Title
Computational Models of the Hippocampus in Radiation and Epilepsy

Permalink
https://escholarship.org/uc/item/2tk3t7zg

Author
Schneider, Calvin James

Publication Date
2015

Peer reviewed|Thesis/dissertation

UNIVERSITY OF CALIFORNIA,
IRVINE

Computational Models of the Hippocampus in Radiation and Epilepsy

DISSERTATION

submitted in partial satisfaction of the requirements
for the degree of

DOCTOR OF PHILOSOPHY

in Biomedical Sciences

by

Calvin James Schneider

Dissertation Committee:
Professor Ivan Soltesz, Chair
Professor Richard Robertson
Professor Charles Limoli

2015

TABLE OF CONTENTS

LIST OF FIGURES

iv

LIST OF TABLES

ACKNOWLEDGMENTS

Most of all I would like to thank my doctoral advisor and mentor Ivan Soltesz. Much of the way I approach science and life has been shaped by your leadership and mentorship. Thank you for always being honest and having an open door during my time in your lab.

I would also like to thank my doctoral committee members, Charles Limoli and Richard Robertson. Charlie, our collaboration has taken me all over the world and I am truly grateful for all the growth and stories I now have because of it. Rick, thank you for your guidance over the years, and making sure I could always talk modeling to those who don't do programming.

I would like to thank Jeffrey Krichmar and David Reinkensmeyer for serving on my advancement committee and providing input on my work.

I would like to thank Hermann Cuntz for his invaluable guidance and mentorship from a computational perspective. I would also like to thank Peter Jedlicka for his help getting this project off the ground, and for his continued input.

I would like to thank Irina Sokolova, Roman Vlkolinsky, and Greg Nelson for letting me tag along for all the NASA-related activities.

I would like to thank the members of the Soltesz lab for the countless discussions and for getting me away from my computer. I would in particular like to thank Mikko Oijala for helping convert me to a MATLAB-er, and Ivan Raikov for being the only Soltesz lab member to always understand what I'm talking about.

I would like to thank my friends and family, for feigning interest and understanding in my work and for always showing me the utmost support. I would in particular like to thank Nicole Worcester for being my best friend and biggest cheerleader, even when you're tired of hearing about the brain.

The text of Chapter 1 is a reprint of material as it appears in Schneider et al. 2012. My coauthors on this publication were Marianne Bezaire and Ivan Soltesz.

The text of Chapter 2 is a reprint of material as it appears in Schneider et al. 2014. My coauthors on this publication were Hermann Cuntz and Ivan Soltesz.

The text of Chapter 3 is a reprint of material as it appears in Sokolova et al. 2015. My coauthors on this publication were Irina Sokolova, Marianne Bezaire, Ivan Soltesz, Roman Vlkolinsky, and Gregory A. Nelson.

The text of Chapter 4 is a reprint of material as it appears in Szabo et al. 2015. My coauthors on this publication were Gergely Szabo and Ivan Soltesz.

CURRICULUM VITAE

Calvin James Schneider

Education

2009-2015   Ph.D. in Biomedical Sciences
             University of California, Irvine

2005-2009   Bachelor of Arts in Biochemistry
             University of San Diego

Research Positions

2009-Present Graduate Student Researcher, Department of Anatomy & Neurobiology;
              University of California Irvine; Irvine, CA
              Research Advisor: Ivan Soltesz, PhD

2008-2009   Undergraduate Researcher, Department of Chemistry & Biochemistry;
              University of San Diego; San Diego, CA
              Research Advisor: Dr. Jeremy Kua

2007   Undergraduate Researcher, Department of Chemistry & Biochemistry;
              University of San Diego; San Diego, CA
              Research Advisor: Dr. Deborah Tahmassebbi

Honors

2007   Summer Undergraduate Research Experience Grant, University of San Diego
2007   Associated Students Grant, University of San Diego

Publications

Szabo GG, **Schneider CJ**, Soltesz I. Resolution revolution: epilepsy dynamics at the microscale. *Curr Opin Neurobiol* 2015, 31c:239-243.

Sokolova IV, **Schneider CJ**, Bezaire M, Soltesz I, Vlkolinsky R, Nelson GA. Proton Radiation Alters Intrinsic and Synaptic Properties of CA1 Pyramidal Neurons of the Mouse Hippocampus. *Radiat Res* 2015, 183:208-218.

Schneider CJ, Soltesz I. Net worth of networks: specificity in anticonvulsant action. *Epilepsy Curr* 2015, 15:45-46.

Schneider CJ, Cuntz H, Soltesz I. Linking macroscopic with microscopic neuroanatomy using synthetic neuronal populations. *PLoS Comput Biol* 2014, 10:e1003921.

Schneider CJ, Bezaire M, Soltesz I. Toward a full-scale computational model of the rat dentate gyrus. *Front Neural Circuits* 2012, 6:83.

Book Chapters

Case MJ, Morgan RJ, **Schneider CJ**, Soltesz I. Computer Modeling of Epilepsy. In: Jasper's Basic Mechanisms of the Epilepsies, 4th ed. New York: Oxford University Press; 2012.

ABSTRACT OF THE DISSERTATION

Computational Models of the Hippocampus in Radiation and Epilepsy

By

Calvin James Schneider

Doctor of Philosophy in Biomedical Sciences

University of California, Irvine, 2015

Professor Ivan Soltesz, Chair

Computational modeling of neuronal networks enables the study of variables in isolation while approximating the biological state. In conditions such as the exposure to radiation and epilepsy, a large number of structural and network parameters are altered, making the role of any individual abnormality unclear. The goal of the presented work is to develop realistic computational models of the hippocampus for the incorporation of experimental observations and to shed light on the relative importance and deleteriousness of pathological alterations. The **Introduction** summarizes our motivations and the utility of realistic computational models, particularly for the hippocampus, and gives a background for the abnormalities present in the irradiated and epileptic conditions. **Chapter 1** describes our work translating our previous model to be compatible with parallel computing and then expanding the model to run at full-scale, with over a million neurons. It then outlines a methodology for the generation of computational models for the dendritic trees of granule cells, the most prevalent cell type in the dentate gyrus, using previous tools that contained a microscopic focus. In **Chapter 2**, we report an entirely new methodology for morphology generation that instead shifts the focus to the macroscopic neuroanatomy, growing dendrites within a realistic three-dimensional structure and enabling the

population-level study of morphology. **Chapter 3** describes a study in which our computational modeling was used to interpret experimental observations in area CA1 of the hippocampus after exposure to proton radiation. The study reports long-term but subtle changes in the passive properties of pyramidal neurons, the principal excitatory cell type in CA1, which were found in a computational model to have a surprisingly dramatic effect on network function. **Chapter 4** reviews the ever-growing observations of the non-recurrent microscopic nature of seemingly repetitive macroscopic events in epilepsy. **Chapter 5** provides the immediate next steps and future directions for computational modeling in health and disease, building on the foundation and framework provided in the previous chapters to suggest several avenues to bring computational models ever closer to the experimental, biological, and clinical conditions.

INTRODUCTION

There is a growing interest in the effects of radiation on the function of the central nervous system, not only because of the use of radiation in the treatment of diseases such as cancer, but also for the future prospects of deep space exploration. The short-term impact on cognitive performance and the long-term risks associated with space radiation exposure are both relatively unknown. Cranial radiation has been well-documented to cause cognitive decline in humans (Lee et al., 1989;Crossen et al., 1994;Abayomi, 1996;Kramer et al., 1997;Surma-aho et al., 2001), and irradiated mice also exhibit hippocampus-dependent cognitive impairment, which is accompanied by deficits in dentate gyrus neurogenesis (Raber et al., 2004;Rola et al., 2004).

The dentate gyrus is uniquely situated to control the cortical inputs arriving at the hippocampus as the first relay point in the trisynaptic loop (dentate gyrus, CA3, and CA1). The overwhelming majority of neurons in the dentate gyrus are granule cells, with over 1.2 million being present in the rat (West et al., 1991;Rapp and Gallagher, 1996). The dentate gyrus is one of two areas in the adult brain (the other being the olfactory bulb) where neurogenesis occurs, as granule cells are functionally integrated into the network throughout life. While the upstream entorhinal cortex region has high levels of activity (Barnes et al., 1990), the dentate gyrus is known for its quiescence, as only 1-2% of the granule cells are active during a behavioral episode (Chawla et al., 2005;Tashiro et al., 2007;Alme et al., 2010). This sparse coding feature of the network is thought to be driven by the newborn granule cells, but their role in the process is still controversial (Piatti et al., 2013).

In a more recent study, significant changes to the granule cell dendritic architecture in the dentate gyrus of the hippocampus have been shown in irradiated mice (Parihar and Limoli, 2013). Dendritic branching, length, and surface area were all shown to be reduced in a dose-

dependent manner, in addition to observed reductions in the number and density of dendritic spines. This study is corroborated by a previous study that found reductions in spine density in the dentate gyrus and CA1 subfields (Chakraborti et al., 2012), but the reductions in CA1 were present to a lesser extent. Alterations in dendritic complexity are present in numerous brain disorders (Terry et al., 1981;Bremner et al., 1995;Kaufmann and Moser, 2000;Nishimura et al., 2011), so they could be a likely source of the cognitive impairments seen with radiation exposure. The functional impact of these structural abnormalities on hippocampal function, both at a single cell level and for the network, are unknown, and cannot be studied in isolation experimentally due to the numerous other pathological changes in the irradiated brain.

Temporal lobe epilepsy (TLE) is the most common form of epilepsy in the adult population (Engel et al., 2008), and the dentate gyrus has garnered particular interest due to the robust pathology observed in human patients, such as granule cell axon (or mossy fiber) sprouting (Buckmaster, 2012b) and the loss of hilar neurons (Margerison and Corsellis, 1966). The dentate gyrus circuit has been increasingly shown to be reorganized in the epileptic brain, including an increased input and output for those cells that survive the epileptogenic insult (Zhang et al., 2009;Halabisky et al., 2010;Peng et al., 2013;Zhang et al., 2014). As the number of cellular and network changes observed in TLE patients and animal models continues to grow, the potential role of computational modeling in determining which of these changes is truly pertinent to hyperexcitability and hypersynchrony in the epileptic network grows simultaneously. Experimental approaches alone most often cannot unequivocally tease apart the overall network effects of the numerous variables altered in an epileptic hippocampus, but recent advances in modeling of the control and epileptic dentate gyrus have demonstrated the ability of data-driven, biologically realistic models to test the relative importance of cellular and circuit alterations and

make experimentally testable predictions (Santhakumar et al., 2005; Dyhrfjeld-Johnsen et al., 2007; Morgan and Soltesz, 2008).

The primary goal of this work is to create a model of the dentate gyrus that can test the various alterations present in the pathological irradiated and epileptic conditions, and to also provide a general tool for researchers to perform their own studies and make their own predictions. Full-scale modeling allows for experimentally-determined parameters to be directly incorporated into the model instead of having to scale these values down to compensate for smaller size networks, such as scaling the connectivity and synaptic strengths in our previous models. The changes in dendritic architecture observed after radiation require realistic dendritic morphologies to be present in the model, but all granule cells in our previous models were identical and had a simple morphology based on a previous study (Aradi and Holmes 1999), which dramatically differs from the biological dentate gyrus where every cell has unique electrophysiological characteristics and morphology. The studies presented in **Chapter 1** and **Chapter 2** provide several major steps toward a more complete dentate gyrus model and a solid foundation and framework for future work, from enabling full-scale simulations to generating realistic and diverse dendritic morphologies.

Chapter 1 describes the translation of our previous 1:20 scale model of the rat dentate gyrus (Dyhrfjeld-Johnsen et al., 2007), that was only able to run on a single processor of a single computer, to utilize parallel computing. The model experienced a superlinear speedup, reducing the required simulation time from 11.0 hours to 6.8 minutes with only 90 processors. In addition, the increased computational power made available to the model by parallel computing enabled simulations of the full-scale model with over a million cells, incorporating two of the previously mentioned hallmark pathological changes in the dentate gyrus observed in epilepsy: mossy fiber

sprouting and hilar cell loss. The construction of realistic granule cell dendritic trees is also described by combining previous tools for the generation (Ascoli and Krichmar, 2000) and analysis (Scorcioni et al., 2008) of morphology. However, these tools follow a microscopic approach, analyzing parameters such as branch angles and lengths and ignoring the overall structural context that the dendrites grow within. Using this previous method, we were only about to generate half of the granule cell population. In **Chapter 2**, we take an entirely new approach to morphology generation, linking microscopic dendritic morphology with the macroscopic neuroanatomy. Instead of constructing dendrites independently and then trying to fit the realistic trees in a structure, we describe a method in which trees are directly grown inside of a realistic three-dimensional structure which promotes the variability. This new methodology allowed us to generate the complete population of granule cell morphologies, matching the experimentally determined characteristics as well as the inherent biological variability. This work provides the foundation for realistic three-dimensional network modeling and can be applied to any other cell type and axons in the future.

The study presented **Chapter 3** switches the focus from the physiological to the pathological, describing long-term changes in the CA1 region of the hippocampus after low-dose proton irradiation. The experimental portion involved electrophysiological recordings from CA1 pyramidal cells and found a seemingly minor change in the passive properties, rendering them less excitable. The impact of this subtle change in individual cells on the network function, however, was unknown. When incorporated into 100 pyramidal cells in a microcircuit model of CA1, the passive property alterations surprisingly had a large impact on network function. The hallmark oscillatory behavior that characterizes the region was dramatically reduced, providing a functional network readout for observed cellular changes. This work highlights the utility of

computational modeling, which allows for the incorporation and interpretation of experimental observations to gain a different perspective or to perform studies not possible with experimental work.

Chapter 4 describes the recent shift in focus toward the opposite direction in regard to epilepsy research, where recurrent macroscale events have been increasingly shown to be non-recurrent when viewed at the microscale. Repeating pathological network manifestations, such as interictal spikes or seizures, are surprisingly comprised of different participating populations of neurons, and the network properties responsible for this behavior is unknown. Computational modeling of this phenomenon would provide a way to isolate whether the inputs to the network or the inherent variability within the network are responsible for generating common motifs with different participants. This work also discusses the growing literature on the dichotomies that exist even with the same cell class, consistent with the heterogeneous nature of seemingly homogenous populations.

Finally, **Chapter 5** discusses future directions and questions to build on the foundations described in the previous chapters. The expansion of models to full-scale and from one to three dimensions results in a similar expansion on the experimental data that can be incorporated as well as the predictions that can be made. It links the model much more closely with the biology, enabling more direct comparisons through future concepts such cutting virtual slices for model validation. Realistic computational models that work in tandem with experimental and clinical efforts could aid in the prevention and treatment of the abnormalities associated with radiation and epilepsy.

CHAPTER 1

Toward a Full-Scale Computational Model of the Rat Dentate Gyrus

Abstract

Recent advances in parallel computing, including the creation of the parallel version of the NEURON simulation environment, have allowed for a previously unattainable level of complexity and detail in neural network models. Previously, we published a functional NEURON model of the rat dentate gyrus with over 50,000 biophysically realistic, multicompartmental neurons, but network simulations could only utilize a single processor. By converting the model to take advantage of parallel NEURON, we are now able to utilize greater computational resources and are able to simulate the full-scale dentate gyrus, containing over a million neurons. This has eliminated the previous necessity for scaling adjustments and allowed for a more direct comparison to experimental techniques and results. The translation to parallel computing has provided a superlinear speedup of computation time and dramatically increased the overall computer memory available to the model. The incorporation of additional computational resources has allowed for more detail and elements to be included in the model, bringing the model closer to a more complete and accurate representation of the biological dentate gyrus. As an example of a major step toward an increasingly accurate representation of the biological dentate gyrus, we discuss the incorporation of realistic granule cell dendrites into the model. Our previous model contained simplified, two-dimensional dendritic morphologies that were identical for neurons of the same class. Using the software tools L-Neuron and L-Measure, we are able to introduce cell-to-cell variability by generating detailed, three-dimensional granule cell morphologies that are based on biological reconstructions. Through these and other improvements, we aim to construct a more complete full-scale model of the rat

dentate gyrus, to provide a better tool to delineate the functional role of cell types within the dentate gyrus and their pathological changes observed in epilepsy.

Introduction

The dentate gyrus network model was developed to study the role of the circuit alterations present in the epileptic dentate gyrus (Santhakumar et al., 2005;Dyhrfjeld-Johnsen et al., 2007) and has been used to make predictions for the existence of nonrandom microcircuits in epilepsy (Morgan and Soltesz, 2008). The network model has also been used in other studies on topics such as epilepsy (Thomas et al., 2009;Thomas et al., 2010), paired-pulse inhibition (Jedlicka et al., 2010), excitability (Winkels et al., 2009;Jedlicka et al., 2011), computational modeling software (Gleeson et al., 2007), and in the construction of a CA1 model (Cutsuridis et al., 2010). Of particular note is the use of the model to test improvements to the NEURON simulation environment (Migliore et al., 2006;Hines and Carnevale, 2008;Hines et al., 2008a;Hines et al., 2008b). The network simulations performed in the studies listed above have exclusively used the smaller 1:2000 scale model (Santhakumar et al., 2005), in part due to the increased time associated with simulating the 1:20 scale model, with a reported 35-70 hours per simulation (Dyhrfjeld-Johnsen et al., 2007).

The creation of parallel NEURON and the speedup obtained during tests on the 1:2000 scale model (Migliore et al., 2006) have provided a means to not only make the recent model more accessible to researchers, but to also remove the limitations on the size and complexity of the computational model. The results presented in this study represent the next step in model development, expanding the size and scope of the model. The results from the translation of the 1:20 scale model from a serial to parallel implementation are described, as well as the

enlargement of the model to the full size of the rat dentate gyrus. Through the cooperation of two software tools, the complexity of the model can be increased with the generation of variable and realistic dendritic morphology for the sample case of granule cells. These model improvements reflect a significant advancement toward a realistic full-scale computational model.

Materials and Methods

All simulations, virtual neuron generation, and analysis were performed on the UCI Broadcom Distributed Unified Cluster (BDUC) or a PC running Ubuntu Linux. Data analysis and plotting were performed using Python 2.7.1.

Dentate Gyrus Network Simulations

All network simulations were performed using NEURON 7.0 (Hines and Carnevale, 1997). NEURON was configured to run in parallel on the Linux BDUC cluster with Openmpi 1.4.3, as shown previously (Hines and Carnevale, 2008). The serial version of the 1:20 scale model is freely available at ModelDB (http://senselab.med.yale.edu/modeldb/ShowModel.asp?model= 124513). The serial version of the dentate model was translated to a parallel implementation using strategies described elsewhere (Migliore et al., 2006;Hines and Carnevale, 2008). This involved assigning each cell a global identifier, so that even though a cell is only created on one host, all other hosts are still be able to refer to that cell. Each cell was then associated with its own random number generator for creating connections which uses a seed that is dependent on its global identifier. The dentate model NEURON code has also been rewritten with an emphasis on modularization and explanatory commenting in order to increase its adaptability and accessibility for the general neuroscience community.

The 1:20 scale parallel model was constructed in accordance with the serial model from previous studies (Dyhrfjeld-Johnsen et al., 2007;Morgan and Soltesz, 2008). Multicompartmental models for granule cells, mossy cells, basket cells, and hilar cells with axonal projections to the perforant path (HIPP) were taken from the original 1:2000 scale model (Santhakumar et al., 2005). These are the numerically dominant cell types found in the dentate gyrus. The single-cell models contained ionic currents dependent on the given cell type, including sodium, fast- and slow-delayed rectifier potassium, A-type potassium, I_h, L, N, and T-type calcium, and calcium-dependent potassium currents. The ionic currents in the cell models were previously tuned to match the passive and active properties observed experimentally for each cell type (Santhakumar et al., 2005). Connectivity was based on a highly realistic, data-driven structural model (Dyhrfjeld-Johnsen et al., 2007), and the probability of making a connection between two cells was increased fivefold to account for the reduced size of the network. The two elements of the injured model (hilar cell loss and mossy fiber sprouting) were simulated at 80% of their maximum values, as this value produced maximal epileptiform activity in the network model and corresponds to the level of mossy cell survival observed in human temporal lobe epilepsy (Blumcke et al., 2000;Gabriel et al., 2004). Perforant path stimulation was simulated through simultaneous input to 5,000 granule cells (10%), 10 mossy cells (3.3%), and 50 basket cells (10%) located in the middle lamella of the model dentate gyrus at 5ms from the start of the simulation.

The full-scale model eliminated previous scaling adjustments that were required by the smaller network size. The number of cells was the same as estimated to be in the dentate gyrus in the rat (for a detailed description, see Dyhrfjeld-Johnsen et al. 2007), with 1,000,000 granule cells, 30,000 mossy cells, 10,000 basket cells, and 12,000 HIPP cells evenly distributed along the

septotemporal axis. Hilar cell loss and mossy fiber sprouting were again simulated at 80% of their maximum. The peak conductance for sprouted granule cell synapses was reduced from 1.0 nS to 0.5 nS, the original estimate based on experimental data (Molnar and Nadler, 1999). Synaptic conductances for connections from granule cells to both inhibitory cell types were reduced by a factor of two to avoid depolarization block, as done previously (Dyhrfjeld-Johnsen et al., 2007). Perforant path stimulation was simulated through simultaneous input to 10,000 granule cells (1%), 20 mossy cells (0.33%), and 100 basket cells (1%), which corresponds to stimulation of $1/10^{th}$ of the middle lamella of the model dentate gyrus.

Reconstructions

Digital reconstructions of dendritic trees were obtained from 19 granule cells labeled in vivo in the rat dentate gyrus (Buckmaster, 2012a). The three-dimensional Neurolucida reconstructions were corrected for shrinkage in the transverse (1.06X) and depth (1.96X) planes based on previous estimates (Buckmaster and Dudek, 1999) using Neurolucida software (MicroBrightfield, Williston, VT). Reconstruction files were converted from .DAT to .ASC format for compatibility with morphological analysis.

Analysis and Generation of Dendritic Morphology

The creation of realistic dendritic morphologies was performed using two freely available software programs: L-Measure and L-Neuron. Morphological parameters from granule cell reconstructions and generated virtual neurons were extracted using L-Measure v4.0 software (Scorcioni et al., 2008). L-Measure is available at http://cng.gmu.edu:8080/Lm/. Virtual dendritic trees were generated using L-Neuron v1.08 (Ascoli and Krichmar, 2000), available at

. The L-Neuron program was executed with the Hillman/PK dendritic growth algorithm (Ascoli et al., 2001), and outputs were generated in Southampton Archive format (.swc) for compatibility with L-Measure analysis.

The parameters utilized by the dendritic growth algorithm, referred to as basic parameters, were extracted from the granule cell reconstructions as raw values. Extracted basic parameter distributions were then incorporated into L-Neuron using one or more of the statistical distributions allowed in L-Neuron: gamma, normal, uniform, and constant value distributions. Many of the basic parameters are compatible and can thus be directly incorporated into L-Neuron from L-Measure. The definitions for some basic parameters, however, are different between L-Neuron and L-Measure, which can be modified to create congruency. For example, L-Neuron generates terminal dendritic branches by creating an interbifurcation segment and then attaching a terminal segment, whereas L-Measure analyzes the two segments as a single branch. This creates a discrepancy between the distribution input for L-Neuron and the distribution for generated outputs measured with L-Measure for parameters such as the path length of the terminal branch. Adjustments were made to the L-Neuron input to maximize the overlap between the basic parameter distributions extracted from generated virtual neurons and those extracted from reconstructions. As a result, L-Neuron creates morphologies that have similar basic parameters, including the path length of terminal branches noted above, as the sample reconstructions. For statistical tests, the outputs for the constant value distributions in L-Neuron were set to their intended values due to minor deviations imposed in the L-Neuron program.

Morphological parameters not used in the dendritic growth algorithm, known as emergent parameters, were used to compare virtual and real neurons, as well as to filter for biologically realistic virtual granule cells. Scalar emergent parameters summarize a morphological

11

characteristic in a single value, whereas distribution emergent parameters show the dependence of one parameter on another. The scalar and distribution emergent parameters used in this study were largely taken from a previous study using L-Neuron (Ascoli et al., 2001). The scalar emergent parameters used were total dendritic length, number of bifurcations, surface area, average path distance to dendritic tips, average Euclidean distance to tips, maximum Euclidean distance to tips, maximum branch order, partition asymmetry, transverse spread, and longitudinal spread. The transverse and longitudinal spreads were used instead of height, width, and depth in order to provide an orientation-independent measure of the three-dimensional extent of dendritic trees. Transverse spread was defined as the maximum distance in the xy plane between dendritic tips, while longitudinal spread was the maximum distance in the z plane. Generated virtual neurons were selected if they fell within two standard deviations of the mean for all emergent parameters except surface area. Assuming a normal distribution, this theoretically includes more than 95% of the granule cell population. The two standard deviation limit for surface area would have allowed for unrealistic values that were lower than the allowed length, so the constraint was changed to 1.65 standard deviations (theoretically more than 90% of granule cells).

Results

Parallelization of the 1:20 Scale Model

Previous implementations of the rat dentate gyrus network model were scaled down from the biological dentate gyrus because they were limited to the use of a single processor. The creation of parallel NEURON (Migliore et al., 2006) dramatically increased the computational resources available to network simulations. Increasing the number of processors for the 1:2000 scale model has been shown to produce a superlinear speedup of the overall runtime when tested

on several different parallel computing systems (Migliore et al., 2006). Using the principles detailed in that conversion, the more recent 1:20 scale dentate gyrus model (Dyhrfjeld-Johnsen et al., 2007;Morgan and Soltesz, 2008) was translated for compatibility with parallel NEURON. Because the granule cells in the control model network only fire sparsely as in the biological dentate gyrus (Morgan and Soltesz, 2008), the "injured" model, which contains several of the experimentally observed changes in epilepsy and displays epilepsy-related hyperactivity, was used in order to generate network activity for the parallel implementation. The general network topology of the dentate gyrus model is depicted in Figure 1.1A. The superlinear speedup from previous studies was also observed with the 1:20 scale model for up to the 90 processors tested, as shown in Figure 1.1B. The superlinear quality, instead of a purely linear result, is thought to be due to the more efficient use of a processor's memory (Migliore et al., 2006). The use of 90 processors decreased the overall runtime from 11.0 hours to 6.8 minutes for 300 milliseconds of model network activity. The granule cell activity for parallel model simulations is shown in Figure 1.1C. The model network connectivity and activity were identical for all parallel simulations regardless of the number of processors used.
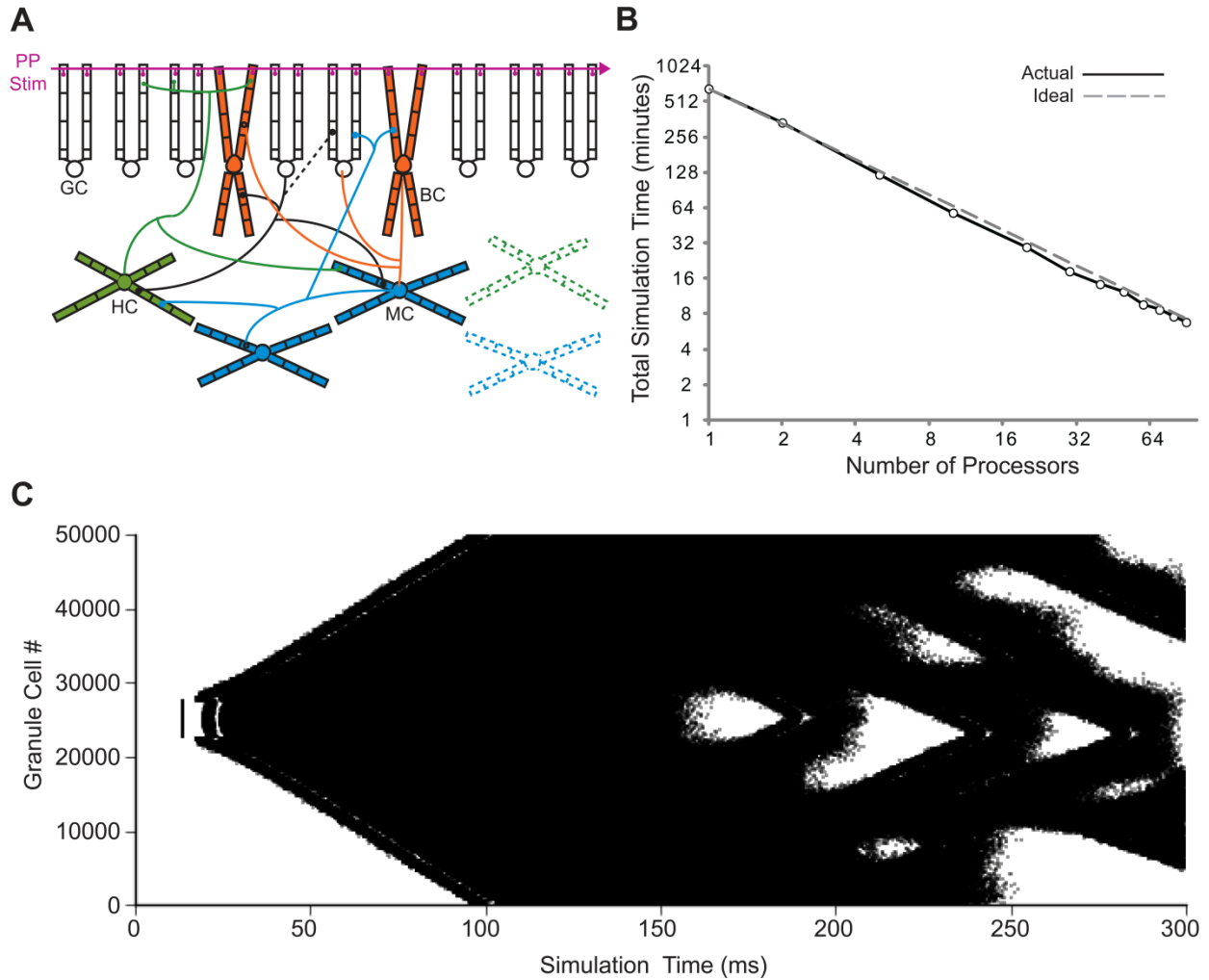
Figure 1.1. Translation to parallel NEURON. (**A**) Basic network connectivity of the dentate model. A depiction of the dendritic structure, connectivity, and location of synapses for the four cell types is shown. Note that the septo-temporal extent of the axons is also incorporated into the model (see Dyhrfjeld-Johnsen et al., 2007) but is not illustrated here. In the injured model, HIPP cells and mossy cells are lost, while granule cells synapse onto other granule cells (changes are represented by dashed lines). GC, granule cell; BC, basket cell; HC, HIPP cell; MC, mossy cell; and PP Stim, perforant path stimulation. (**B**) Runtime of 80% injured network simulations versus the number of processors for actual and ideal scaling. (**C**) Granule cell activity for the parallel 1:20 scale model. Each dot represents a single granule cell spike.

The conversion to a parallel implementation makes the construction of a full-scale

dentate gyrus computational model feasible. The increased availability of computational

resources provided by parallel computing addresses the two main limiting factors to model

network size: runtime and memory capacity. To construct the full-scale model, the number of

cells and the connectivity of the 1:20 scale model were modified to be in agreement with the

previous dentate gyrus structural model (Dyhrfjeld-Johnsen et al., 2007). The full-scale model

contained over 1,000,000 cells and over 470,000,000 connections when simulated with the 80%

injured model. The full-scale simulation shown in Figure 1.2 was performed on 150 processors,

required ~220 GB of RAM, and was completed in 11.1 hours. The reverberating network activity

seen in previous scaled down injured models is observed in the full-scale network, shown for

each cell type in Figure 1.2A. The granule cell activity spreads throughout the network and

persists for the entire simulation time of one second. A voltage trace recorded from a granule cell

demonstrates the realistic firing pattern of the model granule cells, shown in Figure 1.2B. The

model, as explained above, represents a dentate gyrus from the epileptic rat brain with 80% hilar

cell loss and heavy mossy fiber sprouting. The model depicted in Figure 1.2, while data-driven,

still omits many of the changes known to occur in epilepsy, with hilar interneuron axon sprouting

as one example (Zhang et al., 2009), as well as several other features, e.g. some interneuronal

subtypes, gap junctions, short-term plasticity etc. These features will need to be incorporated into

the model in the future.
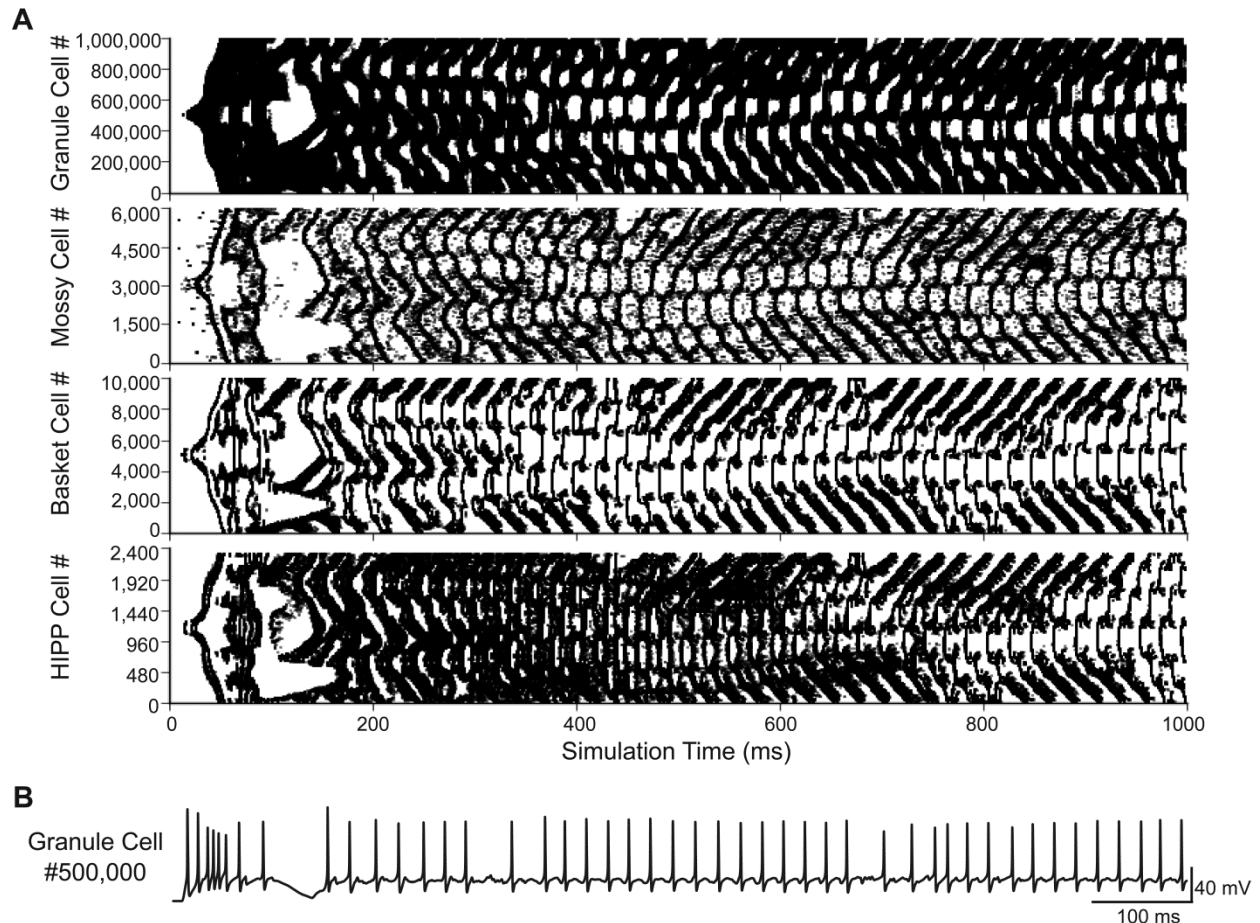
Figure 1.2. Full-scale dentate gyrus simulation. (**A**) Activity for each of the four cell types in the 80% injured model. Each dot represents a single spike. (**B**) Voltage trace from the simulation shown in A for granule cell #500,000.

Creating Variability in Dendritic Morphology

Due to the additional computational resources provided by parallel computing, the complexity of the dentate gyrus model can be expanded just as with the network size. The single cell models are one of the previously simplified aspects of the model that can be improved, such as the single granule cell model. The current granule cell model (introduced in Santhakumar et al., 2005 for the 1:2000 model and also used in Dyhrfjeld-Johnsen et al., 2007 for the 1:20 model) contains nine cylindrical compartments with the diameter of the dendrites constant throughout the dendrites, based on a previous computational model (Aradi and Holmes, 1999). In

16

addition, the morphology and biophysics are equivalent for every granule cell in the network, so that the 1:20 scale model contains 50,000 identical simplified granule cells. The introduction of realistic morphology and cell-to-cell variability would greatly improve the complexity of the network model and can be achieved using two freely available software tools: L-Measure (Scorcioni et al., 2008) and L-Neuron (Ascoli and Krichmar, 2000).

The general strategy for virtual neuron generation was to use morphological parameters extracted from granule cell reconstructions to create realistic virtual neurons that are as much as possible indistinguishable from the reconstructed cells. Basic morphological parameters required by the L-Neuron dendritic growth algorithm were extracted from granule cell reconstructions using L-Measure and are listed in Figure 1.3. The extracted parameter distributions were incorporated into L-Neuron to generate virtual dendritic trees with the same basic parameters as the experimental reconstructions. There was no significant difference between real and virtual granule cell basic parameter distributions (Figure 1.3; p>0.05, two-sample Kolmogorov-Smirnov test). The L-Neuron program thus creates granule cell dendritic trees with similar basic parameters to those seen in granule cells in the biological dentate gyrus. However, the basic parameter distributions used in L-Neuron have a high degree of variability, and it has been noted by previous studies (Ascoli et al., 2001;Donohue et al., 2002) that virtual dendrites generated with L-Neuron have an excessive degree of variability when compared with sample dendrites. Accordingly, generated dendrites will not necessarily be biologically realistic nor produce a representative population. To counteract the excessive variability, the high degree of variability in L-Neuron inputs is still allowed, but the outputs are filtered to select for only those morphologies that are representative of the experimental reconstructions. A population can then

be constructed from these biologically realistic morphologies that has a similar degree of variability as the sample set of reconstructions.

Basic Parameter	Description	Probability Distribution	K-S p-value
bif_ampl_remote	Angle between a bifurcation point and the ends of the two daughter branches		0.61
ibf_branch_pathlength	Length of interbifurcation branches (µm)		0.27
term_branch_ pathlength	Length between the last bifurfaction in a branch and the terminal tip (µm)		0.93
contraction	Ratio between the Euclidean distance and the path length of a branch		0.29
PK_classic	Poliko constant modifying Rall's law, with Rall Power set to 1.5		0.28
HillmanThreshold	Weighted average between 50% of father and 25% of daughter diameters for terminal bifurcation (µm)		0.51
Daughter_Ratio	Ratio between larger and smaller branch diameters at bifurcation		0.35
Taper_2	Length-independent percent of decrease in diameter		0.38
Stem_Diameter	Starting diameter for dendritic tree (µm)		0.96

Figure 1.3. Basic parameter distributions are matched in order to generate virtual granule cells. The basic parameters extracted from L-Measure and incorporated into L-Neuron are listed with their definitions. For more information see the L-Measure website listed in Materials and Methods. The probability distributions are plotted as probability density versus the basic parameter value for experimental reconstructions (gray bars) and 10,000 generated virtual neurons (black bars), and the p-value for the two-sample Kolmogorov-Smirnov test for the overlap of these distributions is shown.

18

The generated granule cells were filtered based on scalar emergent parameters that are not used in the dendritic growth algorithm, such as the total dendritic length of the cell. Constraints involving variability up to two standard deviations for most emergent parameters allowed for values beyond those measured from the sample reconstructions, but restricted generated neurons to only those that have biologically realistic values. The virtual granule cells were then chosen to match a Gaussian or Poisson distribution for the total dendritic length, number of bifurcations, and surface area, shown in Figure 1.4A, to create a representative and distributed population. The virtual granule cell population and granule cell reconstructions were also compared using distribution emergent parameters that examine the relationship between two parameters. The distribution emergent parameters shown in Figure 1.4B demonstrate that the generated granule cells are nearly indistinguishable from the reconstructed cells. This method of constraining and selecting virtual dendrites allows a small set of experimental reconstructions to be amplified to create a realistic and distributed population of granule cells. A sample of real and virtual granule cells is shown in Figure 1.4C. The dendritic trees can be improved by adding tropism to increase the curvature and smoothness of the dendrites, but the overall structures for real and generated neurons are statistically indistinguishable.
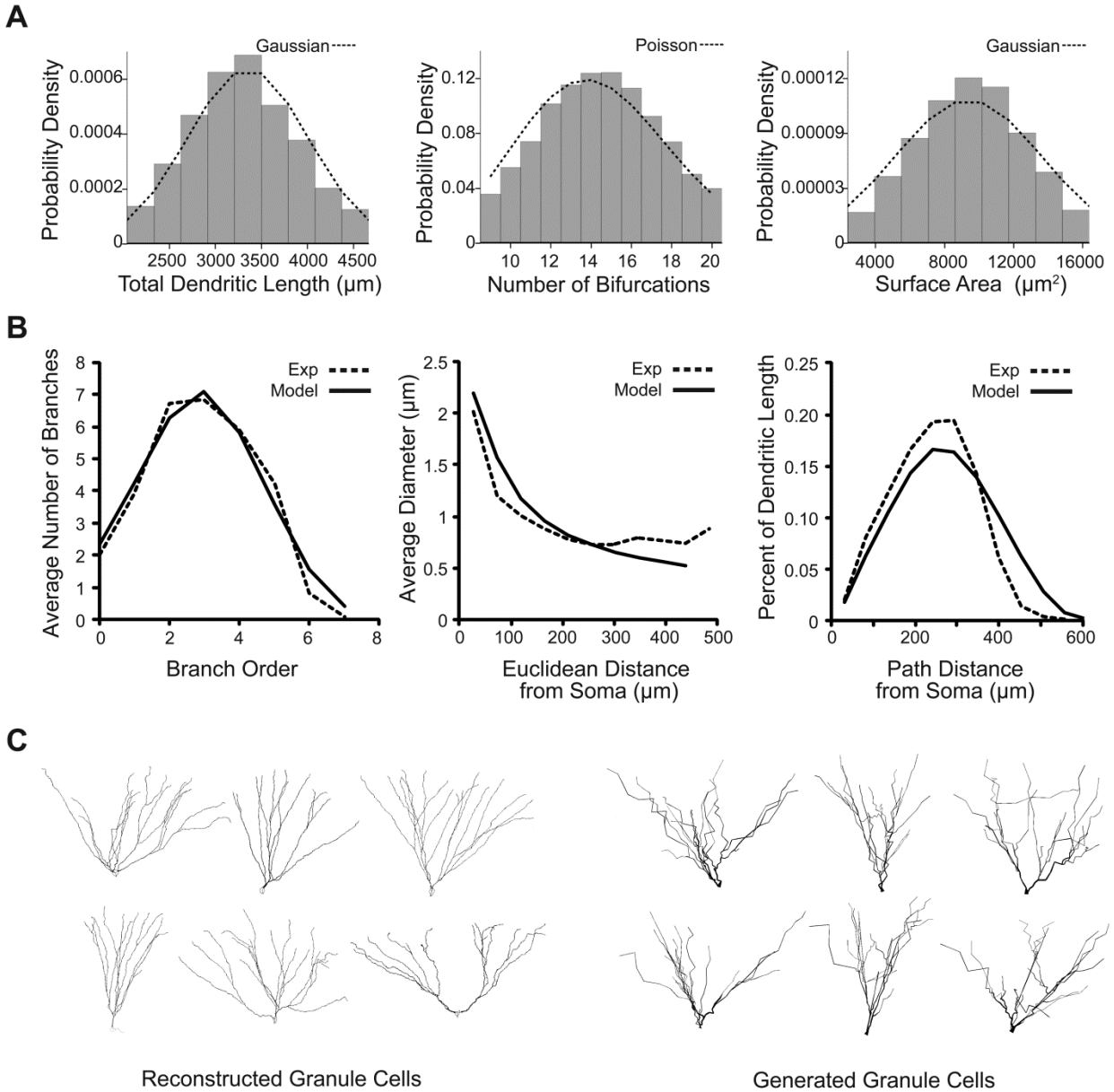
Figure 1.4. Emergent parameter distributions demonstrate the creation of variable and realistic virtual granule cells of the dentate gyrus. (**A**) Probability distributions for several scalar emergent parameters of 100,000 generated granule cells. Distributions for total dendritic length, number of bifurcations, and surface area are shown with their ideal respective truncated Gaussian and Poisson probability density functions. (**B**) Distribution emergent parameters for real (dashed line) and 10,000 generated (solid line) neurons. (**C**) Sample reconstructed and generated dentate granule neurons, visualized in NEURON.

Discussion

The model development presented in this study reflects a significant advancement in bridging the gap between the biological dentate gyrus and the dentate gyrus network model. The speedup conferred by parallel computing makes the 1:20 scale model more accessible for use with even a small computing cluster by reducing the time required for simulations, and the additional computational resources enable the model to be implemented at full scale. These full-scale simulations are advantageous in that they remove the scaling adjustments made for smaller models, and values determined experimentally can now be directly incorporated into the model. The computational model thus becomes a more effective complement to experimental techniques.

The additional computational resources also allow for the complexity of the network to be increased to provide a greater level of accuracy, including at the level of single cells. The inherent cooperation between morphological analysis with L-Measure and generation with L-Neuron provides a means by which to amplify a small sample of reconstructed cells into a distributed virtual population. The availability of detailed reconstructions is ever-growing, such as through the Neuromorpho.org database (Ascoli et al., 2007), so the tools and principles used in this study can be applied to other cell types within the dentate gyrus. The potential covariance of morphological parameters, however, is not considered in this study. Similarly, the inter-dependence of physiological parameters will also need to be addressed, especially with a functional model, given previous insights (Golowasch et al., 2002). The introduction of realistic morphology expands the network from a two-dimensional structure that is dominated by a linear strip to a three-dimensional model that allows for cells to be distributed in space and throughout

layers. This ability gives rise to the possibility of making more direct comparisons to the experimental literature, through concepts such as taking a virtual slice of the model.

The incorporation of realistic morphology can be used in concert with experimentation on the passive and active properties of dentate gyrus neurons to create accurate and variable neurons. Recent studies using a combination of experimental methods and computational modeling have described the dynamics of action potential initiation (Schmidt-Hieber and Bischofberger, 2010) and dendritic integration (Schmidt-Hieber et al., 2007;Krueppel et al., 2011) for dentate granule cells. Generated functional models will need to possess the documented characteristics of granule cells in these studies, such as axonal action potential initiation and a similar level of dendritic attenuation of backpropagating action potentials. In addition, the passive and active properties (e.g. resting membrane potential, action potential threshold, etc.) will be compared to literature values, similar to the development of our previous single cell model (Santhakumar et al., 2005). The improvement of single cell models is not reserved only to principal cells, as the properties of fast-spiking basket cells determined through experiment and modeling (Hu et al., 2010;Norenberg et al., 2010), for example, can be incorporated into a more accurate basket cell model. Through these improvements and the resources conferred by parallel NEURON, the computational model of the rat dentate gyrus can reflect a previously unattainable size and accuracy in order to approach a more complete model of the biological dentate gyrus.

Acknowledgments

CHAPTER 2

Linking Macroscopic with Microscopic Neuroanatomy using Synthetic Neuronal Populations

Abstract

Dendritic morphology has been shown to have a dramatic impact on neuronal function. However, population features such as the inherent variability in dendritic morphology between cells belonging to the same neuronal type are often overlooked when studying computation in neural networks. While detailed models for morphology and electrophysiology exist for many types of single neurons, the role of detailed single cell morphology in the population has not been studied quantitatively or computationally. Here we use the structural context of the neural tissue in which dendritic trees exist to drive their generation *in silico*. We synthesize the entire population of dentate gyrus granule cells, the most numerous cell type in the hippocampus, by growing their dendritic trees within their characteristic dendritic fields bounded by the realistic structural context of (1) the granule cell layer that contains all somata and (2) the molecular layer that contains the dendritic forest. This process enables branching statistics to be linked to larger scale neuroanatomical features. We find large differences in dendritic total length and individual path length measures as a function of location in the dentate gyrus and of somatic depth in the granule cell layer. We also predict the number of unique granule cell dendrites invading a given volume in the molecular layer. This work enables the complete population-level study of morphological properties and provides a framework to develop complex and realistic neural network models.

24

Author Summary

Computational models of neurons and neural networks provide a valuable avenue to test our understanding of brain regions and to make predictions to guide future experimentation. Each neuron has a unique dendritic tree, features of which can vary depending on the location of the neuron within the particular brain region. In this study, we generated a complete population of dendritic trees for the most numerous type of neuron in the hippocampus, the dentate gyrus granule cell, using a realistic three-dimensional structural context to drive the generation process. Morphological properties can now be studied at the level of complete neuronal populations, and this work provides a foundation to build upon in the construction of large-scale, data-driven neuroanatomical and network models.

Introduction

Growing evidence for the importance of dendritic structure on neuronal function has inspired the construction of morphologically realistic computational models of single neurons. Dendritic morphology has been shown to have a significant impact on neuronal firing properties, both between neurons of different classes (Mainen and Sejnowski, 1996) and within the same class (Krichmar et al., 2002;van Elburg and van Ooyen, 2010), as well as on signal integration and propagation (Vetter et al., 2001;Schaefer et al., 2003;Acker and White, 2007). The intra-class morphological variability could have a significant impact on the integration of individual neurons into the circuit and their resulting role in network computation. Correspondingly, this has led to the development of detailed three-dimensional morphological reconstructions of single cells (Ascoli et al., 2007) and functional models incorporating this level of detail (Migliore et al., 2003;Hines et al., 2004). Not only does the incorporation of realistic morphology enable more

accurate reproduction of measured electrophysiology, it also allows for a more detailed representation of network connectivity. These together enable a better understanding of the underlying computation in the network. Advances in computational power as well as in parallel computing, such as the development of parallel versions of neurophysiological simulation environments (Goddard and Hood, 1998;Migliore et al., 2006;Hines and Carnevale, 2008;Hines et al., 2008a;Hines et al., 2008b), have made the simulation of large networks with detailed neuron models accessible. Currently, however, the majority of functional electrophysiological network models utilize uniform single models or very small subsets of models to describe neurons of a given class, overlooking the inherent biological diversity. In addition, the connectivity is usually oversimplified in almost all functional neural networks, whether by the use of probabilistic methods rather than explicit connectivity or by making connections using only a subset of the neurons in the network population, while in most applications it should in fact reflect the full morphological architecture of dendrites and axons. The generation of full-scale, population-level morphological models is, therefore, an important and timely goal. Since experimental reconstructions are to date available only in small sample sizes, techniques to generate population-level morphological models will require the amplification of these data sets to fully realistic and diverse populations (Schneider et al., 2012).

Aside from quantifications based on reconstructions of single cells, existing neuroanatomical data encompasses a large number of measures at multiple levels, such as density estimates for synaptic zones using electron microscopy or cell counts and population analysis using molecular techniques as well as entirely macroscopic features of neural tissue (Braitenberg and Schüz, 1991). The optimal arrangement of elements of neural circuits in the brain has been extensively studied (Cherniak, 1992;Cherniak, 1994;Chklovskii, 2000;Chklovskii

26

et al., 2002;Chen et al., 2006), and a recent trend has been to put neuroanatomical single cell reconstructions in the macroscopic context in which they originally existed (Lang et al., 2011;Oberlaender et al., 2012;Ropireddy et al., 2012). In particular, recent work in *Drosophila* has focused on generating a standardized structural model (Rein et al., 2002) and taken steps toward generating a complete network connectivity map by placing all reconstructed neurons into a standard brain (Chiang et al., 2011), which is possible given the smaller population of neurons in invertebrate model organisms. Conventional light microscopy does not have the resolution to reconstruct circuits in densely labeled neuropil (Helmstaedter et al., 2008), and as a result, modern techniques such as large-scale serial block-face scanning electron microscopy have started to provide reconstruction methods for which both the microscopic details of all cells and the macroscopic circuit-level features are present in the same biological tissue samples (Chklovskii et al., 2010;Helmstaedter et al., 2011;Helmstaedter et al., 2013). These data, however, are rather large and complex, and it will be important to develop novel approaches to facilitate the study of such neuroanatomical connectomes (Seung, 2009). The development of large-scale morphological models with macroscopic constraints will enable the analysis of these large data sets and the study of connectomes before full anatomical reconstructions are available.

Current methodologies for the generation of morphological models primarily employ reconstructions and their branching characteristics independent of their originating context. Several studies have relied solely on the reconstructions themselves, involving pure duplication (Scorcioni et al., 2002), making small variations in the lengths and angles of tree branches (Hill et al., 2012), or resizing to fit within a spatial context (Ropireddy et al., 2012). Other methods have focused on the branching properties of the reconstructions and have used a wide variety of algorithms, including the simulation of growth cones with NETMORPH (Koene et al., 2009),

modeling self-referential forces (Memelli et al., 2013), or mapping one-dimensional structures to 3D trees (Winslow et al., 1999). Several of these tools, such as L-Neuron (Ascoli and Krichmar, 2000), EvOL-Neuron (Torben-Nielsen et al., 2008), and NeuGen (Eberhard et al., 2006;Wolf et al., 2013), create variable dendritic trees by stochastically sampling branching parameters from extracted statistical distributions. While the stochastic sampling methodology is able to generate realistic synthetic trees, it was too inefficient in our previous work to generate a complete and distributed population (Schneider et al., 2012), even without the constraint of fitting within a three-dimensional context. The current study reverses the direction of previous methods by starting with the macroscopic neuroanatomy and enables complete population-level construction and analysis.

Here we report a method that allows us to match generated single cell morphologies to measured data as a function of macroscopic features. We do this by devising a computational model that generates morphologies of all single neurons in a population while considering the broader neuroanatomical context in which they grow. First we model the volume of the rat dentate gyrus based on a recent detailed reconstruction of the entire structure (Ropireddy et al., 2012). We then generate single cell morphologies of all granule cells (GCs) as described previously (Cuntz et al., 2010) constrained within this volume. The resulting population data matches the known variability in GC morphology as well as some known key dependences of GC features on location within the dentate gyrus. We then use our model to develop measures and predictions for dendritic features at the population level. This work provides a valuable framework for the study of complete populations of neuronal morphologies and represents a major step in the development of large-scale neural network models.

Results

Model dentate gyrus boundaries

In order to grow dentate gyrus granule cell (GC) dendritic tree structures within their structural context, we first generated a parameterized volume representing the dentate gyrus (DG) shape. Smoothed surfaces for the boundaries of the DG granule cell layer (GCL) and molecular layer (ML) were obtained from a recent high-resolution, 3D serial reconstruction of the rat hippocampus (Ropireddy et al., 2012). Parametric 2D manifolds were then fitted to these boundary surfaces (Figure 2.1A; see also Methods for detailed equations) in order to provide a coordinate system in which depth in the GCL and ML as well as the septo-temporal and infra-versus suprapyramidal axes are mapped. This in turn enabled the subdivision of the ML volume into inner (IML), middle (MML), and outer molecular layers (OML) using intermediate surfaces, since several aspects of GC morphology have previously been associated to these reference structures. The resulting model DG closely matched the structural features of the experimentally reconstructed volume (Figure 2.1B). The model DG had the same overall GCL volume, 3.78 mm^3, and ML volume, 9.02 mm^3, as the experimental reconstruction. Also, the ML width throughout the structure, 247 ± 33 µm, closely matched a previous experimental measurement, 249 ± 33 µm (Claiborne et al., 1990). Slices from the model DG possessed the characteristic curved structure of the biological dentate gyrus, which is known to be more "V"-shaped in the septal region and "U"-shaped in the temporal region (Figure 2.1C). The volume created by the parametric surfaces thus served as a realistic structural context within which to drive GC dendrite generation. Furthermore, the parametric character of the surfaces subsequently enabled the mathematical tractability of the transformation between a planar two-dimensional sheet and the curved two-dimensional manifolds in 3D space.
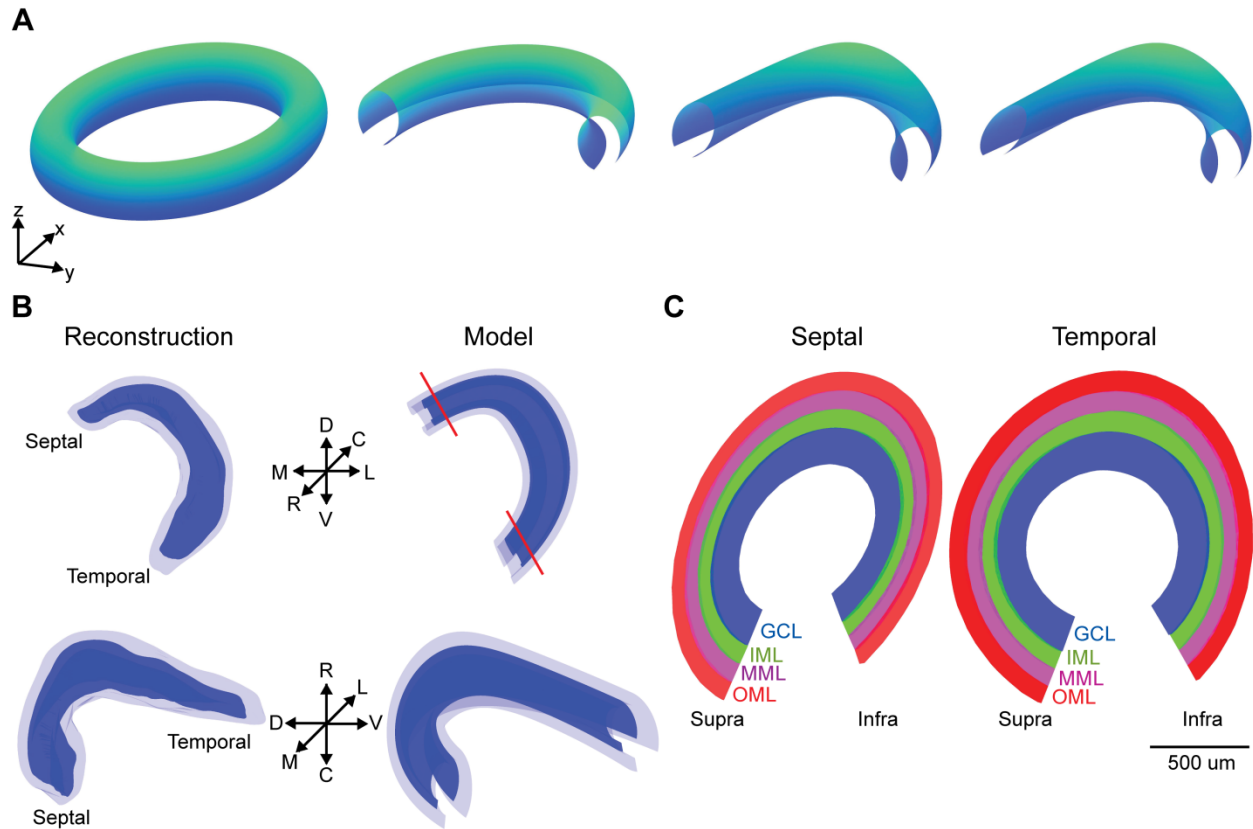
Figure 2.1. Parametric volume representing the dentate gyrus structure. (**A**) The outer boundary for the granule cell layer was created by cutting a piece out of an elliptical torus (left) into a partial structure (middle left), then adding a deflection in the z direction (middle right), and finally creating unequal septal and temporal ends (right). See Methods for details. (**B**) Comparison between the experimental reconstruction and model structure. The rostrocaudal, dorsoventral, and mediolateral axes are shown. Red lines depict slice angles for (**C**). (**C**) 100 μm transverse slices of septal and temporal regions at the level of the red lines in (B). Subdivisions into the different layers is indicated by colors: GCL – granule cell layer (blue), IML – inner molecular layer (green), MML – middle molecular layer (magenta), OML – outer molecular layer (red). Suprapyramidal and infrapyramidal regions are indicated. In (A) and (B), directional arrows represent 1mm.

Generation of synthetic dendritic trees

The dendritic field spanned by the GC dendritic tree can be approximated by an elliptical cone (Williams and Matthysse, 1983;Claiborne et al., 1990;Cuntz et al., 2010). GC trees can be synthesized by connecting a somatic coordinate to target points distributed in such cone-like volumes while minimizing total dendrite length as well as path lengths within the dendrite

30

(Cuntz et al., 2010). To generate the complete GC forest, somata were first distributed within the GCL. The rat DG GCL is estimated to contain approximately 1.2 million tightly-packed GCs (West et al., 1991;Rapp and Gallagher, 1996), and the GC soma is an ellipsoid with an average width of 10.8 µm and height of 18.6 µm (Claiborne et al., 1990). For the purposes of this study, spheres with 12.54 µm diameter corresponding to the volume of an average GC ellipsoid soma were arranged on a large hexagonal grid. Those spheres with any portion located outside of the GCL volume were discarded, and the remaining spheres were selected as somata for the GC population (Figure 2.2A). In this way, 1.19 million somata separated by a 3.5 µm distance were well-packed within the GCL volume. An elliptical cone could now be placed at each of these soma locations to select the target points necessary to grow GC dendritic trees within the ML boundaries.

The optimal wiring algorithm connects points by performing a dual minimization of total dendritic length and path lengths, under a constraint (balancing factor *bf*) that weighs the importance of one over the other. Low values for *bf* lead to strongly minimizing the total wiring which can result in long conduction paths to the soma, while larger *bf* values lead to trees with short conduction times. Target points for all cells were first distributed in the GCL and ML according to proportions estimated from experimentally reconstructed dendritic trees (Figure 2.2B, see also Figure S2.1). Points within each elliptical cone (Figure 2.2C, shaded area) were then isolated, and a subset of these points (Figure 2.2C, larger dots) was selected to result in realistic numbers of branch and termination points per layer when connected. These target points were then connected using the optimal wiring algorithm, which results in specific portions of target points becoming branch, continuation, or termination points in the tree depending on the balancing factor (Cuntz et al., 2012) (Figure 2.2D). Spatial jitter of two different spatial

frequencies was added to reproduce the tortuosity of real dendritic trees (Figure 2.2E; see Methods). Finally, a realistic quadratic tapering in diameter was mapped onto the dendritic topologies (Figure 2.2F), based on both the tapering present in real granule cells and previous work showing that a quadratic taper optimizes synaptic democracy (Cuntz et al., 2007), or the equalization of current transfer between all dendritic locations and the root. This process was then repeated for each GC in the DG, varying the parameters to reproduce the variability in the resulting population (details in Methods).
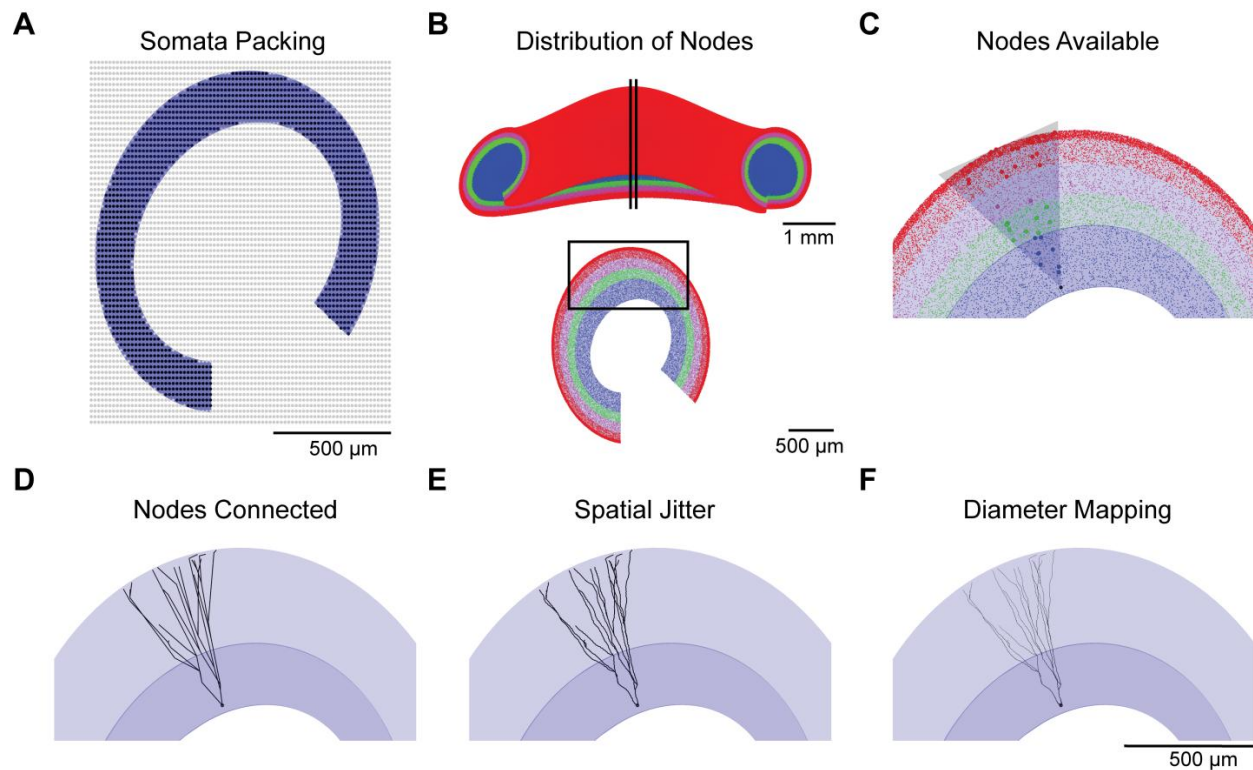
Figure 2.2. Individual steps in the generation process of granule cell dendritic morphologies. (**A**) Spheres with a 12.54 µm diameter were distributed on a closed hexagonal grid in the volume of the entire GCL, and packed spheres inside the GCL (black dots) were kept and outside the GCL (grey dots) were discarded, leaving a tightly packed arrangement for somata within the GCL volume. A 20 µm transverse slice with one layer of somata is shown for illustration. (**B**) Target points are distributed in the GCL (blue), IML (green), MML (magenta), and OML (red). Model dentate gyrus full structure (top) and a transverse 200 µm slice (bottom) are shown for illustration. The location of the slice is depicted by the vertical black lines. The black box represents the viewpoint for subsequent panels. (**C**) Target points lying within an elliptical cone are selected from the pool of available target points, and a subset of these target points is selected to generate the tree (larger points). (**D**) Target points are connected to minimize total dendritic length and path lengths in the tree. (**E**) Spatial jitter is added to reproduce the tortuosity of branches observed in real reconstructions. (**F**) Diameter values consistent with a quadratic taper toward the dendritic tips were mapped onto the resulting synthetic dendritic morphologies.

Validation of synthetic dendritic trees

Synthetic GC dendritic trees were statistically and visually indistinguishable from real GCs. Since the generative wiring algorithm connects target points to form tree structures, it is an important validation of the procedure that both the laminar distribution of branch points and of dendritic length in the synthetic GC population matched the experimental data (Claiborne et al.,

33

1990) (Table 2.1). Example dendritic topologies are shown in Figure 2.3A. Experimental reconstructions and synthetic dendritic trees had similar branching properties, exemplified by the classical Sholl analysis (Sholl, 1953) (Figure 2.3B), for which the number of intersections between the dendrite and a sphere of increasing diameter centered on the dendrite root are counted. Also, the distributions for contraction values (the ratio of Euclidean distances and path distances for all branches in the tree) were similar between reconstructed and synthetic GCs (Figure 2.3C), validating the balancing factor between costs of total dendrite length and path distances in the synthetic trees as well as the added spatial jitter. Because diameter measurements are not available for our reference GC morphologies (Claiborne et al., 1990), the diameter tapering was constrained to a more recent set of experimental reconstructions (Buckmaster, 2012a) independent of the context-dependent study. The match of the diameter tapering between reconstructed and synthetic GCs is visualized in Figure 2.3D. The branching structure and diameter tapering of the synthetic trees were thus indistinguishable from experimental reconstructions.

Table 2.1. Laminar distribution of branch points and total dendritic length for the synthetic GC

population and experimental reconstructions.

Sublayer	Percent Branch Points		Percent Total Dendritic Length	
	Synthetic Population	Experimental Values	Synthetic Population	Experimental Values
IML	61 ± 14	63 ± 14	29 ± 6	30 ± 7
MML	27 ± 13	27 ± 14	32 ± 3	30 ± 7
OML	12 ± 7	10 ± 7	39 ± 5	40 ± 7

Branch points and dendritic length in the GCL were included in the IML values, as was done in

the experimental study.
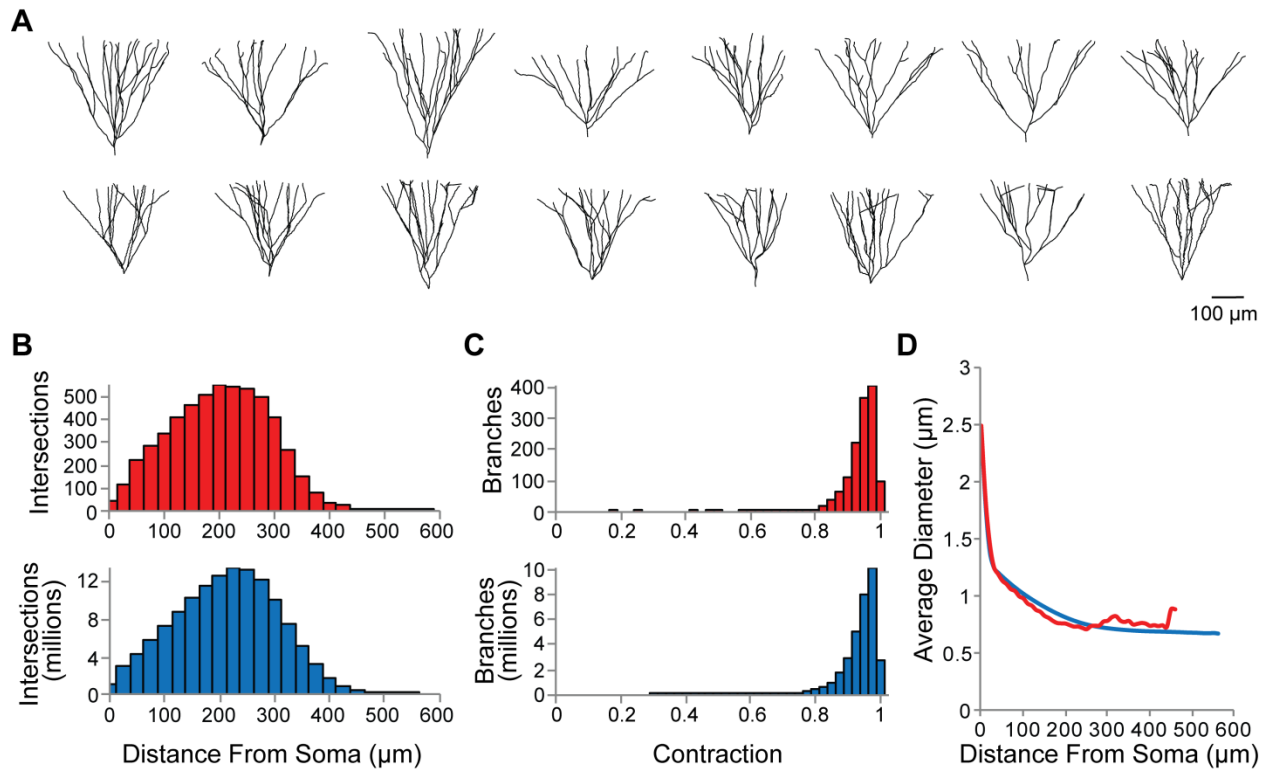
Figure 2.3. Validation of synthetic dendritic morphologies. (**A**) Example reconstructed (top row) and synthetic dendritic topologies (bottom row). (**B**) Sholl analysis plots for reconstructed (red) and synthetic dendritic trees (blue). (**C**) Contraction value distributions (ratio between Euclidean distance and path distance) for all branches in reconstructed (red) and synthetic dendritic trees (blue). (**D**) Average diameter versus distance from the soma for reconstructed (red) and synthetic dendritic trees (blue).

Matching known context-dependent features

The complete forest of 1.19 million synthetic GC dendritic trees was constructed by varying the parameters in the generation process (i.e., cone radii, number of stems, total number of nodes, laminar distribution of nodes, balancing factor, amplitude of spatial jitter, and diameter taper) for each individual GC. The resulting properties of the complete population matched values from reconstructed granule cells (Table 2.2), with small differences arising from a different relative composition of GCs from context-dependent subgroups. Significant differences have been described in GC dendritic morphology depending on the location of the soma within the GCL, i.e. for GCs with somata in the suprapyramidal versus infrapyramidal blade as well as

36

in the deep versus superficial parts of the GCL (Claiborne et al., 1990). Accordingly, choosing parameters in the generation process based on the location of each generated granule cell somata allowed for each statistically significant context-dependent difference reported previously to be recreated in the synthetic tree population (Table 2.3, $p < 0.001$ for all comparisons, Student's t-test). For example, the balancing factor for the suprapyramidal deep granule cells was set to 0.9 to match the higher maximum branch order, which was lower than the 1.35 value used for suprapyramidal superficial granule cells and the 1.22 value used for infrapyramidal granule cells. The lower balancing factor in the suprapyramidal deep subgroup signifies that minimizing dendritic length is more important for these cells. A complete and realistic population of 1.19 million context-dependent GC dendritic trees was created that matched the observed biological variability and recreated context-dependent differences, in addition to fitting within a realistic three-dimensional DG structure (Figure 2.4A-C). The distribution of these trees within the neuroanatomical space enables the study of the input organization and spatial occupancy of the complete GC forest.

Table 2.2. Overall properties for the synthetic GC population and experimental reconstructions.

Parameter	Synthetic Population (n = 1,185,178)	Experimental Values
# Dendrites	1.8 ± 0.9	1.9 ± 1.4[1]
# Dendritic Branches	28 ± 5	29 ± 7[1]
Max Branch Order	5.7 ± 0.8	5.7 ± 0.7[1]
Transverse Spread (μm)	309 ± 77	325 ± 76[1]
Longitudinal Spread (μm)	173 ± 40	176 ± 42[1]
Total Dendritic Length (μm)	3,357 ± 691	3,221 ± 540[1]
Mean Pathlength to Terminal Tips (μm)	378 ± 62	346 ± 60[2]
Mean Intermediate Branch Length (μm)	86 ± 18	72 ± 17[2]
Mean Terminal Branch Length (μm)	149 ± 32	148 ± 38[2]
Topological Asymmetry	0.45 ± 0.02	0.41 ± 0.02[2]

1 Reported literature value (n = 48)
2 Extracted from experimental reconstructions (n=43)

Table 2.3. Generation process recreates location-specific differences observed between subgroups of granule cells in experimental reconstructions.

Parameter	Subgroup	Synthetic Population	Experimental Values
# Dendritic Branches	Suprapyramidal	30 ± 5	31 ± 5
	Infrapyramidal	26 ± 4	27 ± 4
Total Dendritic Length (µm)	Suprapyramidal	3,580 ± 671	3,478 ± 482
	Infrapyramidal	3,071 ± 606	2,793 ± 314
# Dendrites	Suprapyramidal Superficial	2.4 ± 1.0	2.4 ± 1.3
	Suprapyramidal Deep	1.5 ± 0.7	1.5 ± 0.7
Max Branch Order	Suprapyramidal Superficial	5.5 ± 0.7	5.5 ± 0.9
	Suprapyramidal Deep	6.4 ± 0.7	6.4 ± 1.0
Transverse Spread (µm)	Suprapyramidal Superficial	374 ± 69	378 ± 70
	Suprapyramidal Deep	290 ± 53	293 ± 53
	Infrapyramidal Superficial	302 ± 57	311 ± 59
	Infrapyramidal Deep	243 ± 60	244 ± 64
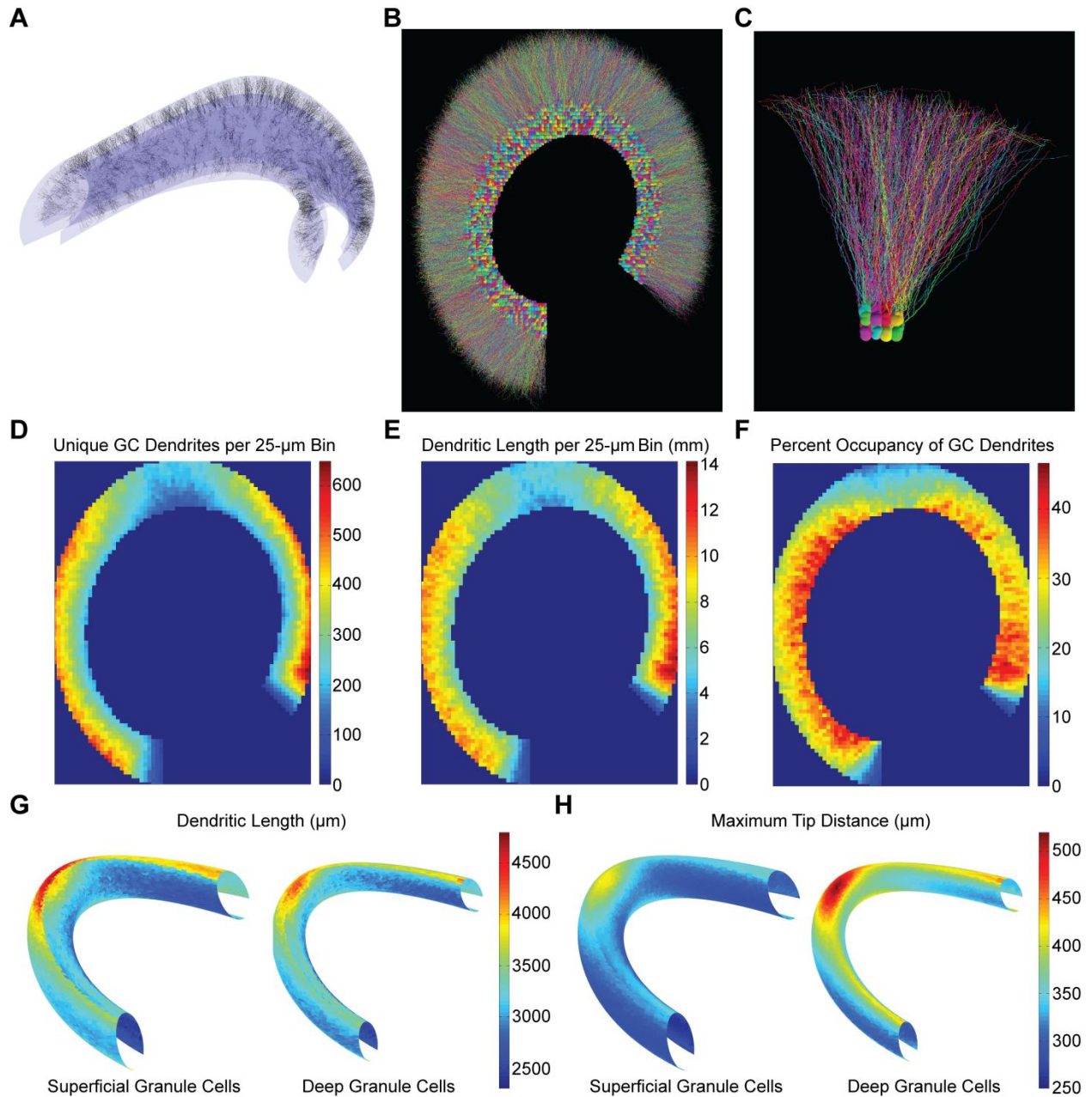
Figure 2.4. Population analysis of all synthetic granule cells in a rat dentate gyrus. (**A**) Visualization of the boundary surfaces of the dentate gyrus model structure (GCL and ML) and 1,000 synthetic dendritic trees. (**B**) Rendering of the complete morphologies for somata of all granule cells in a 20 μm transverse slice from the center of the model dentate gyrus. (**C**) Rendering of 48 granule cells from the crest of the slice in (B). (**D**) Number of unique granule cells with dendrites reaching into a given cube (25 x 25 x 25 μm) of molecular layer volume. The displayed 25-μm slice is located at the center of the model dentate gyrus. (**E**) Density of granule cell dendritic length in the same cubes as (D). (**F**) Percent volumetric occupancy of granule cell dendrites in the same cubes as (D). (**G**) Average dendritic length plotted against the position in the granule cell layer for deep and superficial granule cells. (**H**) Same as (G) but for the average maximum distance between the soma and dendritic tips.

40

Population-level analyses

In the following, we show how simple analyses that become possible with such a model can be informative about the network constituency in the hippocampus and about the location-specific distances of dendritic structure within the DG volume. An important question regarding the connectivity in the circuit is to know how many unique GCs an axonal arborization would reach within a given volume of the molecular layer. This can now simply be visualized as exemplified for a sample transverse slice from the center of the dentate gyrus (Figure 2.4D), divided into 25 μm cubic volumes. The overlap of dendrites from unique GCs in each sample volume (312 ± 114 GCs, range 45 to 650) is a small portion of the 1.19 million GC population, signifying that the macroscopic neuroanatomy of the DG promotes a sparse connectivity. This large range also results in a diverse amount of complexity required for an axon to arrive within 5 μm of all GCs in the sample cubic volumes (64 ± 22 branch points, range 17 to 142, see Methods for axon construction details). The distribution was location dependent, as there was a greater overlap in unique GC dendrites in the OML versus the IML, which coincides with the increased dendritic length in the OML (Table 2.1) and an increased cable density, i.e. dendritic length per volume (Figure 2.4E). The volume occupied by the GC forest, on the other hand, decreased toward the OML (Figure 2.4F), signifying that the increased cable density in the OML does not counteract the diameter tapering implemented into synthetic GC dendrites. The overlap of unique GCs, cable density, and volume occupied by GC dendrites were larger in the supra- and infrapyramidal blades as opposed to the crest, which is in accordance with the increased ML volume at the crest reported in the experimental reconstruction (Ropireddy et al., 2012). There were significant positive correlations between the overlap of unique GC dendrites, cable density, and volume occupied (Figure S2.2, $p < 0.001$). However, the correlation between the number of

unique GC dendrites and cable density ($r = 0.95$) was much stronger than the correlation between the number of unique GC dendrites and volume occupied or the cable density and volume occupied ($r = 0.27$ and 0.50, respectively). This likely resulted from the implemented variability in diameter tapering.

While the occupancy features impact strongly on network connectivity, measures of dendritic morphology that vary along with spatial coordinates in the DG impact strongly on the electrotonic constituency and resulting dendritic computation and synaptic integration in individual GCs. Using our complete population model, we can compare simple measures such as total dendritic length (Figure 2.4G) and maximum tip distances (Figure 2.4H) in a location-dependent manner. Even ignoring the difference between GCs from the suprapyramidal and infrapyramidal blades since these were directly incorporated into the model, the total dendritic length varied by a factor of 2x between the most distal septal or temporal tips of the DG as compared to the center of the model. The transverse axis, or size of the "C"-shape, is higher toward the center compared to the septal and temporal tips in the experimental reconstruction (Ropireddy et al., 2012), so the GCs in the center have an increased length in order to reach the outer edge of the OML. GCs with somata deep in the GCL had less variability in total length compared to the GCs with somata in more superficial parts of the GCL (Figure 2.4G). As expected, maximum tip distances in deep GCs were longer than in superficial GCs (Figure 2.4H).

We therefore have provided here simple measures linking the macroscopic scale of the DG volume with the microscopic details of single neuron morphologies and extracted useful information for network connectivity and neural computation. In future studies, novel population-level measures can be designed and tested utilizing this framework as a foundation.

Discussion

In the present study, we used a realistic structural context based on a reconstructed rat dentate gyrus (Ropireddy et al., 2012) to drive the generation of dendritic trees with a recently developed algorithm based on optimal wiring constraints (Cuntz et al., 2007;Cuntz et al., 2008). By varying the relatively few parameters in the generation process, we were able to reproduce the observed biological variability in the morphology of dentate gyrus granule cells and match key location-specific differences. While some properties were obtained from parameter optimization, several features were emergent and not the result of direct parameter constraints, including the total dendritic length, branch lengths, path lengths, and asymmetry in Table 2.2 as well as the Sholl intersections in Figure 2.3. In addition, all population-level measures, such as the cable density, are emergent properties.

The set of synthetic dendritic trees represents the largest collection of realistic morphologies to date, a complete forest of 1.19 million granule cell dendritic trees, with each tree requiring less than two seconds to be constructed. The method that we devised enables population-level analysis, and we can link the larger neuroanatomical features with the resulting branching characteristics. Due to the small number of existing reconstructions that are registered to a macroscopic context and the limited information about the properties of granule cells in the crest, granule cells were split into subgroups differentiating infrapyramidal versus suprapyramidal and deep versus superficial granule cells based on previous reconstructions (Claiborne et al., 1990), and a single balancing factor parameter was specified for each group. As more context-aware reconstructions become available, this abrupt transition can be modified to create a more continuous variation of the parameters. The speed conferred by utilizing parallel

computing in the generation process and the relatively few parameters involved provide flexibility to incorporate future experimental observations to improve the model.

While the current model provides a valuable framework for the exploration of macroscopic and microscopic neuroanatomical links, there are inherent simplifications that deviate from the biological condition that should be improved upon in future studies. The current generation process allows for multiple dendrites to occupy the same point in space, so a form of avoidance could be implemented into the spatial tortuosity, instead of solely low-pass filtered noise, in order to create a more realistic spatial occupancy. In addition, the packing of spherical somata can be improved to implement the variable and tightly-packed elliptical somata observed in experimental studies (Claiborne et al., 1990). The current study also does not include the newborn granule cells, which constitute approximately 10% of the total granule cell population (Imayoshi et al., 2008), transiently exhibit basal dendrites (Seress and Pokorny, 1981;Lübbers and Frotscher, 1988;Schmidt-Hieber et al., 2004), and possess a significantly smaller total dendritic length (Schmidt-Hieber et al., 2004). This subpopulation has recently come under intense focus for their unique participation in hippocampal network functions (Zhao et al., 2008;Gu et al., 2012;Akers et al., 2014), and the neuroanatomical properties of this subpopulation could be contrasted with the more numerous mature granule cells constructed in this study.

The linking of macroscopic and microscopic neuroanatomy presented in this study provides a framework that can be expanded upon with additional cell types and axons, but it also provides an avenue to link neuroanatomical features with electrophysiological function. The breadth of anatomical data being collected, including recent experimental reconstructions of excitatory mossy cells (Buckmaster, 2012a) and inhibitory interneurons (Norenberg et al.,

2010;Savanthrapadian et al., 2014) in the dentate gyrus, will make it possible to construct even more biologically realistic DG models. In addition, the context-driven generation methodology can be applied to axons to create realistic connectivity for comparison to the growing connectomics literature. As noted in the introduction, dendritic morphology can have a dramatic impact on electrophysiological function, and the framework provided in this study allows for this relationship to be studied on the level of the complete population. All generated morphologies can be exported to simulation environments (Cuntz et al., 2011) for the insertion of ion channel conductances or other biophysical mechanisms. For the example case of granule cells, the measured properties of dendritic integration (Schmidt-Hieber et al., 2007;Krueppel et al., 2011) and action potential initiation (Schmidt-Hieber and Bischofberger, 2010) should serve as valuable constraints. This structure and function relationship can eventually be linked to both the macroscopic neuroanatomical and network context.

Methods

The model dentate gyrus structure and granule cell synthetic trees were created and analyzed in MATLAB using the TREES toolbox (Cuntz et al., 2010;2011) on University of California Irvine's High Performance Computing cluster. The model structure and generation process will be made available at ModelDB (http://senselab.med.yale.edu/ModelDB/). The standard deviations for the literature values (Claiborne et al., 1990) were determined by multiplying the reported standard error by the sample size. All values are presented as mean ± standard deviation.

Model dentate gyrus structure

The following parametric equations defined the layer boundaries:

$$x = -500 \cdot \cos(u) \cdot (5.3 - \sin(u) + (1 + 0.138 \cdot L) \cdot \cos(v))$$

$$y = 750 \cdot \sin(u) \cdot (5.5 - 2 \cdot \sin(u) + (0.9 + 0.114 \cdot L) \cdot \cos(v))$$

$$x = 2{,}500 \cdot \sin(u) + (663 + 114 \cdot L) \cdot \sin(v - 0.13 \cdot (\pi - u))$$

where v defined the "C"-shape and ranged from -0.23π to 1.425π, u defined the septotemporal extent and ranged from 0.01π to 0.98π for the GCL and -0.016π to 1.01π for the ML, and L defined the layer and was -1.95 for inner GCL, 0 for outer GCL, 1 for IML, 2 for MML, and 3 for OML. The experimental reconstruction GCL volume was calculated based on the average 0.6 GCL to hilus volumetric ratio and their combined volume of 6.30 mm^3 (Ropireddy et al., 2012). The experimental value for the molecular layer width was determined by combining the means and standard deviations for the infrapyramidal and suprapyramidal group measurements (240 ± 17 and 254 ± 3, respectively) reported in a previous study (Claiborne et al., 1990). The model ML width was determined by distributing 2 million points on the outer GCL and OML boundary, and then calculating the closest distance to the OML boundary from 10,000 randomly sampled outer GCL points.

Synthetic dendritic tree generation

In order to recreate the context-dependent differences in the synthetic tree population, the size of the elliptical cone, number of stems, total number of nodes, and balancing factor governing the wiring were modified based on the location of each soma. Superficial neurons were defined as having somata in the half of the GCL closest to the ML, whereas deep neurons had somata in the half farthest from the ML. The infrapyramidal/suprapyramidal split was

located halfway around the characteristic "C"-shape of the transverse slice of the dentate gyrus, which was defined by the midpoint of the v parameter in the GCL boundary equation. The number of stems was set by sampling from a truncated Poisson distribution and ranged from 1 to 4, as observed in experimental reconstructions (Claiborne et al., 1990;Buckmaster, 2012a). The elliptical cone was oriented by pointing the center axis toward the closest of two million points distributed on the OML boundary and orienting the longitudinal and transverse elliptical cone radii within the structure. The transverse spread of generated GCs was analyzed by orienting cells based on their mean transverse axis and measuring the distance between the outermost dendritic tips. The widest spread in the majority of granule cells is reported to be close to the transverse axis (Claiborne et al., 1990), so the elliptical cone transverse radius was set greater than the longitudinal radius in the generation process. All trees were resampled to a 5 μm fixed segment interval, and low-pass filtered homogenous spatial noise was applied to all points similar to previous methods (Cuntz et al., 2010), using length constants of 10 μm and 50 μm. Diameter mapping was implemented using a variable quadratic tapering from previous studies (Cuntz et al., 2007;Cuntz et al., 2010) and adding an additional scaling function $\exp(x) - 1$, where x is the distance from the soma, to better approximate the initial diameter taper close to the soma. Experimental reconstructions (Claiborne et al., 1990) used in the target point laminar distribution estimation (see Supporting Information) and synthetic tree validation were obtained from the NeuroMorpho.Org database (Ascoli et al., 2007).

Population-level analyses

The ray-tracing images in Figure 2.4B-C were created with the Persistence of Vision Ray tracer (POV-ray) software (http://www.povray.org/download/). The location of dendrites within

each 25 μm cube was determined by testing the points in each dendritic tree, which specify the center of each segment. Because the granule cell dendritic trees were resampled at 5 μm before the spatial jitter addition, the length and volume measurements within each cubic volume are approximations. To get an estimate of the complexity required for an axon to contact all granule cell dendritic trees invading each cubic volume, random points were selected for each cubic volume and connected using the optimal wiring algorithm with a balancing factor of zero (to minimize total dendritic length). The number of target points was increased until the simulated axon reached within 5 μm of all granule cell dendritic trees present in the each volume. The results from 10 different random collections of target points were averaged together to determine the complexity required (number of branch points) for each cubic volume. In order to map the dendritic length and maximum tip distance onto the GCL, triangulations of the inner and outer GCL surfaces were created with 5000 faces, and the closest face for all trees was determined. The values for the trees associated with each respective face were then averaged together.

Supplemental Material

Text S2.1. Estimation of target point laminar distribution.

Laminar distribution of target points for synthetic granule cell generation

The optimal wiring algorithm connects input target points and allocates each point as a branch, continuation, or termination point in the final structure. The number of target points and their laminar distribution were thus required to generate dendritic morphologies in the model dentate gyrus structure. These parameters were estimated from three-dimensional dendritic reconstructions of 43 granule cells, which were performed in 400-μm slices and contained no cut dendrites in the IML and two or less cut dendrites in the MML and OML (Claiborne et al., 1990). Only branch and termination points were summed together to estimate target points in the reconstructions, because continuation points are a part of the generation process and do not have significance in the reconstructions. The dendritic reconstructions had an average of 32 total branch and termination points, which slightly underestimates the average number of target points required in the generation process due to the lack of continuation points. To extract the laminar distribution estimate, reconstructions were rotated and size-normalized. All experimental reconstructions were originally performed perpendicular to the longitudinal axis of the dentate gyrus, so they were only rotated in the transverse plane to orient their mean transverse axis and then their outermost dendritic tips (Figure S2.1A). The reconstructions were then scaled to the average limits in all three directions to produce size-normalized dendritic trees (Figure S2.1B), as done previously (Cuntz et al., 2010). Branch and termination points were then grouped into layers based on their distance from the base of the normalized trees, choosing the maximum normalized tree height as the edge of the molecular layer and the molecular layer width as the average experimentally determined value of 249 μm (Claiborne et al., 1990) (Figure S2.1C).

This resulted in estimated proportions of 14%, 14%, 12%, and 60% for the GCL, IML, MML, and OML, respectively. Because virtually all granule cell dendrites extend toward the OML boundary (Claiborne et al., 1990), points in the OML were preferentially distributed in the outer fourth of the layer, according to a 2:1 ratio measured in the estimation process. This weighted distribution in the outer portion of the OML was crucial to achieve the correct laminar distribution of the total dendritic length (see Table 2.1). The inclusion of the billions of points available in the model dentate gyrus structure as possible target points in the generation process would be computationally expensive, even with parallel computing, and is not necessary for the 1.19 million neurons being generated. The complete set of points located within the model GCL and ML was first determined at a 1 μm interval, and a subset of 200 million random points was chosen from the GCL and the sublayers of the ML according to the laminar distribution extracted above. The selection of target points in the final generation process was $14 \pm 4.1\%$ in the GCL, $13 \pm 4.1\%$ in the IML, 11.5% in the inner OML, 48% in the outer OML, and the remaining percentage, on average 13.5%, in the MML.
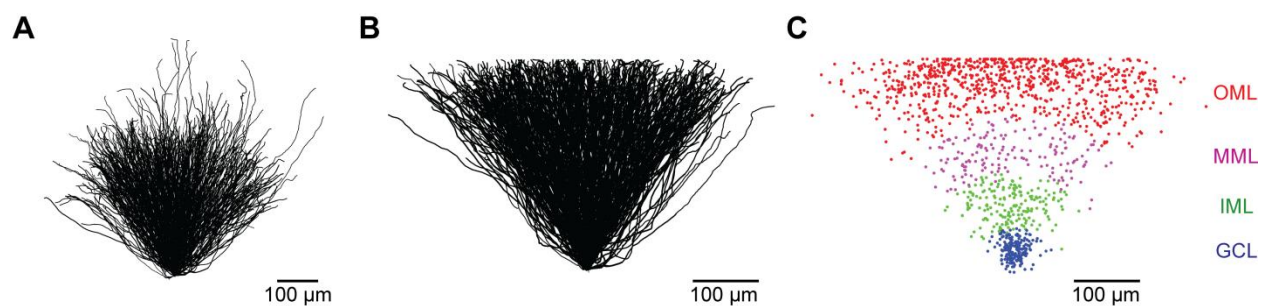
Figure S2.1. Branch and termination point distributions estimated from experimental dendritic tree reconstructions. (**A**) Overlay of rotated three-dimensional reconstructions of 43 granule cell dendritic morphologies. (**B**) Size-normalized dendritic morphologies scaled to the average limits in all three dimensions. (**C**) Distribution of branch and termination points in each layer. GCL – granule cell layer (blue), IML – inner molecular layer (green), MML – middle molecular layer (magenta), OML – outer molecular layer (red).
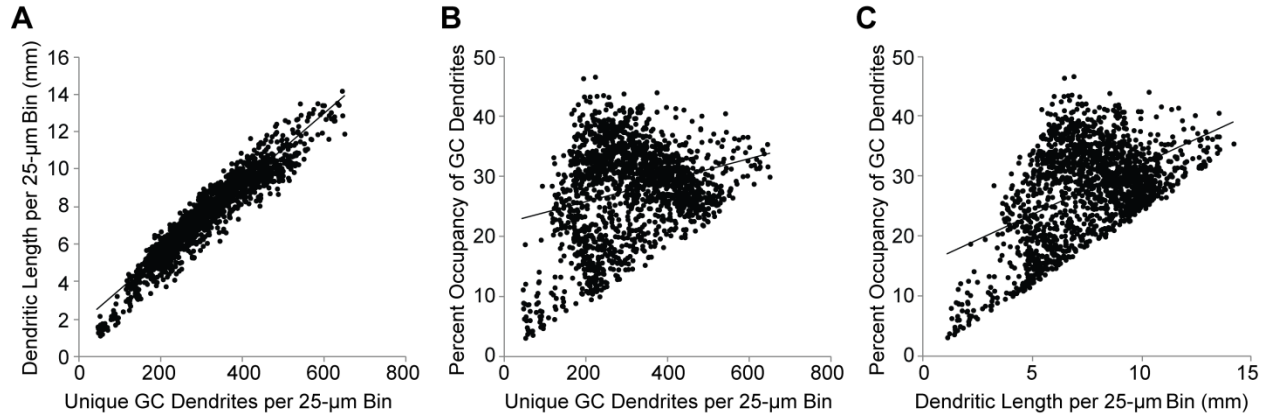
Figure S2.2. Correlations between occupancy measures. (**A**) Number of unique granule cells with dendrites reaching into a given cube (25 x 25 x 25 µm) versus the cable density. Cubic volumes are the same as in Figure 2.4D-F. (**B**) Number of unique granule cells with dendrites reaching into a given cube versus percent volumetric occupancy in the same cubes as (A). (**C**) Cable density versus percent volumetric occupancy in the same cubes as (A).

CHAPTER 3

Radiation Alters Intrinsic and Synaptic Properties of CA1 Pyramidal Neurons of the Hippocampus

Abstract

High-energy protons constitute at least 85% of the fluence of energetic ions in inter-planetary space. While protons are only sparsely ionizing compared to higher atomic mass ions, protons could significantly contribute to the delivered dose and affect astronaut central nervous system function at high fluence, especially during prolonged deep space missions, such as to Mars. Here we report long-term effects of 1 Gy proton radiation on electrophysiological properties of CA1 pyramidal neurons in the mouse hippocampus. The hippocampus is a key structure for the formation of long-term episodic memory, for spatial orientation, and for information processing in a number of other cognitive tasks. CA1 pyramidal neurons form the last and critical relay point in the tri-synaptic circuit of the hippocampal principal neurons through which information is processed before being transferred to other brain areas. Proper functioning of CA1 pyramidal neurons is crucial for hippocampus-dependent tasks. We used the patch-clamp technique to evaluate chronic effects of 1 Gy proton radiation on CA1 pyramidal neurons. We found that radiation chronically altered the intrinsic membrane properties of CA1 pyramidal neurons at 3 months post-irradiation, resulting in a hyperpolarization of the resting membrane potential (V_{RMP}) and a decrease in input resistance (R_{in}). These small but significant alterations in intrinsic properties decreased the excitability of CA1 pyramidal neurons, and had a dramatic impact on network function in a computational model of the CA1 microcircuit. On the other hand, proton radiation upregulated the persistent Na^+ current (I_{NaP}) and increased the rate of miniature excitatory postsynaptic currents (mEPSCs). Both the I_{NaP} and the heightened rate of

mEPSCs contribute to neuronal depolarization and excitation, at least in part, compensating for the reduced excitability resulting from the radiation effects on the V_{RMP} and the R_{in}. These results show long-term alterations in the intrinsic properties of CA1 pyramidal cells following realistic, low dose proton irradiation.

Introduction

Astronauts on space missions are subjected to deleterious effects of cosmic radiation in the form of highly-penetrating charged nuclei originating from the Sun or from galactic sources. The largest component of this space radiation is high energy protons, while the remainder takes the form of high charge high energy nuclear particles (HZE) (Cucinotta et al., 1996;Badhwar and Cucinotta, 1998;Setlow, 2003). While the energy deposited by a single HZE particle is significantly higher than that by a single proton, the total radiation dose contributed by HZEs could be comparable to that contributed by the high fluence of protons.

Ionizing radiation has been shown to acutely produce an excess of free radicals, followed by a protracted shift of the tissue oxidation-reduction equilibrium state (redox state) toward oxidation and leading to oxidative stress (Giedzinski et al., 2005;Guan et al., 2006;Limoli et al., 2007;Tseng et al., 2013). Oxidative stress is thought to be the main contributing factor to the radiation-induced CNS damage, manifested as suppressed neurogenesis, neuroinflammation, and cognitive deficits in rodents (Raber et al., 2004;Rola et al., 2004;Manda et al., 2008;Yang et al., 2012). Similar cognitive and biochemical deficits associated with normal aging and the progression of neurodegenerative diseases have also been attributed to oxidative stress (Harman, 1992;Ames et al., 1993;Olanow, 1993;Hauss-Wegrzyniak et al., 2000).

One of NASA's goals is to establish the acute and long-term effects of space radiation on astronaut health, in order to define the safety limits of deep space travel. The total radiation dose accumulated by astronauts during a prolonged space mission to Mars is estimated as close to 1 Gy (Hassler et al., 2013;Zeitlin et al., 2013). In addition, a similar radiation dose might be accumulated as a result of a solar energetic particle event during an astronaut's extravehicular activity. The long-term effects of these doses of radiation on the central nervous system (CNS) are largely unknown. In this study, using electrophysiological techniques, we examined whether proton radiation at a dose of 1 Gy produced long-term alterations in principal neurons of the hippocampus in adult mice.

The hippocampus is a key structure in information processing and is crucial for long-term memory, orientation in space, and analysis of the emotional contexts of events (Milner, 1974;Squire et al., 2004). Dysfunction of the hippocampus is a major cause of a variety of cognitive deficits and dementia, and is linked to various forms of depression (DeKosky et al., 1996;Hof and Morrison, 1996;Procter, 1996;Sweatt, 2004;Kalia, 2005;Maletic et al., 2007;Calabresi et al., 2013). CA1 pyramidal neurons form the main output of the hippocampus since they relay the processed information to other brain areas. Impaired function of these neurons is associated with a number of pathologic states and diseases (Fattoretti et al., 2010;Perez-Cruz et al., 2011;Alldred et al., 2012).

We used the patch-clamp technique to evaluate long-term effects of 1 Gy proton radiation on the function of CA1 pyramidal neurons in mice. We found that proton radiation produced long-term alterations in the intrinsic and synaptic properties of CA1 pyramidal neurons, which affected neuronal excitability in an antagonistic manner. To evaluate the outcome of these alterations on the hippocampal function, we used computational modeling to simulate neuronal

activity in a microcircuit of the CA1 area, which demonstrated that radiation-induced alterations of the neuronal passive membrane properties of pyramidal cells can dramatically compromise the function of the CA1 network.

Materials and Methods

Irradiation procedure

Eight C57Bl/6J male mice (Jackson Laboratories) at 10 weeks of age were exposed to whole body 150 MeV/n protons at the James M Slater Proton Therapy Treatment and Research Center, Loma Linda University. Four mice were irradiated at a time in well-ventilated plastic holders that minimized movement. The mice were positioned in the beam line and received doses of 1.00±0.02 Gy at a dose rate of 0.55 Gy/min. Non-irradiated control mice were treated identically without being exposed to radiation. All protocols were approved by the Institutional Animal Care and Use Committees (IACUC) of LLU and were in compliance with all Federal regulations.

Slice Preparation and Electrophysiology

In vitro electrophysiological experiments were performed starting 3 months post-irradiation (6 months of age). All protocols and procedures were approved by the Institutional Animal Care and Use Committee of Loma Linda University. Mice were housed on a 12:12 h light-dark cycle at constant temperature and humidity. Prior to decapitation, mice were anesthetized with isoflurane (Webster Veterinary Supply, Inc., Sterling, MA). After decapitation, the head was placed in an ice-cold artificial cerebro-spinal fluid (ACSF) for 1.5 min. The brain was then quickly isolated, submerged in oxygenated ice-cold ACSF, and then glued on a vibratome (Leica 1000S) stage. Coronal slices (300 µm) of the rostral hippocampus were

prepared in ice-cold, dissection ACSF containing (in mM) 124 NaCl, 2.5 KCl, 1.25 NaH_2PO_4, 26 $NaHCO_3$, 1 $CaCl_2$, 2.5 $MgCl_2$, and 10 glucose (95% O_2/5% CO_2).

Slices were incubated at room temperature and used for recordings for up to 6 h after decapitation. Recordings were performed in ACSF containing (in mM) 124 NaCl, 2.5 KCl, 1.25 NaH_2PO_4, 26 $NaHCO_3$, 2 $CaCl_2$, 2 $MgCl_2$, and 10 glucose (95% O_2/5% CO_2). Unless indicated otherwise, no GABA receptor blockers or other drugs were added to the external solution. The recording temperature in the submerged chamber was 29-33°C. Cells were visualized with infrared differential interference contrast (IR-DIC) utilizing a water immersion objective (40×, 0.9 NA, Olympus). Patch pipettes were pulled from borosilicate glass tubing (1.5 mm outer diameter, 0.3 mm wall thickness) on a horizontal puller (P-97, Sutter Instruments) and used without further modifications. Pipettes were filled with internal solution of the following composition (in mM): 155 potassium gluconate, 5 NaCl, 0.5 EGTA, 0.1 $CaCl_2$, 2 MgATP, 5 HEPES, 0.3 NaGTP, 2 Phosphocreatine; pH adjusted to 7.2 with KOH. Somatic whole-cell recordings in CA1 pyramidal cells were made with a Multiclamp 700B amplifier (Molecular Devices). Most data were filtered at 2 kHz and sampled at 20 kHz with a Digidata 1440 interface controlled by pClamp Software (Molecular Devices, Union City, CA). Electrode resistance in the bath ranged from 4.5 to 8 MΩ.

The data presented here are based upon patch clamp recordings from 65 neurons located in the pyramidal layer of the CA1 area of the dorsal hippocampus. To record action potentials (APs), the cells were current-clamped at 0 pA and then depolarized by applying steps of positive currents at 5-15 pA increments. Parameters of the APs and the repolarization phases (illustrated in Figure 3.1A,B) were analyzed at minimal suprathreshold currents. Sag of the membrane potential (V_h sag) created by activation of the hyperpolarization-activated non-specific cation

current (I_h) was analyzed from traces with initial hyperpolarization to -100 mV (Figure 3.1C).

Current-clamp recordings were followed by recordings of the voltage-gated currents.

Recordings were not adjusted for the liquid junction potential prior to the analysis.
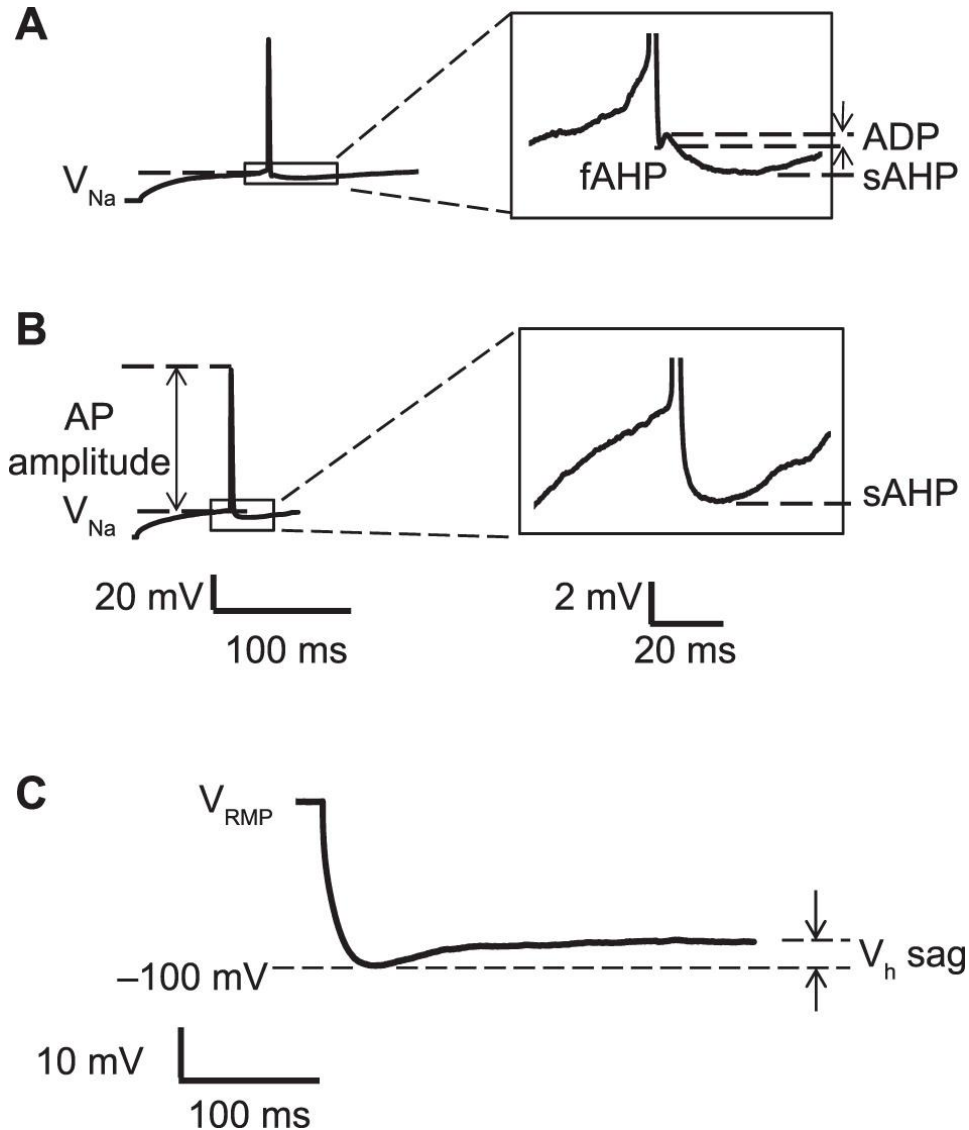
Figure 3.1. Characteristics of CA1 pyramidal neurons assessed in the patch-clamp experiments using the current-clamp mode. Examples of the triphasic (panel A) and biphasic (panel B) repolarization patterns of the action potential (AP). The resting membrane potential (V_{RMP}), threshold for activation of the Na^+ channels (V_{Na}), fast after-hyperpolarization (fAHP), after-depolarization (ADP), slow after-hyperpolarization (sAHP), action potential amplitude (AP amp) and AP width at half maximum AP amplitude (AP ½ width) were assessed in individual CA1 pyramidal neurons. Panel C: Negative currents were injected to evaluate the voltage sag reflecting activation of the nonspecific cationic current (I_h). ΔV_h was evaluated from traces with initial hyperpolarization to -100 mV.

Voltage-gated currents were induced by 400-ms long voltage steps to -105 mV to -5 mV in 10 mV increments from the initial potential of -65 mV. Neurons were not stimulated beyond -5 mV since the large amplitudes of K^+ currents at more positive voltages cannot be accurately evaluated in cells with complex morphology, where the errors arise from the space-clamp problem (Bar-Yehuda and Korngreen, 2008) and from imperfections of the capacitance and the series resistance (R_s) compensations (Marty and Neher, 1995). The leak currents were subtracted from the voltage-gated currents prior to analysis. The leak currents were calculated using the currents induced by stimulation from -65 mV to -55 mV and scaling them to the corresponding membrane voltage. To address a possible contribution of Ca^{2+}- or Ca^{2+}-dependent currents, we performed experiments in low-Ca^{2+} ACSF (0.2 mM $CaCl_2$). Whole-cell currents in low-Ca^{2+} ACSF at voltages up to -5 mV were not significantly different from those in control ACSF (2mM $CaCl_2$), indicating that the whole-cell currents at depolarized voltages were contributed mainly by the voltage-gated K^+ channels (data not shown).

In a subset of experiments, recordings in drug-free ACSF were followed by superfusion with ACSF containing tetrodotoxin (TTX, 1 µM) for 10 min after which the voltage-gated currents were recorded. Recordings in TTX-containing ACSF were done to evaluate the persistent Na current (I_{NaP}) and to isolate the fast component of the voltage-dependent K^+ currents (K_v), the A-type K^+ current (K_A).

In a separate set of experiments, mEPSCs and voltage-gated currents were recorded in TTX-containing ACSF. To avoid time-dependent changes, mEPSCs were recorded immediately after establishing the whole-cell configuration. Parameters of mEPSCs were obtained by analyzing the 2-4 min long current recordings in neurons voltage-clamped at -65 mV. It has been demonstrated in earlier studies that, at -65 mV holding potential and with the K^+ gluconate-based

internal solution, the inhibitory or other non-α-amino-3-hydroxy-5-methyl-4-isoxazolepropionic

acid receptor (AMPA) receptor currents in the CA1 pyramidal neurons are below resolution and

do not contaminate mEPSCs (Spruston and Johnston, 1992;Sokolova et al., 2006;Sokolova and

Mody, 2008). To confirm this, in a subset of experiments, mEPSC recordings were followed by

perfusion with the specific AMPA receptor blocker 6,7-Dinitroquinoxaline-2,3(1H,4H)-dione

(DNQX, 20μM). DNQX completely eliminated any negative phasic currents (Figure 3.2C),

indicating that all synaptic currents were specific for AMPA receptors. mEPSCs were analyzed

with MiniAnalysis software (Synaptosoft) using a 4 pA current threshold and an area threshold

parameter of 14, for detection of mEPSCs. All of the data analyzed with this program were also

visually controlled. Data analysis was performed blinded to the control and irradiated groups.
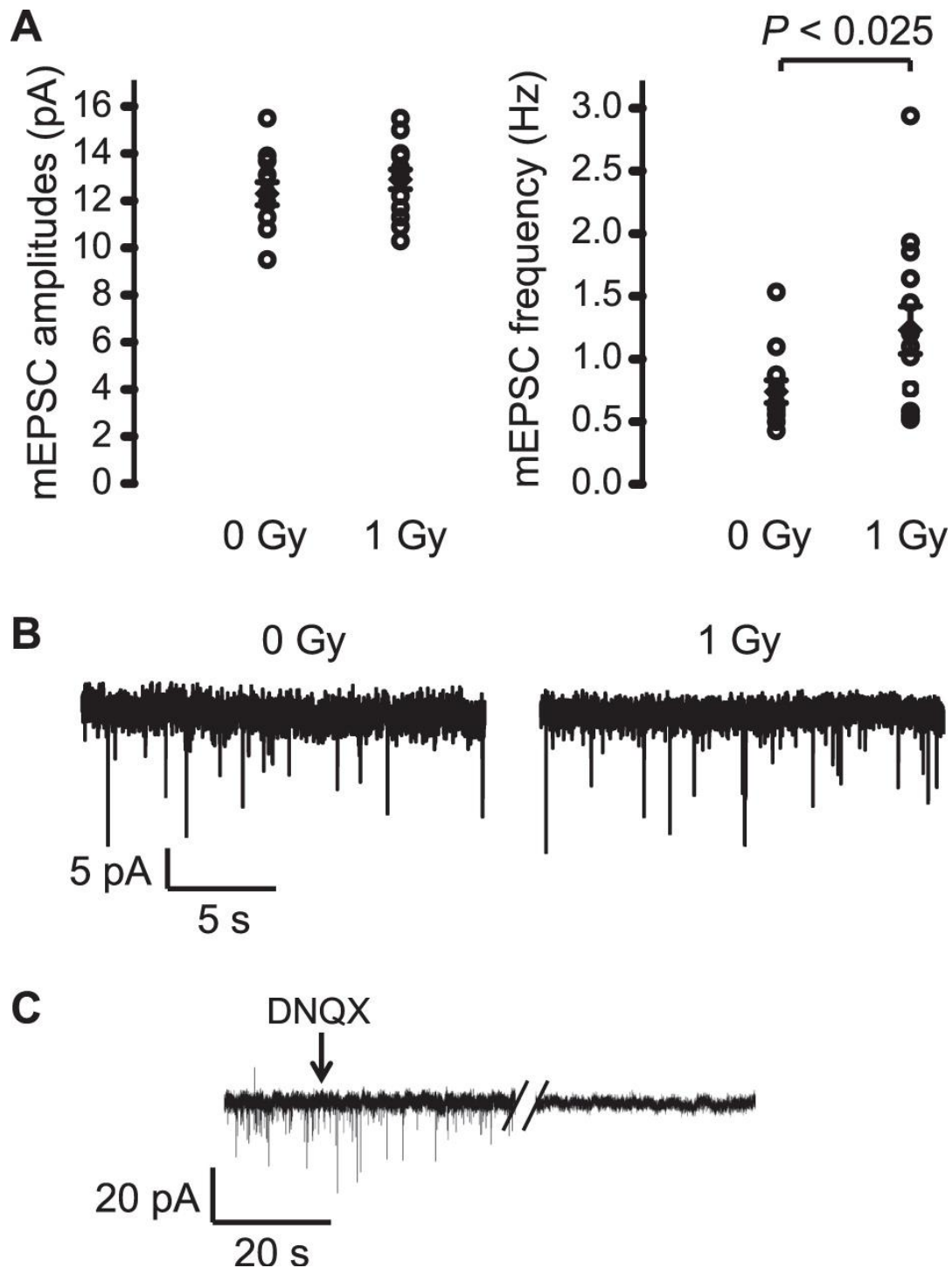
Figure 3.2. Effect of radiation on mEPSC amplitudes and frequencies. Panel A: Irradiation did not affect mEPSC amplitudes (left side) but augmented mEPSC frequencies (right side). Panel B: Representative recordings of mEPSCs in control (left side) and irradiated neurons (right side). Panel C: Specific AMPA-type receptor blocker DNQX (20 μM) eliminated all negative phasic currents, indicating that mEPSCs were specific to AMPA receptors.

The two criteria for data inclusion were possessing a resting membrane potential (V_{RMP}) more hyperpolarized than -57 mV and a series resistance (R_s) less than 23 MΩ. The R_{in} and R_s were evaluated by analyzing the steady-state and transient components of current responses to +10 mV-voltage steps applied from the holding potential of -65 mV. The lowest R_{in} was 88 MΩ. The rest of the neurons had R_{in}>100 MΩ. R_s was monitored throughout the experiments. Experiments in which R_s exceeded 23 MΩ or changed more than 20% during the recordings were excluded from the analysis. R_s ranged from 8 to 23 MΩ and was, on average, 13 ± 2.4 MΩ. Data presented are mean ± standard error and n is the number of experiments. Data were statistically evaluated using the one-tailed Student's t-test.

Computational Modeling

The computational model of the CA1 microcircuit was adapted from a recent study, which investigated the mechanisms underlying CA1 function by simulating the storage and recall of spatio-temporal patterns (Cutsuridis et al., 2010). All simulations were performed using NEURON 7.3 (Hines and Carnevale, 1997) running on a Windows PC or with 64 processors using MPI (message passing interface) on University of California Irvine's High Performance Computing cluster. The model contained multicompartmental models of 100 excitatory pyramidal cells and four types of inhibitory interneurons: 2 basket cells, 1 bistratified cell, 1 axo-axonic cell, and 1 *oriens lacunosum-moleculare* cell. Inputs to the CA1 microcircuit were provided by simulating inhibitory input from the medial septum and excitatory input from the entorhinal cortex and CA3 Schaffer collaterals, as done previously. The computational model exhibits a robust theta rhythm, and the activity of each cell type with respect to theta oscillations

is in accordance with experimental observations (Klausberger et al., 2003;Klausberger et al., 2004;Somogyi and Klausberger, 2005).

Network simulations were performed using the pyramidal cell model from the original study to simulate the control condition and a pyramidal cell model with altered passive membrane properties to simulate the irradiated condition. The control pyramidal cell model (V_{RMP} -63.8 mV and R_{in} 72.3 mΩ) was converted to the irradiated pyramidal cell model (V_{RMP} -67.9 mV and R_{in} 62.2 mΩ) by reducing the membrane resistance from 20,000 to 11,650 Ohm*cm^2 and changing the reversal potential of the leak conductance from -70 to -79.1 mV. The input resistance was measured by simulating a voltage clamp procedure that stepped from a holding potential of -65 mV to -60 mV. The recall function of the network model from the previous study was utilized, which involved providing CA3 input to only a subset (20%) of the pyramidal cells, using a previously determined spatio-temporal input pattern. Network activity was generated for 5.05 seconds (a 50 ms initial delay and 20 theta cycles). A fast Fourier transform of the pyramidal cell spike times was performed using MATLAB (The MathWorks Inc.) to measure the power of the theta oscillation in pyramidal cell activity at the peak theta frequency.

Results

Miniature excitatory postsynaptic currents

In CA1 pyramidal neurons, mEPSCs represent AMPAR-mediated post-synaptic responses to spontaneous release of individual glutamate-containing synaptic vesicles, predominantly from the CA3 pyramidal neurons. Changes in mEPSC amplitudes are commonly interpreted as the altered function of AMPA receptors. Changes in mEPSC frequency, on the

other hand, might reflect alterations in the number of functional excitatory synapses or the synaptic release probability. To evaluate the effect of radiation on glutamatergic neurotransmission, we compared mEPSCs in CA1 pyramidal neurons in both irradiated and control mice.

Mean mEPSCs amplitudes in irradiated mice were not significantly different from those in control mice (12.3 ± 0.5 vs. 12.9 ± 0.4 pA, in control and irradiated mice, respectively, n=11/13, p>0.05, t-test, Figure 3.2A, left). In contrast to mEPSC amplitudes, mEPSC frequencies were significantly higher in irradiated mice than in controls (0.74 ± 0.09 vs. 1.23 ± 0.19 Hz, in control and irradiated groups, respectively, n=11/13, t-test, p<0.025, Figure 3.2A, right).

In a subset of experiments, recordings of mEPSCs were followed by perfusion with a specific AMPA receptor blocker DNQX (20 µM). In all experiments, DNQX eliminated the miniature events of negative polarity, indicating that they were specific to the AMPA-type glutamate receptors (Figure 3.2C).

Passive membrane properties, V_h and parameters of the AP

Neuronal excitability is determined, in part, by neuronal passive membrane properties. We sought to establish whether radiation affected the R_{in}, a measure of neuronal membrane resistance, and the V_{RMP}, two characteristics that control neuronal excitability. Both the R_{in} and the V_{RMP} were altered by proton radiation. Radiation significantly reduced the R_{in} and shifted the V_{RMP} of the CA1 pyramidal neurons toward more negative potentials (Table 3.1, Figure 3.3A,B). The difference in the passive membrane properties could potentially be contributed by a time-dependent signal run-down in whole-cell patch-clamp recordings. To avoid these time-dependent

changes, the R_{in} was recorded immediately after obtaining the whole-cell configuration (the start

of the experiment), while the V_{RMP} was recorded within 10 min of the start of the experiments.

There was no correlation between the V_{RMP} and the recording time, and the mean V_{RMP} recording

time was not significantly different between the control and irradiated groups, indicating that

time-dependent changes introduced by the whole-cell configuration of the patch-clamp

experiment did not contribute to the observed difference in the passive membrane properties

between the control and the irradiated groups (see Supplementary Figure S3.1).

Table 3.1. Summary of the Passive Membrane Properties and the Characteristics of the CA1 Neurons Obtained in the Current Clamp Mode

Gy	V_{RMP} (mV)	R_{in} (MΩ)	V_{Na} (mV)	fAHP (mV)	ADP (mV)	sAHP (mV)	AP amp (mV)	AP ½ width (ms)	V_h sag (mV)
0	-63.2 ± 0.78	156.3 ± 7.9	-37.5 ± 1.0	-41.6 ± 1.0	0.3 ± 0.1	-45.2 ± 1.1	94.0 ± 2.2	1.17 ± 0.03	7.1 ± 0.5
	n = 18	n = 16	n = 16	n = 10	n = 10	n = 16	n = 16	n = 16	n = 17
1	-67.4 ± 0.58	134.4 ± 6.0	-39.1 ± 1.5	-38.8 ± 1.7	0.3 ± 0.1	-45.9 ± 1.3	92.3 ± 1.9	1.17 ± 0.03	6.0 ± 0.24
	n = 16	n = 17	n = 15	n = 7	n = 7	n = 15	n = 15	n = 15	n = 17
	$P < 0.0002$	$P < 0.02$							$P < 0.025$

Notes. V_{RMP}: resting membrane potential. R_{in}: input resistance. fAHP: fast after-hyperpolarization. ADP: after-depolarization, which follows the fAHP. sAHP: slow after-hyperpolarization. V_{Na}: threshold for activation of the fast Na^+ current. AP amp: action potential amplitude. AP ½ width: width at half AP amplitude. V_h sag: sag of the membrane potential at hyperpolarizations to -100 mV. n: number of experiments. *P*: significance of the *t* test analysis of sample differences (*P* indicated only for significantly different results; $P < 0.05$).
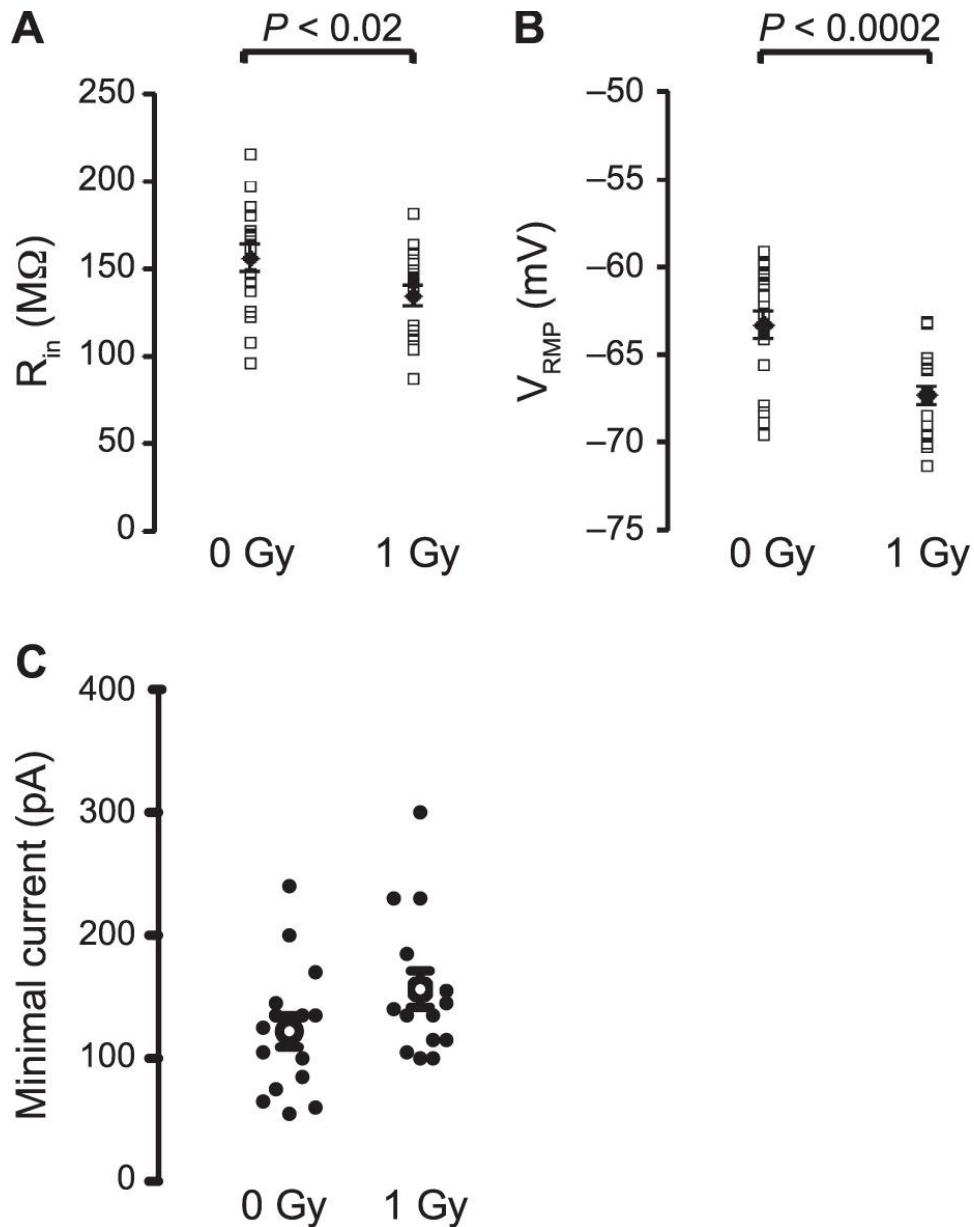
Figure 3.3. Passive membrane properties of CA1 pyramidal neurons were altered in irradiated mice. Reduced R_{in} (panel A) and hyperpolarized V_{RMP} (panel B) in CA1 pyramidal neurons from irradiated mice. Both of these altered passive membrane properties suppress neuronal excitability. Panel C: The minimal suprathreshold current in irradiated neurons was not significantly higher than in the control neurons ($P = 0.055$, t test, n = 14/15).

The shape of the AP is determined by the specific properties and relative contributions of membrane voltage-gated currents. Changes in these currents might be reflected in the characteristics of the APs. We compared the APs in CA1 pyramidal neurons from the control and irradiated groups of mice. The following parameters of the APs were evaluated: the magnitudes

of the fast and slow afterhyperpolarizations (fAHP and sAHP, respectively) and the afterdepolarization (ADP), the threshold for the Na^+ current activation (V_{Na}), the AP half-widths, and the AP amplitudes (Figure 3.1). About 40% of the tested neurons in both groups displayed the three-phase repolarization of the AP revealing the fAHP, ADP and sAHP (Figure 3.1A). In the rest of the neurons, repolarization was bi-phasic with the sAHP as the only characteristic of the repolarizing phase (Figure 3.1B). All characteristics of the APs were similar in neurons from the control and irradiated groups. There was no significant difference in the R_s between the neurons with the tri-phasic and the bi-phasic patterns of AP repolarization (14.6 ± 0.4 vs. 15.9 ± 0.8 MΩ, respectively).

V_h sag, which is contributed by activation of the hyperpolarization-activated non-specific cation conductance, was measured in recordings showing initial hyperpolarization to approximately -100 mV (Figure 3.1C). There was no significant difference between the injected currents required for the initial neuronal depolarization to -100 mV in the control and the irradiated groups (-325.9 ± 15.4 pA vs. -314.1 ± 15.5 pA, respectively). However, V_h sag was significantly smaller in neurons from irradiated mice (Table 3.1). Since radiation did not affect the I_h current (see below), the decreased V_h sag in irradiated neurons, most likely, reflects radiation-induced reduction of the R_{in}.

Both reduction of the R_{in} and hyperpolarization of the V_{RMP} alter neuronal excitability, or the propensity of neurons to respond to depolarizing stimuli by generating an AP. In order to assess excitability in the two groups of neurons, we compared the minimal currents required for stimulation neuronal spiking activity (minimal suprathreshold currents, see Methods). Minimal suprathreshold currents in irradiated neurons were not significantly higher than those in control ($p = 0.055$, t-test, n = 14/15, Figure 3.3C).

Voltage-gated currents

Voltage-gated currents induced by either hyperpolarizing or depolarizing command steps were compared in non-irradiated and irradiated mice. Voltage-activated membrane currents were examined in ACSF supplemented with TTX to eliminate the contribution of the Na^+ currents. Currents induced by the hyperpolarizing voltage steps consist primarily of the non-selective hyperpolarization-induced cation current (I_h). Depolarizing voltage steps induced fast, A-type (K_A), and slow, delayed rectifier (K_{DR}), K^+ currents (Figure 3.4B). Neither depolarization- nor hyperpolarization-induced K^+ currents were affected by radiation (Figure 3.4A).
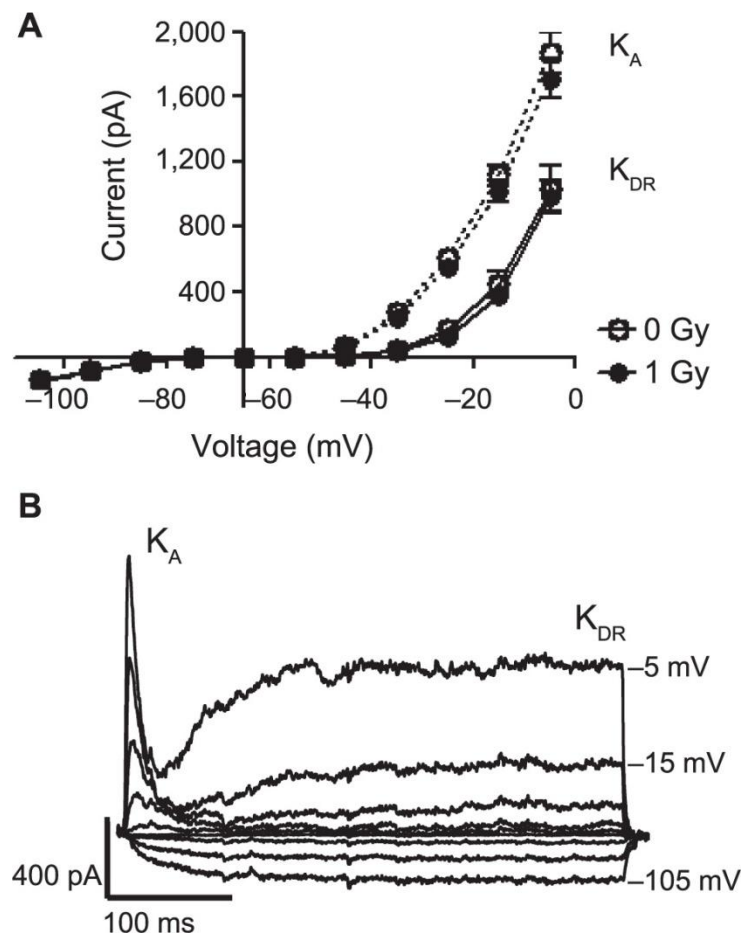
Figure 3.4. Panel A: Whole-cell voltage gated K^+ currents K_A and K_{DR} were not affected by irradiation. Panel B: Representative voltage-gated currents after the leak and capacitance current subtraction demonstrating the K_A and K_{DR}.

In drug-free ACSF, the steady-state currents at voltages from -35 mV to -15 mV were significantly attenuated when compared to the ones in TTX (Figure 3.5B). The TTX-sensitive non-inactivating negative conductance was contributed by the persistent Na^+ current (I_{NaP}). The presence of I_{NaP} could also be demonstrated during a slow voltage ramp command (60 mV/ 14 s, Figure 3.5C). Slow membrane depolarization during the voltage ramp suppressed the fast Na^+ current revealing a region of negative conductance which was eliminated by TTX. I_{NaP} was significantly larger in the irradiated group than that in the control (-148.6 ± 25.1 pA vs. -78 ± 12.5 pA at -25 mV, n=11, t-test, p<0.03, Figure 3.5A).
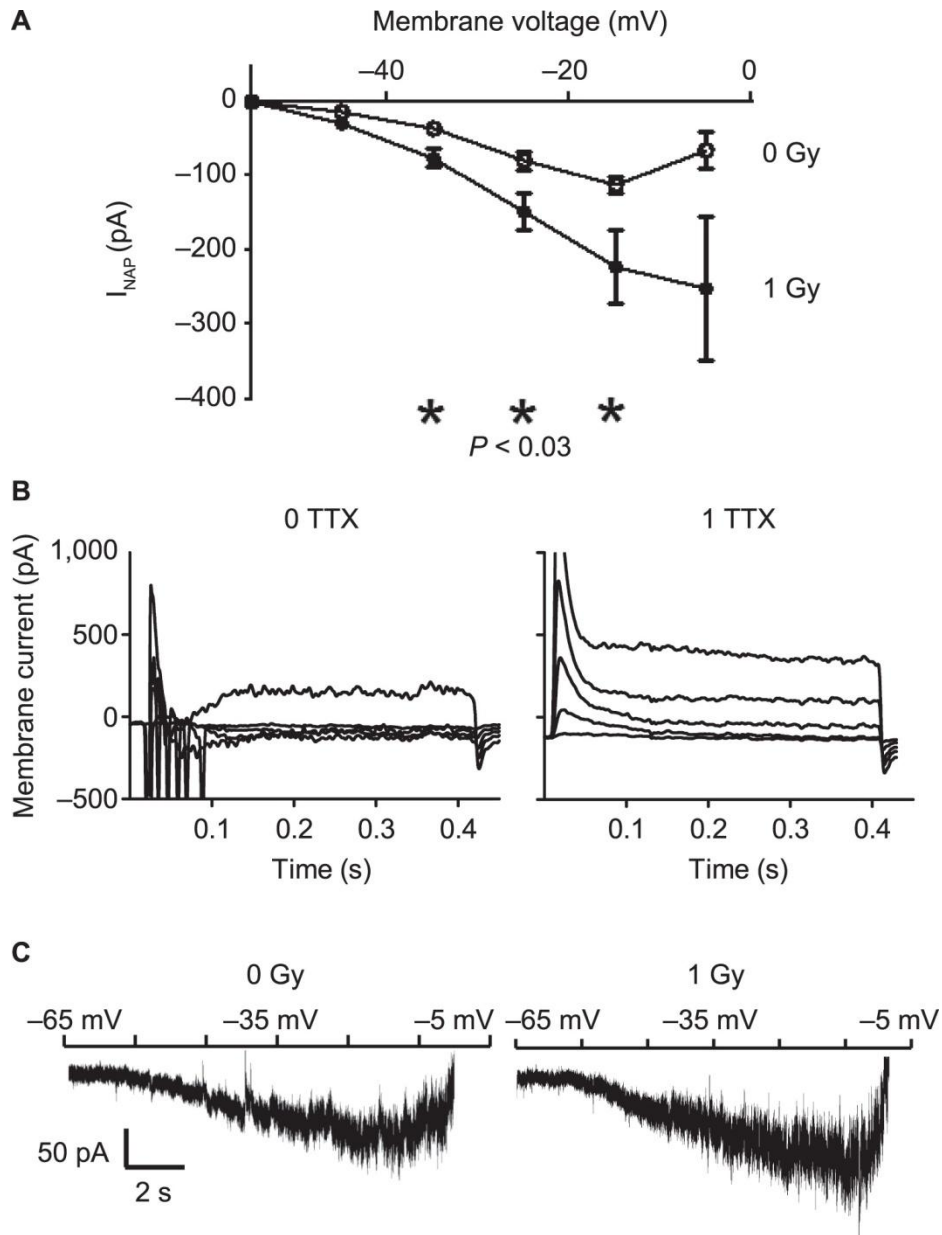
Figure 3.5. Panel A: Radiation exposure significantly augmented the I_{NaP}. I_{NaP} was identified as a TTX-sensitive non-inactivating steady state whole-cell current. Panel B: Leak-subtracted whole-cell currents in response to stimulating potentials from −45 mV to −5 mV in nonirradiated animals. In the absence of TTX (0 TTX), stimulation of neurons to suprathreshold potentials was not associated with the increase of the whole-cell currents as expected from activation of K_{DR} (left side). This is explained by the partial masking of the K^+ currents by the negatively polarized voltage-gated steady-state TTX-sensitive currents. K_{DR} was unmasked in the 1 μ*M* TTX-containing ACSF (1 TTX, right side). Panel C: Representative TTX-sensitive currents recorded using the voltage ramp protocol. Neurons were initially clamped at −65 mV and then were steadily depolarized by 60 mV within a time period of 14 s. Slow depolarization eliminated contribution of the fast I_{Na}. Larger I_{NaP} in irradiated neurons (right side) is associated with the higher current noise.

Network simulations

After proton irradiation, the CA1 pyramidal cell population underwent a small but significant change in its passive membrane properties, but the impact of this change on overall network activity is uncertain. To investigate the functional implications of these radiation-induced alterations, we utilized a recent computational model of the CA1 microcircuit, which contains pyramidal cells and four types of inhibitory interneurons (Cutsuridis et al., 2010). Network simulations were performed for two separate conditions: with the control pyramidal cell model and with a pyramidal cell model incorporating the radiation-induced alterations in passive membrane properties (resting membrane potential hyperpolarized by 6% compared to the control and input resistance decreased to 86% of control). Each of the two networks was then tested for its ability to produce theta oscillations during the pattern recall function of the microcircuit. The control condition exhibited pyramidal cell firing that exhibited strong theta oscillations (Figure 3.6A), and pyramidal cell activity was dramatically reduced after incorporating the changes in passive membrane properties (Figure 3.6B). Example traces exemplifying the diminished excitability of pyramidal cells in the control and irradiated conditions are shown (Figure 3.6C). The power of the theta oscillation in pyramidal cell firing was reduced to 50.6% in the irradiated condition relative to the control network (Figure 3.6D), while the peak theta oscillation frequency remained constant at 4.0 Hz. The computational modeling results show that the small radiation-induced alterations in the passive membrane properties of pyramidal cells can dramatically compromise the function of the CA1 network.
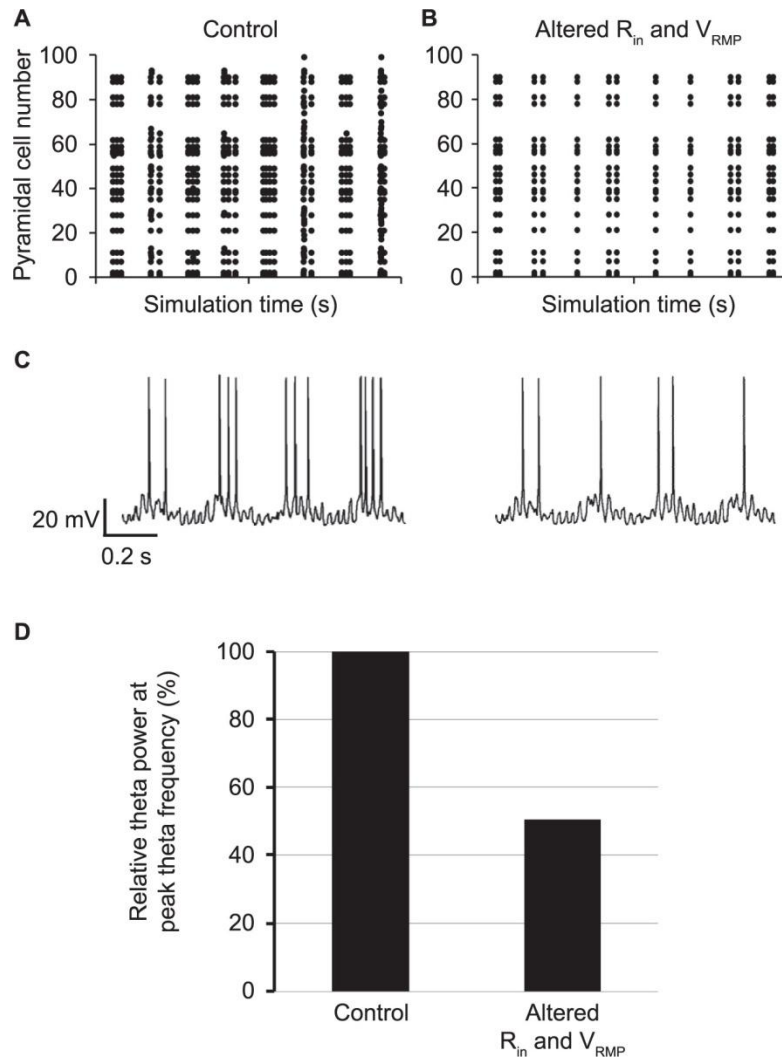
Figure 3.6. Incorporation of radiation-induced alterations into a computational model of the CA1 microcircuit containing 100 excitatory cells and four types of interneurons using the NEURON simulation environment. Panel A: Pyramidal cell firing statistics for the control condition after initial stimulation of 20% of the cells. Each dot represents a single action potential. Panel B: Pyramidal cell firing statistics after incorporation of radiation-induced changes in resting membrane potential and input resistance. Panel C: Voltage traces for pyramidal cell no. 1 under control (left side) and irradiated (right side) simulation conditions. Panel D: Relative theta oscillation power at the 4.0 Hz peak theta frequency.

Discussion

Using the patch-clamp technique, we examined the effect of proton radiation at a dose of

1 Gy on the electrophysiological properties of CA1 pyramidal neurons in the mouse

hippocampus. Proton radiation mimics space radiation since energetic protons constitute up to

85% of the cosmic ray particle fluence. The 1 Gy dose of radiation used in this study is similar to that expected for astronauts during prolonged space flights or large solar particle events (Curtis, 1963;Curtis et al., 1998;Hassler et al., 2013;Zeitlin et al., 2013). We found that radiation affected the passive membrane properties of CA1 pyramidal neurons in a way that reduced neuronal excitability. This effect of radiation was counterbalanced by the radiation-induced increase of the I_{NaP} and the rate of mEPSCs which are known to facilitate neuronal excitation. To the best of our knowledge, the data presented here is the first to demonstrate the effect of low dose ionizing radiation on the electrophysiology of CA1 pyramidal neurons in the hippocampus.

Radiation damage has long been associated with oxidative stress due to its production of reactive oxygen and nitrogen species. Radiation-induced production of the reactive oxygen species (ROS) in the CNS has been well documented (Limoli et al., 1998;Limoli et al., 2007;Rola et al., 2007;Suman et al., 2013). ROS oxidize a variety of transmembrane proteins including ion channels (Garcia-Sancho and Herreros, 1983;Anzai et al., 2000;Matalon et al., 2003;Zima and Blatter, 2006;Bogeski et al., 2011) and neurotransmitter receptors (Sucher and Lipton, 1991;Lei et al., 1992;Tang and Aizenman, 1993a;b;Sullivan et al., 1994;Lipton et al., 1998;Choi and Lipton, 2000;Kamsler and Segal, 2003). ROS could also indirectly affect ion channels and transporters through oxidation of the membrane lipids or modulation of their associated protein kinases (Stark, 2005;Wagner et al., 2013).

Since oxidative stress affects numerous cellular structures, we aimed at evaluating a wide range of electrophysiological parameters of CA1 pyramidal neurons to identify the ion currents affected by radiation. Contrasting the apparent effects on animal behavior by low doses of accelerated [56]Fe (Shukitt-Hale et al., 2003;Britten et al., 2014), proton radiation at doses of up to 4 Gy had no effect on rat performance in two common behavioral tests (Shukitt-Hale et al.,

2004), suggesting that the proton radiation effect on the hippocampus is either small and/or that animal behavioral tests are not sensitive enough to reveal the effect of low dose proton radiation on memory and cognition. Alternatively, radiation is associated with a series of alterations in the neural networks that, at least in part, compensate for each other's effects. Compensatory mechanisms induced in response to a disturbance in the environment, referred to as homeostatic plasticity, have been well documented in neural networks (Desai et al., 1999;Echegoyen et al., 2007;Mrsic-Flogel et al., 2007;Turrigiano, 2008). We hypothesized that radiation-induced oxidation alters the normal, "target" rate of neuronal activity. This primary effect of radiation then triggers homeostatic plasticity which, at least in part, compensates for the initial perturbation of the neuronal basal states. We used the patch-clamp technique to identify the electrophysiological characteristics of CA1 pyramidal neurons affected by radiation.

Radiation-induced changes of the passive membrane properties reported here, such as hyperpolarization of the RMP and reduction of the R_{in}, suppress neuronal excitability. Indeed, since R_{in} is a measure of neuronal membrane resistance, a decrement in R_{in} signifies an increase of the membrane conductance, a change that normally dampens the depolarizing effect of the excitatory inputs. In addition, the V_{RMP} shifted towards more negative potentials (away from the V_{Na}, the voltage for spike initiation). As a result of the altered R_{in} and V_{RMP}, stronger excitatory input would be required to bring irradiated neurons to the target rate of spiking activity. The role of the passive membrane properties in neuronal excitability have been emphasized in other studies. For example, modulation of V_{RMP} underlies, at least in part, the effects of a number of anesthetics (Wann and Southan, 1992). On the other hand, increased R_{in} contributes to hyperexcitability of the *locus ceruleus* neurons in a mouse model of Rett syndrome (Taneja et

al., 2009). In addition to its role in neuronal excitability, changed intrinsic membrane properties have a defining role in long-term potentiation (LTP).

LTP refers to a phenomenon of strengthening synaptic communication between neurons following a short period of intense neuronal spiking activity. In the hippocampus, LTP is considered a cellular model for memory storage critical for cognitive performance. Altered excitability of irradiated neurons might affect LTP through its impact on the oscillatory behavior of neuronal networks which takes place during the information processing in the hippocampus and is associated with certain behavioral activities. For example, during exploration, running and REM sleep, CA1 neurons display rhythmic and synchronized spiking at frequencies referred to as the theta frequency (3-10 Hz). Oscillations in theta frequency range are driven by the excitatory inputs from the CA3 pyramidal neurons, and are modulated by hippocampal interneurons and by inputs from other brain areas (Buzsaki, 2002). Theta rhythm oscillations in hippocampal neural networks facilitate LTP, and are critical for temporal coding/decoding of active neuronal ensembles as well as the modification of synaptic weights in various types of plasticity (Buzsaki, 2002).

We used computational modeling to evaluate the effect of excitability changes on neuronal network activity. The hippocampal microcircuit model contained the major types of neurons involved in the formation of the hippocampal theta rhythm oscillations. We modified the R_{in} and the V_{RMP} in the pyramidal cell model in the same manner as produced by radiation. This modification of the pyramidal cell model resulted in a marked change of oscillatory network activity expressed as a dramatic reduction in the power of the theta oscillation in pyramidal neurons (Figure 3.6). Such a change in the neuronal network function might potentially contribute to hippocampus-dependent behavioral and cognitive deficits, and critically affect

astronauts' performance during space missions. In experimental rats and in humans, impairment of oscillatory activity of the hippocampal networks is linked to stress- and age-related deficits in learning and memory (Jacinto et al., 2013;van de Vijver et al., 2014).

It remains to be established whether alterations in the hippocampal neural networks are present in irradiated mice *in vivo*. Alternatively, decreased neuronal excitability contributed by the altered V_{RMP} and R_{in} could be compensated by adjustments of other intrinsic or synaptic properties of the hippocampal neurons. One such adjustment could potentially be the increased rate of mEPSCs in irradiated CA1 pyramidal neurons. The augmented rate of mEPSCs results either from an increased probability of synaptic release at the CA3-CA1 synapse (a change involving presynaptic CA3 pyramidal neurons) or from the elevated density of functional excitatory synapses in CA1 pyramidal neurons. Either change increases the total amount of glutamate released during synaptic transmission at excitatory synapses, thus contributing to neuronal depolarization and excitation.

Another change produced by radiation which facilitates neuronal excitability is the upregulated I_{NaP}. I_{NaP} is a non-inactivating, or slowly inactivating, TTX-sensitive current of negative polarity specific to Na^+ ions (Crill, 1996;Magistretti and Alonso, 1999). I_{NaP} has been demonstrated in CA1 pyramidal neurons, as well as in neurons from other brain areas (French et al., 1990;Caffrey et al., 1992). By facilitating neuronal depolarization, I_{NaP} has a role in integrating synaptic potentials, accelerating firing rates and promoting subthreshold oscillations (Crill, 1996;Kay et al., 1998), thus contributing to neuronal excitability. The elevated I_{NaP} may account for the unchanged minimal suprathreshold currents (Figure 3.3C) and, together with the modified mEPSCs, compensate for the effects of reduced neuronal excitability in the irradiated neurons.

The fact that radiation-induced alterations produce antagonistic effects on neuronal excitability suggests a possible involvement of homeostatic plasticity. Homeostatic plasticity refers to the capacity of the central and peripheral neurons to adapt to chronic perturbations in the environment by adjusting their biophysical traits to maintain their firing within a target range. Homeostatic plasticity includes a large number of phenomena identified in a wide range of organisms and brain regions (Davis and Bezprozvanny, 2001;Marder and Prinz, 2003;Turrigiano and Nelson, 2004;Turrigiano, 2007). Homeostatic modulation of ionic currents has been well documented. For example, activity blockade in cortical cultured neurons upregulated the fast Na^+ current and down-regulated the K^+ current, two changes that increase neuronal excitability (Desai et al., 1999;Howard et al., 2007). Modulation of other types of ionic currents in response to changed network activity has also been reported (Fan et al., 2005;Howard et al., 2007;Breton and Stuart, 2009;Cudmore et al., 2010).

We speculate that some alterations in irradiated neurons were contributed by mechanisms of homeostatic plasticity. Activation of these mechanisms was secondary to the alterations in the neural networks produced by direct effects of radiation on neuronal structures. It is unclear which alterations reported here result directly from radiation-induced oxidative damage and which are induced as part of homeostatic plasticity. Previous studies suggest the I_{NaP} serves as a likely target of cellular oxidative processes. For example, NO, a free radical and an oxidizing agent that is produced during radiation and is elevated during inflammation, acutely increased the I_{NaP} in rat hippocampal neurons (Hammarstrom and Gage, 1999). Elevated I_{NaP} has been reported to be associated with enhanced levels of ROS and oxidative stress. It accompanies oxidative stress in motor neurons undergoing pathologic changes during myotrophic lateral sclerosis, a complex motor neuron disorder (Bae et al., 2013). The I_{NaP} is also enhanced in one of

76

the mouse models of myotrophic lateral sclerosis expressing mutated Cu^{2+},Zn^{2+} superoxide dismutase (Pieri et al., 2009).

The data presented in the current study does not yet reveal the specific molecular mechanisms underlying the alterations in neuronal intrinsic or synaptic properties. The V_{RMP} is determined by relative contributions of K^+, Na^+, and Cl^- membrane conductances to the total membrane current, and by the Na^+/K^+ ATPase (Ross and Soltesz, 2000;Nicholls, 2012). An increase in the K^+ conductance or a decrement in the Na^+ or Cl^- conductances might lead to both the membrane hyperpolarization and decrements of the R_{in} (Fatt and Katz, 1951). The enhanced I_{NaP} could be contributed by elevated expression of the Na^+ channels or by a change in the Na^+ channel function, such as an increased unitary conductance or changes to the channel kinetics. Further studies are necessary to establish the molecular mechanisms contributing to the chronic effects of radiation on neuronal electrophysiology.

In conclusion, the data presented here provide the first evidence that proton radiation at a dose relevant to prolonged deep space missions produces long-term changes to neuronal electrophysiological states. The mutually opposing effects of the radiation-induced alterations on neuronal excitability might contribute to amelioration of the functional outcome of the radiation-induced changes explaining the relative insensitivity of the common behavioral tests in detecting the effects of the low dose radiation.

Figure S3.1. V_{RMP} plotted against the time of V_{RMP} recording after the start of the experiment (the moment the whole-cell configuration of the patch-clamp experiment was obtained by membrane rupture). Symbols with the standard error bars are means of the V_{RMP} and the time in the control (open circle) and the irradiated groups (closed circle).

CHAPTER 4

Resolution Revolution: Epilepsy Dynamics at the Microscale

Abstract

Our understanding of the neuronal mechanisms behind epilepsy dynamics has recently advanced due to the application of novel technologies, monitoring hundreds of neurons with single cell resolution. These developments have provided new theories on the relationship between physiological and pathological states, as well as common motifs for the propagation of paroxysmal activity. While traditional electroencephalogram (EEG) recordings continue to describe normal network oscillations and abnormal epileptic events within and outside of the seizure focus, analysis of epilepsy dynamics at the microscale has found variability in the composition of macroscopically repetitive epileptiform events. These novel results point to heterogeneity in the underlying dynamics of the disorder, highlighting both the need and potential for more specific and targeted therapies.

Introduction

Epilepsy involves the spontaneous generation, propagation, and termination of pathological network events, typically surrounded spatially and temporally by predominantly normal neural activity. The challenge in selectively treating the condition is determining what mechanisms cause this shift from the physiological to pathological state and what measures can be used to predict the time and location of seizures. The development of advanced multi-modal imaging and multi-electrode array technologies has dramatically increased the temporal and spatial resolution of recordings, leading to several novel insights into the underpinnings of the disorder. The spiral wave dynamic, in which propagating waves emanate from and rotate around

a central rhythmic organizer (Winfree, 2001), has been detected in the normal cortex in vivo using voltage-sensitive dye imaging (Huang et al., 2010), providing a powerful mechanism by which to entrain neuronal populations, while multi-electrode arrays have revealed that seizures may also exhibit spiral wave behavior (Viventi et al., 2011). Normal, interictal, and ictal (seizures) brain states are thought to coexist in the epileptic brain, but the transformation that allows a physiological mechanism such as the spiral waves to instead propagate recurrent pathological activity is unknown. From a dynamical systems theory perspective, a bifurcation barrier (separatrix) is thought to act between the normal and pathological brain states, and the onset of a seizure begins when the normal brain trajectory collides with this barrier (Jirsa et al., 2014). In addition to this theoretical barrier between brain states, a sharp demarcation can be present between the areas of the brain that become entrained and recruited into a seizure and other adjacent non-participating areas ("penumbra") (Schevon et al., 2012;Weiss et al., 2013), demonstrating a seizure core surrounded by an inhibitory restraint. Based on functional connectivity from multisite recordings in patients, seizures have been characterized as a consistent progression of brain states, in which the seizure onset zone is isolated at the seizure onset but gradually becomes more connected until seizure termination (Burns et al., 2014). Discovering the dynamics particular to the seizure focus thus becomes paramount to the localization and targeted treatment of the seizure disorder, and the levels of both physiological and pathological oscillations have recently been shown to be crucial for clinical intervention.

Spikes and Oscillations at the Seizure Focus

After frontline anti-epileptic drugs fail to satisfactorily control seizures in patients, the clinical effectiveness of subsequent treatment is heavily influenced by the ability to localize the

seizure-generating brain structures, as the removal of tissue associated with frequent seizure onset, not the surrounding infrequent onset areas, during surgical intervention predicts freedom from seizures (Huang et al., 2012). As a result, the ability to localize the onset zone from current clinical measurements, such as EEG recordings, has obtained ever-increasing scrutiny. Interictal spikes (IISs) are generated by synchronized discharges of cell populations and precede the appearance of spontaneous seizures during epileptogenesis in experimental epilepsy models (reviewed in (Staley and Dudek, 2006); also (White et al., 2010;Chauvière et al., 2012)). The incidence of IISs is currently used as a diagnostic tool due to their high correlation with spontaneous seizures (Engel, 2013). In contrast, gamma oscillations (defined as 30-100 Hz) have a more variable correlation with the seizure onset zone. While electrodes in the seizure onset zone have been shown to have higher mean gamma oscillation activity in some patients (Gupta et al., 2011), secondary seizure areas or areas without seizures can have more frequent gamma oscillations than the seizure onset zone (Smart et al., 2012). However, cross-frequency coupling between the high gamma oscillation (defined as 80-150 Hz) amplitude and the low frequency (1-25 Hz) ictal rhythm allows the core seizure territory to be distinguished from the penumbra (Weiss et al., 2013). In addition to these dynamics, physiological and pathological higher frequency oscillations have also been used to localize the seizure focus.

High frequency oscillations (HFOs) in the normal ripple (defined as 80-250 Hz) and pathological fast ripple (FR; 250-500 Hz) spectral domains have recently provided valuable additions to the clinical perspective, although the overwhelming variability in the epileptic condition often obfuscates universal changes. HFOs and IISs have been shown to occur both simultaneously as well as independently (Jacobs et al., 2008), but FRs have a particular potential in epilepsy diagnostics, as the FR frequency range typically reflects pathological activity in

81

hippocampal and parahippocampal structures (Bragin et al., 1999;Bragin et al., 2002;Staba et al., 2002;Staba et al., 2004;Engel Jr et al., 2009). In patients with lesions, the presence of HFOs was found to be more tightly coupled to the seizure onset zone than to the location of the lesion, which does not necessarily coincide with the area where the seizure emerges (Jacobs et al., 2009). This tight coupling of HFOs to the epilepsy onset zone proves to have a critical importance in surgical interventions, because the resecting of regions with HFO activity correlated with a better seizure outcome after the surgery, with FRs serving as a more specific marker than ripples (Jacobs et al., 2008;Akiyama et al., 2011). However, in neocortical epilepsy, ripple oscillations were found to be increased in the seizure onset zone more frequently than fast ripple oscillations (Blanco et al., 2011). In addition, a high degree of variability has been shown between patients with regard to the relative levels of ripples, fast ripples, and mixed events before, during, and after seizures (Pearce et al., 2013), indicating the possible need for individualized seizure detection and treatment. While the oscillations present during interictal and ictal activity provide invaluable information for targeted surgical resection, determining the participating cells and networks in these pathological dynamics may lead to more mechanistic explanations for the transition to the epileptic state, which requires moving beyond broad EEG recordings. This avenue of study has been enabled by the development and application of methods aimed at the simultaneous recording of hundreds of neurons.

Synchrony During Interictal Events and Seizures

Traditional EEG methods are not suitable to determine the participation of individual cells in the creation and propagation of pathological dynamics, which has led to the recent application of techniques that are able to monitor multiple cells simultaneously. For example,

multibeam two-photon calcium imaging in hippocampal slices from chronically epileptic animals exhibiting spontaneous seizures revealed that epileptic networks are composed of multiple functional clusters of spatially localized neurons. Unexpectedly, these clusters co-activated in unpredictable combinations to give rise to interictal-like network events (Feldt Muldoon et al., 2013) (Figure 4.1A). Although active neuronal clusters have been observed in both normal and epileptic hippocampal circuits, the epileptic tissue contains more functional clusters, and these clusters are more spatially localized (Feldt Muldoon et al., 2013). Similar heterogeneity has also been observed during interictal epileptiform activity in humans with intractable focal epilepsy (Keller et al., 2010). This suggests that interictal network events do not simply represent a hypersynchronous entrainment of cells, but rather reflect a phenomenon that involves the interplay between spatially dispersed cell assemblies. A startling conclusion of these studies has been that, in fact, differing combinations of active neuronal clusters give rise to pathological interictal events that only appear self-repeating or recurrent when viewed at a macroscopic scale (e.g., using EEG or local field potential recordings).
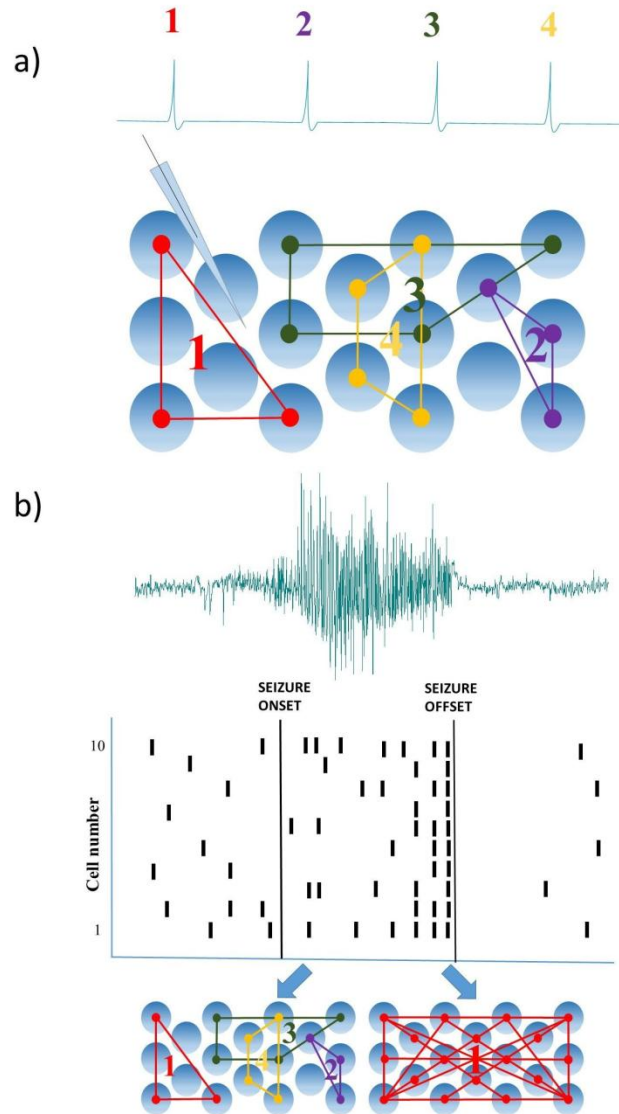
Figure 4.1. Epileptiform activity has recently been shown to reflect heterogeneity rather than homogeneous synchrony when viewed at the microscale. (**A**) Interictal-like network events emerge due to the co-activation of functional clusters of spatially localized neurons in unpredictable combinations (Feldt Muldoon et al., 2013). The consecutive activation of different cell clusters brings about a seemingly recurrent pattern when observed on a local field potential recording. (**B**) Spontaneous seizures show heterogeneous activity patterns when viewed at the microscale. *Top:* Example seizure. *Middle*: Raster plot of cellular activity based on the findings of Truccolo and colleagues (Truccolo et al., 2011). At seizure onset, cells fire heterogeneously. At seizure termination, cellular activity becomes homogeneous, and the neurons enter a refractory state. *Bottom:* Possible arrangement of active cell clusters at the onset and offset of the seizure. At onset, randomly activated cell clusters might give rise to seizure cycles, similar to interictal-like events. At offset, cells homogeneously fire and may act as one cluster.

Ictal events were similarly found to have a rather heterogenous pattern of activity, instead of homogenous synchrony, when studied at the microscale, enabled by the application of multi-electrode single-unit recordings (Truccolo et al., 2011;Bower et al., 2012;Cymerblit-Sabba and Schiller, 2012;Truccolo et al., 2014). In addition, the level of synchrony changed during the seizure, with a relatively asynchronous state in the seizure onset followed by a more synchronous state towards the termination phase (Truccolo et al., 2011) (Figure 4.1B). These findings exemplify growing evidence for asynchrony before and during seizure generation followed by hypersynchrony facilitating seizure termination (reviewed in (Jiruska et al., 2013)). Accordingly, it has been suggested that a higher level of population activity can be maintained in a neuronal network if the cells are firing asynchronously (Golomb, 1998;Gutkin et al., 2001;Netoff and Schiff, 2002). Excessive synchronous firing may lead to communal refractoriness, in which the seizure terminates because the number of available excitable cells abruptly drops, though seizures can also terminate through depolarization block of principal cells (Bragin et al., 1997). Another explanation can be that during seizures, localized clusters of active cells are co-activated in an unpredictable order, similar to the observations for interictal events (Feldt Muldoon et al., 2013). Indeed, the heterogeneity of cell spiking was much higher during seizures even if quite similar motifs of neuronal firing patterns were observed in consecutive focal seizures (Truccolo et al., 2011). Taken together, these findings suggest that epileptic seizures and interictal events are much more complicated network phenomena than previously thought.

Cell Type-Specific Microcircuit Interactions

Instead of simple runaway excitation, seizures reflect rather precise interactions between neuronal subgroups. The composition of these subgroups remains an open question, as previous

studies have not addressed the various distinctions that exist between and within neuronal classes (e.g. (Soltesz, 2005;Bezaire and Soltesz, 2013)). Seemingly homogenous populations have been increasingly shown to instead be composed of heterogeneous subpopulations, forming functional dichotomies during network events. For example, in the case of the CA1 pyramidal cell population in the normal hippocampus, recent research has revealed that deep and superficial pyramidal cells form functionally distinct sublayers with regard to their participation in theta oscillations and in other aspects (Mizuseki et al., 2011). Consistent with this dichotomy, deep CA1 pyramidal neurons receive stronger inhibition from fast-spiking basket cells (a key interneuronal subtype implicated in a variety of normal and abnormal oscillatory phenomena (Hu et al., 2014)) than superficial pyramidal cells (Lee et al., 2014). Subsequently, the participation of these basket cells in ripple oscillations has been shown to further segregate along specific anatomical features (Varga et al., 2014). As predicted by theoretical studies (Morgan and Soltesz, 2008), exceedingly rare but unusually well-connected hub-like cells may play crucial roles in epilepsy, and certain early born neurons during prenatal development have indeed been demonstrated to be able to serve as functional hub cells by exerting powerful effects on synchronous network events (Bonifazi et al., 2009;Picardo et al., 2011). As a result, unmasking these primary generating and participating subpopulations in the epileptic condition has become an important goal for future research.

Concluding Remarks

While the recent shifts in focus to the microscale mechanisms enabled by high-resolution electrophysiological and optical imaging technologies have revealed unexpected levels of complexity, such new insights into microcircuit organization under healthy and

pathophysiological conditions could also lead to a higher degree of specificity in targeting epilepsy, as well as to more individualized treatment. In particular, optogenetic techniques have provided significant recent progress toward higher specificity in controlling spontaneous seizures in models of experimental epilepsy, because they allow for targeting neurons in a time-, location-, direction of modulation- (i.e. inhibition/excitation), and cell type-specific manner (reviewed in (Krook-Magnuson et al., 2014a)). The increased specificity of intervention offered by optogenetic approaches also highlighted the potential for efficient control of seizure activity from brain structures that are located outside of the area where the seizure focus resides (Krook-Magnuson et al., 2013;Paz et al., 2013;Krook-Magnuson et al., 2014b). As the microscale dynamics and mechanisms for each type of epilepsy and within each patient become increasingly elucidated due to these higher resolution technologies, treatment options of the future have the potential to become more and more focused as well, reducing the side effects associated with the currently available 'macroscale'-targeting interventions.

Acknowledgments

CHAPTER 5

Future Directions

The work presented here lays a foundation for future model development and a closer tie between computational modeling and the biological condition. The generated variable morphologies should be converted into variable electrophysiological models through the insertion of biophysical mechanisms and channel conductances. Recent experimental studies have provided information on the dendritic attenuation (Schmidt-Hieber et al., 2007;Krueppel et al., 2011) and action potential initiation (Schmidt-Hieber and Bischofberger, 2010) in granule cells that the new models should match, and a recent experimental and modeling study on several inherent channel conductances should provide a starting point for this endeavor (Mateos-Aparicio et al., 2014) There may be some compensation required, however, to account for the morphological variability in order to create models that still fire according to the properties of the granule cell class (Hay et al., 2013).

The other dentate gyrus cell types should be placed in the new structure and connected, taking advantage of the three-dimensional structure to attain an unparalleled approximation of the biological dentate gyrus. The mossy cells and interneuronal cell types from previous iterations of the model can be inserted, and with the realistic three-dimensional structure, the known septotemporal distributions of these neurons (Buckmaster and Dudek, 1997;Buckmaster and Jongen-Relo, 1999;Jinno et al., 1999) can be taken into account in their placement. Hilar cells that project to the commissural-associational pathway (HICAP) (Han et al., 1993;Freund and Buzsáki, 1996) and neurogliaform cells (Armstrong et al., 2011) will require the construction of new models to form a more complete network. The connectivity will need to be updated from the previous model detailed in **Chapter 1**, taking into account recent electrophysiological studies

(Savanthrapadian et al., 2014) as well as including gap junctions between particular

interneuronal classes (Bartos et al., 2001;Meyer et al., 2002;Baude et al., 2007;Armstrong et al.,

2011;Iball and Ali, 2011). This would result in the first data-driven, full-scale, and three-

dimensional function model with this level of size and complexity for any brain region.

While certain pathologies in the irradiated or epileptic brain can now be incorporated,

there are still several additions to the model that would greatly increase our understanding of the

pathological circuit. The recently observed changes in granule cell dendritic architecture after

irradiation (Parihar and Limoli, 2013) can now be directly incorporated, as the experimentally

measured parameters (branch points, dendritic length, etc.) are direct inputs or easily tunable

outputs for the morphology generation process discussed in **Chapter 2**. In contrast, newborn

granule cells have not been generated or modeled. The reduction of neurogenesis in the dentate

gyrus by radiation has been well-established (Cucinotta et al., 2014) , but the relative importance

of neurogenesis decrements, dendritic architecture changes, and charged particle tracks

traversing the tissue (Cucinotta and Durante, 2006) in producing cognitive deficits is unknown

and could be teased apart through computational modeling. In addition, these newborn cells have

been increasingly implicated in temporal lobe epilepsy, acting as a primary source of mossy fiber

sprouting and hilar ectopic granule cells (Kron et al., 2010;Parent and Kron, 2012;Hester and

Danzer, 2013).

One exciting future avenue enabled by this work is the reduction of the full-scale model

to a "virtual slice" model. Very few electrophysiological studies have been done on the full intact

dentate gyrus, but there is a wealth of literature available for brain slice electrophysiology. With

our model cells distributed in a realistic three-dimensional structure, the model can then be cut to

only include those neurons, connections, and dendrites that are located inside of a particular

slice. This would keep the advantages of full-scale modeling (such as the direct incorporation of experimental observations and measurements) but allow for a more direct comparison and validation from experimental approaches as well as demand less computational resources. This represents an entirely new modeling paradigm, with myriad applications and validation tests that would serve to dramatically reduce the gap between computational and experimental neuroscience.

REFERENCES

Abayomi, O.K. (1996). Pathogenesis of irradiation-induced cognitive dysfunction. *Acta Oncol* 35**,** 659-663.

Acker, C.D., and White, J.A. (2007). Roles of IA and morphology in action potential propagation in CA1 pyramidal cell dendrites. *J Comput Neurosci* 23**,** 201-216.

Akers, K.G., Martinez-Canabal, A., Restivo, L., Yiu, A.P., De Cristofaro, A., Hsiang, H.L., Wheeler, A.L., Guskjolen, A., Niibori, Y., Shoji, H., Ohira, K., Richards, B.A., Miyakawa, T., Josselyn, S.A., and Frankland, P.W. (2014). Hippocampal neurogenesis regulates forgetting during adulthood and infancy. *Science* 344**,** 598-602.

Akiyama, T., Mccoy, B., Go, C.Y., Ochi, A., Elliott, I.M., Akiyama, M., Donner, E.J., Weiss, S.K., Snead, O.C., and Rutka, J.T. (2011). Focal resection of fast ripples on extraoperative intracranial EEG improves seizure outcome in pediatric epilepsy. *Epilepsia* 52**,** 1802-1811.

Alldred, M.J., Duff, K.E., and Ginsberg, S.D. (2012). Microarray analysis of CA1 pyramidal neurons in a mouse model of tauopathy reveals progressive synaptic dysfunction. *Neurobiol Dis* 45**,** 751-762.

Alme, C.B., Buzzetti, R.A., Marrone, D.F., Leutgeb, J.K., Chawla, M.K., Schaner, M.J., Bohanick, J.D., Khoboko, T., Leutgeb, S., Moser, E.I., Moser, M.B., Mcnaughton, B.L., and Barnes, C.A. (2010). Hippocampal granule cells opt for early retirement. *Hippocampus* 20**,** 1109-1123.

Ames, B.N., Shigenaga, M.K., and Hagen, T.M. (1993). Oxidants, antioxidants, and the degenerative diseases of aging. *Proc Natl Acad Sci U S A* 90**,** 7915-7922.

Anzai, K., Ogawa, K., Ozawa, T., and Yamamoto, H. (2000). Oxidative modification of ion channel activity of ryanodine receptor. *Antioxid Redox Signal* 2**,** 35-40.

Aradi, I., and Holmes, W.R. (1999). Role of multiple calcium and calcium-dependent conductances in regulation of hippocampal dentate granule cell excitability. *J Comput Neurosci* 6**,** 215-235.

Armstrong, C., Szabadics, J., Tamas, G., and Soltesz, I. (2011). Neurogliaform cells in the molecular layer of the dentate gyrus as feed-forward gamma-aminobutyric acidergic modulators of entorhinal-hippocampal interplay. *J Comp Neurol* 519**,** 1476-1491.

Ascoli, G.A., Donohue, D.E., and Halavi, M. (2007). NeuroMorpho.Org: a central resource for neuronal morphologies. *J Neurosci* 27**,** 9247-9251.

Ascoli, G.A., and Krichmar, J.L. (2000). L-Neuron: a modeling tool for the efficient generation and parsimonious description of dendritic morphology. *Neurocomputing* 32**,** 1003-1011.

Ascoli, G.A., Krichmar, J.L., Scorcioni, R., Nasuto, S.J., and Senft, S.L. (2001). Computer generation and quantitative morphometric analysis of virtual neurons. *Anat Embryol (Berl)* 204**,** 283-301.

Badhwar, G.D., and Cucinotta, F.A. (1998). Depth dependence of absorbed dose, dose equivalent and linear energy transfer spectra of galactic and trapped particles in polyethylene and comparison with calculations of models. *Radiat Res* 149**,** 209-218.

Bae, J.S., Simon, N.G., Menon, P., Vucic, S., and Kiernan, M.C. (2013). The puzzling case of hyperexcitability in amyotrophic lateral sclerosis. *J Clin Neurol* 9**,** 65-74.

Bar-Yehuda, D., and Korngreen, A. (2008). Space-clamp problems when voltage clamping neurons expressing voltage-gated conductances. *J Neurophysiol* 99**,** 1127-1136.

Barnes, C.A., Mcnaughton, B.L., Mizumori, S.J., Leonard, B.W., and Lin, L.H. (1990). Comparison of spatial and temporal characteristics of neuronal activity in sequential stages of hippocampal processing. *Prog Brain Res* 83**,** 287-300.

Bartos, M., Vida, I., Frotscher, M., Geiger, J.R., and Jonas, P. (2001). Rapid signaling at inhibitory synapses in a dentate gyrus interneuron network. *The Journal of Neuroscience* 21**,** 2687-2698.

Baude, A., Bleasdale, C., Dalezios, Y., Somogyi, P., and Klausberger, T. (2007). Immunoreactivity for the GABAA receptor α1 subunit, somatostatin and connexin36 distinguishes axoaxonic, basket, and bistratified interneurons of the rat hippocampus. *Cerebral Cortex* 17**,** 2094-2107.

Bezaire, M.J., and Soltesz, I. (2013). Quantitative assessment of CA1 local circuits: Knowledge base for interneuron-pyramidal cell connectivity. *Hippocampus* 23**,** 751-785.

Blanco, J.A., Stead, M., Krieger, A., Stacey, W., Maus, D., Marsh, E., Viventi, J., Lee, K.H., Marsh, R., and Litt, B. (2011). Data mining neocortical high-frequency oscillations in epilepsy and controls. *Brain* 134**,** 2948-2959.

Blumcke, I., Suter, B., Behle, K., Kuhn, R., Schramm, J., Elger, C.E., and Wiestler, O.D. (2000). Loss of hilar mossy cells in Ammon's horn sclerosis. *Epilepsia* 41 Suppl 6**,** S174-180.

Bogeski, I., Kappl, R., Kummerow, C., Gulaboski, R., Hoth, M., and Niemeyer, B.A. (2011). Redox regulation of calcium ion channels: chemical and physiological aspects. *Cell Calcium* 50**,** 407-423.

Bonifazi, P., Goldin, M., Picardo, M.A., Jorquera, I., Cattani, A., Bianconi, G., Represa, A., Ben-Ari, Y., and Cossart, R. (2009). GABAergic hub neurons orchestrate synchrony in developing hippocampal networks. *Science* 326**,** 1419-1424.

Bower, M.R., Stead, M., Meyer, F.B., Marsh, W.R., and Worrell, G.A. (2012). Spatiotemporal neuronal correlates of seizure generation in focal epilepsy. *Epilepsia* 53**,** 807-816.

Bragin, A., Engel, J., Wilson, C.L., Fried, I., and Buzsáki, G. (1999). High-frequency oscillations in human brain. *Hippocampus* 9**,** 137-142.

Bragin, A., Mody, I., Wilson, C.L., and Engel, J. (2002). Local generation of fast ripples in epileptic brain. *The Journal of neuroscience* 22**,** 2012-2021.

Bragin, A., Penttonen, M., and Buzsáki, G. (1997). Termination of epileptic afterdischarge in the hippocampus. *The Journal of neuroscience* 17**,** 2567-2579.

Braitenberg, V., and Schüz, A. (1991). *Anatomy of the cortex: Statistics and geometry.* Springer-Verlag Publishing.

Bremner, J.D., Krystal, J.H., Southwick, S.M., and Charney, D.S. (1995). Functional neuroanatomical correlates of the effects of stress on memory. *J Trauma Stress* 8**,** 527-553.

Breton, J.D., and Stuart, G.J. (2009). Loss of sensory input increases the intrinsic excitability of layer 5 pyramidal neurons in rat barrel cortex. *J Physiol* 587**,** 5107-5119.

Britten, R.A., Davis, L.K., Jewell, J.S., Miller, V.D., Hadley, M.M., Sanford, L.D., Machida, M., and Lonart, G. (2014). Exposure to Mission Relevant Doses of 1 GeV/Nucleon Fe Particles Leads to Impairment of Attentional Set-Shifting Performance in Socially Mature Rats. *Radiat Res*.

Buckmaster, P.S. (2012a). Mossy cell dendritic structure quantified and compared with other hippocampal neurons labeled in rats in vivo. *Epilepsia* 53 Suppl 1**,** 9-17.

Buckmaster, P.S. (2012b). "Mossy Fiber Sprouting in the Dentate Gyrus," in *Jasper's Basic Mechanisms of the Epilepsies,* eds. J.L. Noebels, M. Avoli, M.A. Rogawski, R.W. Olsen & A.V. Delgado-Escueta. (Bethesda (MD): National Center for Biotechnology Information (US)

Michael A Rogawski, Antonio V Delgado-Escueta, Jeffrey L Noebels, Massimo Avoli and Richard W Olsen.).

Buckmaster, P.S., and Dudek, F.E. (1997). Neuron loss, granule cell axon reorganization, and functional changes in the dentate gyrus of epileptic kainate-treated rats. *J Comp Neurol* 385**,** 385-404.

Buckmaster, P.S., and Dudek, F.E. (1999). In vivo intracellular analysis of granule cell axon reorganization in epileptic rats. *J Neurophysiol* 81**,** 712-721.

Buckmaster, P.S., and Jongen-Relo, A.L. (1999). Highly specific neuron loss preserves lateral inhibitory circuits in the dentate gyrus of kainate-induced epileptic rats. *J Neurosci* 19**,** 9519-9529.

Burns, S.P., Santaniello, S., Yaffe, R.B., Jouny, C.C., Crone, N.E., Bergey, G.K., Anderson, W.S., and Sarma, S.V. (2014). Network dynamics of the brain and influence of the

epileptic seizure onset zone. *Proceedings of the National Academy of Sciences* 111**,** E5321-E5330.

Buzsaki, G. (2002). Theta oscillations in the hippocampus. *Neuron* 33**,** 325-340.

Caffrey, J.M., Eng, D.L., Black, J.A., Waxman, S.G., and Kocsis, J.D. (1992). Three types of sodium channels in adult rat dorsal root ganglion neurons. *Brain Res* 592**,** 283-297.

Calabresi, P., Castrioto, A., Di Filippo, M., and Picconi, B. (2013). New experimental and clinical links between the hippocampus and the dopaminergic system in Parkinson's disease. *Lancet Neurol* 12**,** 811-821.

Chakraborti, A., Allen, A., Allen, B., Rosi, S., and Fike, J.R. (2012). Cranial irradiation alters dendritic spine density and morphology in the hippocampus. *PLoS One* 7**,** e40844.

Chauvière, L., Doublet, T., Ghestem, A., Siyoucef, S.S., Wendling, F., Huys, R., Jirsa, V., Bartolomei, F., and Bernard, C. (2012). Changes in interictal spike features precede the onset of temporal lobe epilepsy. *Annals of neurology* 71**,** 805-814.

Chawla, M.K., Guzowski, J.F., Ramirez-Amaya, V., Lipa, P., Hoffman, K.L., Marriott, L.K., Worley, P.F., Mcnaughton, B.L., and Barnes, C.A. (2005). Sparse, environmentally selective expression of Arc RNA in the upper blade of the rodent fascia dentata by brief spatial experience. *Hippocampus* 15**,** 579-586.

Chen, B.L., Hall, D.H., and Chklovskii, D.B. (2006). Wiring optimization can relate neuronal structure and function. *Proceedings of the National Academy of Sciences of the United States of America* 103**,** 4723-4728.

Cherniak, C. (1992). Local optimization of neuron arbors. *Biological Cybernetics* 66**,** 503-510.

Cherniak, C. (1994). Component placement optimization in the brain. *J Neurosci* 14**,** 2418-2427.

Chiang, A.-S., Lin, C.-Y., Chuang, C.-C., Chang, H.-M., Hsieh, C.-H., Yeh, C.-W., Shih, C.-T., Wu, J.-J., Wang, G.-T., Chen, Y.-C., Wu, C.-C., Chen, G.-Y., Ching, Y.-T., Lee, P.-C., Lin, C.-Y., Lin, H.-H., Wu, C.-C., Hsu, H.-W., Huang, Y.-A., Chen, J.-Y., Chiang, H.-J., Lu, C.-F., Ni, R.-F., Yeh, C.-Y., and Hwang, J.-K. (2011). Three-Dimensional Reconstruction of Brain-wide Wiring Networks in Drosophila at Single-Cell Resolution. *Current Biology* 21**,** 1-11.

Chklovskii, D.B. (2000). Optimal sizes of dendritic and axonal arbors in a topographic projection. *J Neurophysiol* 83**,** 2113-2119.

Chklovskii, D.B., Schikorski, T., and Stevens, C.F. (2002). Wiring Optimization in Cortical Circuits. *Neuron* 34**,** 341-347.

Chklovskii, D.B., Vitaladevuni, S., and Scheffer, L.K. (2010). Semi-automated reconstruction of neural circuits using electron microscopy. *Current Opinion in Neurobiology* 20**,** 667-675.

Choi, Y.B., and Lipton, S.A. (2000). Redox modulation of the NMDA receptor. *Cell Mol Life Sci* 57**,** 1535-1541.

Claiborne, B.J., Amaral, D.G., and Cowan, W.M. (1990). Quantitative, three-dimensional analysis of granule cell dendrites in the rat dentate gyrus. *J Comp Neurol* 302**,** 206-219.

Crill, W.E. (1996). Persistent sodium current in mammalian central neurons. *Annu Rev Physiol* 58**,** 349-362.

Crossen, J.R., Garwood, D., Glatstein, E., and Neuwelt, E.A. (1994). Neurobehavioral sequelae of cranial irradiation in adults: a review of radiation-induced encephalopathy. *J Clin Oncol* 12**,** 627-642.

Cucinotta, F.A., Alp, M., Sulzman, F.M., and Wang, M. (2014). Space radiation risks to the central nervous system. *Life Sciences in Space Research* 2**,** 54-69.

Cucinotta, F.A., and Durante, M. (2006). Cancer risk from exposure to galactic cosmic rays: implications for space exploration by human beings. *Lancet Oncol* 7**,** 431-435.

Cucinotta, F.A., Wilson, J.W., Shinn, J.L., Badavi, F.F., and Badhwar, G.D. (1996). Effects of target fragmentation on evaluation of LET spectra from space radiations: implications for space radiation protection studies. *Radiat Meas* 26**,** 923-934.

Cudmore, R.H., Fronzaroli-Molinieres, L., Giraud, P., and Debanne, D. (2010). Spike-time precision and network synchrony are controlled by the homeostatic regulation of the D-type potassium current. *J Neurosci* 30**,** 12885-12895.

Cuntz, H., Borst, A., and Segev, I. (2007). Optimization principles of dendritic structure. *Theor Biol Med Model* 4**,** 21.

Cuntz, H., Forstner, F., Borst, A., and Hausser, M. (2010). One rule to grow them all: a general theory of neuronal branching and its practical application. *PLoS Comput Biol* 6.

Cuntz, H., Forstner, F., Borst, A., and Hausser, M. (2011). The TREES toolbox--probing the basis of axonal and dendritic branching. *Neuroinformatics* 9**,** 91-96.

Cuntz, H., Forstner, F., Haag, J., and Borst, A. (2008). The morphological identity of insect dendrites. *PLoS Comput Biol* 4**,** e1000251.

Cuntz, H., Mathy, A., and Hausser, M. (2012). A scaling law derived from optimal dendritic wiring. *Proc Natl Acad Sci U S A* 109**,** 11014-11018.

Curtis, H.J. (1963). Biological mechanisms underlying the aging process. *Science* 141**,** 686-694.

Curtis, S.B., Vazquez, M.E., Wilson, J.W., Atwell, W., Kim, M., and Capala, J. (1998). Cosmic ray hit frequencies in critical sites in the central nervous system. *Adv Space Res* 22**,** 197-207.

Cutsuridis, V., Cobb, S., and Graham, B.P. (2010). Encoding and retrieval in a model of the hippocampal CA1 microcircuit. *Hippocampus* 20**,** 423-446.

Cymerblit-Sabba, A., and Schiller, Y. (2012). Development of hypersynchrony in the cortical network during chemoconvulsant-induced epileptic seizures in vivo. *J Neurophysiol* 107**,** 1718-1730.

Davis, G.W., and Bezprozvanny, I. (2001). Maintaining the stability of neural function: a homeostatic hypothesis. *Annu Rev Physiol* 63**,** 847-869.

Dekosky, S.T., Scheff, S.W., and Styren, S.D. (1996). Structural correlates of cognition in dementia: quantification and assessment of synapse change. *Neurodegeneration* 5**,** 417-421.

Desai, N.S., Rutherford, L.C., and Turrigiano, G.G. (1999). Plasticity in the intrinsic excitability of cortical pyramidal neurons. *Nat Neurosci* 2**,** 515-520.

Donohue, D.E., Scorcioni, R., and Ascoli, G.A. (2002). "Generation and description of neuronal morphology using L-Neuron: a case study," in *Computational Neuroanatomy: Principles and Methods,* ed. G.A. Ascoli. (Totowa, NJ: Humana), 49-70.

Dyhrfjeld-Johnsen, J., Santhakumar, V., Morgan, R.J., Huerta, R., Tsimring, L., and Soltesz, I. (2007). Topological determinants of epileptogenesis in large-scale structural and functional models of the dentate gyrus derived from experimental data. *J Neurophysiol* 97**,** 1566-1587.

Eberhard, J., Wanner, A., and Wittum, G. (2006). NeuGen: a tool for the generation of realistic morphology of cortical neurons and neural networks in 3D. *Neurocomputing* 70**,** 327-342.

Echegoyen, J., Neu, A., Graber, K.D., and Soltesz, I. (2007). Homeostatic plasticity studied using in vivo hippocampal activity-blockade: synaptic scaling, intrinsic plasticity and age-dependence. *PLoS One* 2**,** e700.

Engel, J. (2013). *Seizures and epilepsy.* Oxford University Press.

Engel, J., Pedley, T.A., and Aicardi, J. (2008). *Epilepsy: a comprehensive textbook.* Lippincott Williams & Wilkins.

Engel Jr, J., Bragin, A., Staba, R., and Mody, I. (2009). High-frequency oscillations: What is normal and what is not? *Epilepsia* 50**,** 598-604.

Fan, Y., Fricker, D., Brager, D.H., Chen, X., Lu, H.C., Chitwood, R.A., and Johnston, D. (2005). Activity-dependent decrease of excitability in rat hippocampal neurons through increases in I(h). *Nat Neurosci* 8**,** 1542-1551.

Fatt, P., and Katz, B. (1951). An analysis of the end-plate potential recorded with an intracellular electrode. *J Physiol* 115**,** 320-370.

Fattoretti, P., Balietti, M., Casoli, T., Giorgetti, B., Di Stefano, G., Bertoni-Freddari, C., Lattanzio, F., and Sensi, S.L. (2010). Decreased numeric density of succinic dehydrogenase-positive mitochondria in CA1 pyramidal neurons of 3xTg-AD mice. *Rejuvenation Res* 13**,** 144-147.

Feldt Muldoon, S., Soltesz, I., and Cossart, R. (2013). Spatially clustered neuronal assemblies comprise the microstructure of synchrony in chronically epileptic networks. *Proc Natl Acad Sci U S A* 110**,** 3567-3572.

French, C.R., Sah, P., Buckett, K.J., and Gage, P.W. (1990). A voltage-dependent persistent sodium current in mammalian hippocampal neurons. *J Gen Physiol* 95**,** 1139-1157.

Freund, T.F., and Buzsáki, G. (1996). Interneurons of the hippocampus. *Hippocampus* 6**,** 347-470.

Gabriel, S., Njunting, M., Pomper, J.K., Merschhemke, M., Sanabria, E.R., Eilers, A., Kivi, A., Zeller, M., Meencke, H.J., Cavalheiro, E.A., Heinemann, U., and Lehmann, T.N. (2004). Stimulus and potassium-induced epileptiform activity in the human dentate gyrus from patients with and without hippocampal sclerosis. *J Neurosci* 24**,** 10416-10430.

Garcia-Sancho, J., and Herreros, B. (1983). Effects of redox agents on the Ca2+-activated K+ channel. *Cell Calcium* 4**,** 493-497.

Giedzinski, E., Rola, R., Fike, J.R., and Limoli, C.L. (2005). Efficient production of reactive oxygen species in neural precursor cells after exposure to 250 MeV protons. *Radiat Res* 164**,** 540-544.

Gleeson, P., Steuber, V., and Silver, R.A. (2007). neuroConstruct: a tool for modeling networks of neurons in 3D space. *Neuron* 54**,** 219-235.

Goddard, N., and Hood, G. (1998). "Large-Scale Simulation Using Parallel GENESIS," in *The Book of GENESIS*. Springer New York), 349-379.

Golomb, D. (1998). Models of neuronal transient synchrony during propagation of activity through neocortical circuitry. *Journal of neurophysiology* 79**,** 1-12.

Golowasch, J., Goldman, M.S., Abbott, L.F., and Marder, E. (2002). Failure of averaging in the construction of a conductance-based neuron model. *J Neurophysiol* 87**,** 1129-1131.

Gu, Y., Arruda-Carvalho, M., Wang, J., Janoschka, S.R., Josselyn, S.A., Frankland, P.W., and Ge, S. (2012). Optical controlling reveals time-dependent roles for adult-born dentate granule cells. *Nat Neurosci* 15**,** 1700-1706.

Guan, J., Stewart, J., Ware, J.H., Zhou, Z., Donahue, J.J., and Kennedy, A.R. (2006). Effects of dietary supplements on the space radiation-induced reduction in total antioxidant status in CBA mice. *Radiat Res* 165**,** 373-378.

Gupta, J.R., Marsh, E.D., Nieh, H.A., Porter, B.E., and Litt, B. (2011). Discrete gamma oscillations identify the seizure onset zone in some pediatric epilepsy patients. *Conf Proc IEEE Eng Med Biol Soc* 2011**,** 3095-3098.

Gutkin, B.S., Laing, C.R., Colby, C.L., Chow, C.C., and Ermentrout, G.B. (2001). Turning on and off with excitation: the role of spike-timing asynchrony and synchrony in sustained neural activity. *Journal of computational neuroscience* 11**,** 121-134.

Halabisky, B., Parada, I., Buckmaster, P.S., and Prince, D.A. (2010). Excitatory input onto hilar somatostatin interneurons is increased in a chronic model of epilepsy. *J Neurophysiol* 104**,** 2214-2223.

Hammarstrom, A.K., and Gage, P.W. (1999). Nitric oxide increases persistent sodium current in rat hippocampal neurons. *J Physiol* 520 Pt 2**,** 451-461.

Han, Z.S., Buhl, E.H., Lörinczi, Z., and Somogyi, P. (1993). A High Degree of Spatial Selectivity in the Axonal and Dendritic Domains of Physiologically Identified Local-circuit Neurons in the Dentate Gyms of the Rat Hippocampus. *European Journal of Neuroscience* 5**,** 395-410.

Harman, D. (1992). Free radical theory of aging. *Mutat Res* 275**,** 257-266.

Hassler, D.M., Zeitlin, C., Wimmer-Schweingruber, R.F., Ehresmann, B., Rafkin, S., Eigenbrode, J.L., Brinza, D.E., Weigle, G., Bottcher, S., Bohm, E., Burmeister, S., Guo, J., Kohler, J., Martin, C., Reitz, G., Cucinotta, F.A., Kim, M.H., Grinspoon, D., Bullock, M.A., Posner, A., Gomez-Elvira, J., Vasavada, A., Grotzinger, J.P., Team, M.S., and The, M.S.L.S.T. (2013). Mars' Surface Radiation Environment Measured with the Mars Science Laboratory's Curiosity Rover. *Science*.

Hauss-Wegrzyniak, B., Vannucchi, M.G., and Wenk, G.L. (2000). Behavioral and ultrastructural changes induced by chronic neuroinflammation in young rats. *Brain Res* 859**,** 157-166.

Hay, E., Schurmann, F., Markram, H., and Segev, I. (2013). Preserving axosomatic spiking features despite diverse dendritic morphology. *J Neurophysiol* 109**,** 2972-2981.

Helmstaedter, M., Briggman, K.L., and Denk, W. (2008). 3D structural imaging of the brain with photons and electrons. *Current Opinion in Neurobiology* 18**,** 633-641.

Helmstaedter, M., Briggman, K.L., and Denk, W. (2011). High-accuracy neurite reconstruction for high-throughput neuroanatomy. *Nat Neurosci* 14**,** 1081-1088.

Helmstaedter, M., Briggman, K.L., Turaga, S.C., Jain, V., Seung, H.S., and Denk, W. (2013). Connectomic reconstruction of the inner plexiform layer in the mouse retina. *Nature* 500**,** 168-174.

Hester, M.S., and Danzer, S.C. (2013). Accumulation of abnormal adult-generated hippocampal granule cells predicts seizure frequency and severity. *J Neurosci* 33**,** 8926-8936.

Hill, S.L., Wang, Y., Riachi, I., Schurmann, F., and Markram, H. (2012). Statistical connectivity provides a sufficient foundation for specific functional connectivity in neocortical neural microcircuits. *Proc Natl Acad Sci U S A* 109**,** E2885-2894.

Hines, M.L., and Carnevale, N.T. (1997). The NEURON simulation environment. *Neural Comput* 9**,** 1179-1209.

Hines, M.L., and Carnevale, N.T. (2008). Translating network models to parallel hardware in NEURON. *J Neurosci Methods* 169**,** 425-455.

Hines, M.L., Eichner, H., and Schurmann, F. (2008a). Neuron splitting in compute-bound parallel network simulations enables runtime scaling with twice as many processors. *J Comput Neurosci* 25**,** 203-210.

Hines, M.L., Markram, H., and Schurmann, F. (2008b). Fully implicit parallel simulation of single neurons. *J Comput Neurosci* 25**,** 439-448.

Hines, M.L., Morse, T., Migliore, M., Carnevale, N.T., and Shepherd, G.M. (2004). ModelDB: A Database to Support Computational Neuroscience. *J Comput Neurosci* 17**,** 7-11.

Hof, P.R., and Morrison, J.H. (1996). Hippocampal and neocortical involvement in normal brain aging and dementia: morphological and neurochemical profile of the vulnerable circuits. *J Am Geriatr Soc* 44**,** 857-864.

Howard, A.L., Neu, A., Morgan, R.J., Echegoyen, J.C., and Soltesz, I. (2007). Opposing modifications in intrinsic currents and synaptic inputs in post-traumatic mossy cells: evidence for single-cell homeostasis in a hyperexcitable network. *J Neurophysiol* 97**,** 2394-2409.

Hu, H., Gan, J., and Jonas, P. (2014). Fast-spiking, parvalbumin+ GABAergic interneurons: From cellular design to microcircuit function. *Science* 345**,** 1255263.

Hu, H., Martina, M., and Jonas, P. (2010). Dendritic mechanisms underlying rapid synaptic activation of fast-spiking hippocampal interneurons. *Science* 327**,** 52-58.

Huang, C., Marsh, E.D., Ziskind, D.M., Celix, J.M., Peltzer, B., Brown, M.W., Storm, P.B., Litt, B., and Porter, B.E. (2012). Leaving tissue associated with infrequent intracranial EEG seizure onsets is compatible with post-operative seizure freedom. *Journal of pediatric epilepsy* 1**,** 211-219.

Huang, X., Xu, W., Liang, J., Takagaki, K., Gao, X., and Wu, J.-Y. (2010). Spiral wave dynamics in neocortex. *Neuron* 68**,** 978-990.

Iball, J., and Ali, A.B. (2011). Endocannabinoid release modulates electrical coupling between CCK cells connected via chemical and electrical synapses in CA1. *Frontiers in neural circuits* 5.

Imayoshi, I., Sakamoto, M., Ohtsuka, T., Takao, K., Miyakawa, T., Yamaguchi, M., Mori, K., Ikeda, T., Itohara, S., and Kageyama, R. (2008). Roles of continuous neurogenesis in the structural and functional integrity of the adult forebrain. *Nat Neurosci* 11**,** 1153-1161.

Jacinto, L.R., Reis, J.S., Dias, N.S., Cerqueira, J.J., Correia, J.H., and Sousa, N. (2013). Stress affects theta activity in limbic networks and impairs novelty-induced exploration and familiarization. *Front Behav Neurosci* 7**,** 127.

Jacobs, J., Levan, P., Chander, R., Hall, J., Dubeau, F., and Gotman, J. (2008). Interictal high-frequency oscillations (80-500 Hz) are an indicator of seizure onset areas independent of spikes in the human epileptic brain. *Epilepsia* 49**,** 1893-1907.

Jacobs, J., Levan, P., Chatillon, C.E., Olivier, A., Dubeau, F., and Gotman, J. (2009). High frequency oscillations in intracranial EEGs mark epileptogenicity rather than lesion type. *Brain* 132**,** 1022-1037.

Jedlicka, P., Deller, T., and Schwarzacher, S.W. (2010). Computational modeling of GABAA receptor-mediated paired-pulse inhibition in the dentate gyrus. *J Comput Neurosci* 29**,** 509-519.

Jedlicka, P., Hoon, M., Papadopoulos, T., Vlachos, A., Winkels, R., Poulopoulos, A., Betz, H., Deller, T., Brose, N., Varoqueaux, F., and Schwarzacher, S.W. (2011). Increased dentate gyrus excitability in neuroligin-2-deficient mice in vivo. *Cereb Cortex* 21**,** 357-367.

Jinno, S., Aika, Y., Fukuda, T., and Kosaka, T. (1999). Quantitative analysis of neuronal nitric oxide synthase-immunoreactive neurons in the mouse hippocampus with optical disector. *Journal of Comparative Neurology* 410**,** 398-412.

Jirsa, V.K., Stacey, W.C., Quilichini, P.P., Ivanov, A.I., and Bernard, C. (2014). On the nature of seizure dynamics. *Brain* 137**,** 2210-2230.

Jiruska, P., De Curtis, M., Jefferys, J.G., Schevon, C.A., Schiff, S.J., and Schindler, K. (2013). Synchronization and desynchronization in epilepsy: controversies and hypotheses. *J Physiol* 591**,** 787-797.

Kalia, M. (2005). Neurobiological basis of depression: an update. *Metabolism* 54**,** 24-27.

Kamsler, A., and Segal, M. (2003). Hydrogen peroxide modulation of synaptic plasticity. *J Neurosci* 23**,** 269-276.

Kaufmann, W.E., and Moser, H.W. (2000). Dendritic anomalies in disorders associated with mental retardation. *Cereb Cortex* 10**,** 981-991.

Kay, A.R., Sugimori, M., and Llinas, R. (1998). Kinetic and stochastic properties of a persistent sodium current in mature guinea pig cerebellar Purkinje cells. *J Neurophysiol* 80**,** 1167-1179.

Keller, C.J., Truccolo, W., Gale, J.T., Eskandar, E., Thesen, T., Carlson, C., Devinsky, O., Kuzniecky, R., Doyle, W.K., and Madsen, J.R. (2010). Heterogeneous neuronal firing patterns during interictal epileptiform discharges in the human cortex. *Brain* 133**,** 1668-1681.

Klausberger, T., Magill, P.J., Marton, L.F., Roberts, J.D., Cobden, P.M., Buzsaki, G., and Somogyi, P. (2003). Brain-state- and cell-type-specific firing of hippocampal interneurons in vivo. *Nature* 421**,** 844-848.

Klausberger, T., Marton, L.F., Baude, A., Roberts, J.D., Magill, P.J., and Somogyi, P. (2004). Spike timing of dendrite-targeting bistratified cells during hippocampal network oscillations in vivo. *Nat Neurosci* 7**,** 41-47.

Koene, R.A., Tijms, B., Van Hees, P., Postma, F., De Ridder, A., Ramakers, G.J., Van Pelt, J., and Van Ooyen, A. (2009). NETMORPH: a framework for the stochastic generation of large scale neuronal networks with realistic neuron morphologies. *Neuroinformatics* 7**,** 195-210.

Kramer, J.H., Crowe, A.B., Larson, D.A., Sneed, P.K., Gutin, P.H., Mcdermott, M.W., and Prados, M.D. (1997). Neuropsychological sequelae of medulloblastoma in adults. *Int J Radiat Oncol Biol Phys* 38**,** 21-26.

Krichmar, J.L., Nasuto, S.J., Scorcioni, R., Washington, S.D., and Ascoli, G.A. (2002). Effects of dendritic morphology on CA3 pyramidal cell electrophysiology: a simulation study. *Brain Res* 941**,** 11-28.

Kron, M.M., Zhang, H., and Parent, J.M. (2010). The developmental stage of dentate granule cells dictates their contribution to seizure-induced plasticity. *J Neurosci* 30**,** 2051-2059.

Krook-Magnuson, E., Armstrong, C., Oijala, M., and Soltesz, I. (2013). On-demand optogenetic control of spontaneous seizures in temporal lobe epilepsy. *Nature communications* 4**,** 1376.

Krook-Magnuson, E., Ledri, M., Soltesz, I., and Kokaia, M. (2014a). "How might novel technologies such as optogenetics lead to better treatments in epilepsy?," in *Issues in Clinical Epileptology: A View from the Bench*. Springer), 319-336.

Krook-Magnuson, E., Szabo, G.G., Armstrong, C., Oijala, M., and Soltesz, I. (2014b). Cerebellar Directed Optogenetic Intervention Inhibits Spontaneous Hippocampal Seizures in a Mouse Model of Temporal Lobe Epilepsy. *eneuro* 1**,** ENEURO. 0005-0014.2014.

Krueppel, R., Remy, S., and Beck, H. (2011). Dendritic integration in hippocampal dentate granule cells. *Neuron* 71**,** 512-528.

Lang, S., Dercksen, V.J., Sakmann, B., and Oberlaender, M. (2011). Simulation of signal flow in 3D reconstructions of an anatomically realistic neural network in rat vibrissal cortex. *Neural Networks* 24**,** 998-1011.

Lee, P.W., Hung, B.K., Woo, E.K., Tai, P.T., and Choi, D.T. (1989). Effects of radiation therapy on neuropsychological functioning in patients with nasopharyngeal carcinoma. *J Neurol Neurosurg Psychiatry* 52**,** 488-492.

Lee, S.-H., Marchionni, I., Bezaire, M., Varga, C., Danielson, N., Lovett-Barron, M., Losonczy, A., and Soltesz, I. (2014). Parvalbumin-positive basket cells differentiate among hippocampal pyramidal cells. *Neuron*.

Lei, S.Z., Pan, Z.H., Aggarwal, S.K., Chen, H.S., Hartman, J., Sucher, N.J., and Lipton, S.A. (1992). Effect of nitric oxide production on the redox modulatory site of the NMDA receptor-channel complex. *Neuron* 8**,** 1087-1099.

Limoli, C.L., Giedzinski, E., Baure, J., Rola, R., and Fike, J.R. (2007). Redox changes induced in hippocampal precursor cells by heavy ion irradiation. *Radiat Environ Biophys* 46**,** 167-172.

Limoli, C.L., Hartmann, A., Shephard, L., Yang, C.R., Boothman, D.A., Bartholomew, J., and Morgan, W.F. (1998). Apoptosis, reproductive failure, and oxidative stress in Chinese hamster ovary cells with compromised genomic integrity. *Cancer Res* 58**,** 3712-3718.

Lipton, S.A., Rayudu, P.V., Choi, Y.B., Sucher, N.J., and Chen, H.S. (1998). Redox modulation of the NMDA receptor by NO-related species. *Prog Brain Res* 118**,** 73-82.

Lübbers, K., and Frotscher, M. (1988). Differentiation of granule cells in relation to GABAergic neurons in the rat fascia dentata. *Anatomy and Embryology* 178**,** 119-127.

Magistretti, J., and Alonso, A. (1999). Biophysical properties and slow voltage-dependent inactivation of a sustained sodium current in entorhinal cortex layer-II principal neurons: a whole-cell and single-channel study. *J Gen Physiol* 114**,** 491-509.

Mainen, Z.F., and Sejnowski, T.J. (1996). Influence of dendritic structure on firing pattern in model neocortical neurons. *Nature* 382**,** 363-366.

Maletic, V., Robinson, M., Oakes, T., Iyengar, S., Ball, S.G., and Russell, J. (2007). Neurobiology of depression: an integrated view of key findings. *Int J Clin Pract* 61**,** 2030-2040.

Manda, K., Ueno, M., and Anzai, K. (2008). Memory impairment, oxidative damage and apoptosis induced by space radiation: ameliorative potential of alpha-lipoic acid. *Behav Brain Res* 187**,** 387-395.

Marder, E., and Prinz, A.A. (2003). Current compensation in neuronal homeostasis. *Neuron* 37**,** 2-4.

Margerison, J.H., and Corsellis, J.A. (1966). Epilepsy and the temporal lobes. A clinical, electroencephalographic and neuropathological study of the brain in epilepsy, with particular reference to the temporal lobes. *Brain* 89**,** 499-530.

Marty, A., and Neher, E. (1995). "Tight-Seal Whole-Cell Recording," in *Single-Channel Recording,* eds. B. Sackmann & E. Neher (New York, New York: Plenum Press).

Matalon, S., Hardiman, K.M., Jain, L., Eaton, D.C., Kotlikoff, M., Eu, J.P., Sun, J., Meissner, G., and Stamler, J.S. (2003). Regulation of ion channel structure and function by reactive oxygen-nitrogen species. *Am J Physiol Lung Cell Mol Physiol* 285**,** L1184-1189.

Mateos-Aparicio, P., Murphy, R., and Storm, J.F. (2014). Complementary functions of SK and Kv7/M potassium channels in excitability control and synaptic integration in rat hippocampal dentate granule cells. *J Physiol* 592**,** 669-693.

Memelli, H., Torben-Nielsen, B., and Kozloski, J. (2013). Self-referential forces are sufficient to explain different dendritic morphologies. *Front Neuroinform* 7**,** 1.

Meyer, A.H., Katona, I., Blatow, M., Rozov, A., and Monyer, H. (2002). In vivo labeling of parvalbumin-positive interneurons and analysis of electrical coupling in identified neurons. *The Journal of neuroscience* 22**,** 7055-7064.

Migliore, M., Cannia, C., Lytton, W.W., Markram, H., and Hines, M.L. (2006). Parallel network simulations with NEURON. *J Comput Neurosci* 21**,** 119-129.

Migliore, M., Morse, T.M., Davison, A.P., Marenco, L., Shepherd, G.M., and Hines, M.L. (2003). ModelDB: making models publicly accessible to support computational neuroscience. *Neuroinformatics* 1**,** 135-139.

Milner, B. (1974). "Hemispheric specialization: scope and limits," in *The neurosciences: third studyprogram,* ed. W.F. Schmitt Fo. (Cambridge, MA: MIT Press), 75–89.

Mizuseki, K., Diba, K., Pastalkova, E., and Buzsáki, G. (2011). Hippocampal CA1 pyramidal cells form functionally distinct sublayers. *Nature neuroscience* 14**,** 1174-1181.

Molnar, P., and Nadler, J.V. (1999). Mossy fiber-granule cell synapses in the normal and epileptic rat dentate gyrus studied with minimal laser photostimulation. *J Neurophysiol* 82**,** 1883-1894.

Morgan, R.J., and Soltesz, I. (2008). Nonrandom connectivity of the epileptic dentate gyrus predicts a major role for neuronal hubs in seizures. *Proc Natl Acad Sci U S A* 105**,** 6179-6184.

Mrsic-Flogel, T.D., Hofer, S.B., Ohki, K., Reid, R.C., Bonhoeffer, T., and Hubener, M. (2007). Homeostatic regulation of eye-specific responses in visual cortex during ocular dominance plasticity. *Neuron* 54**,** 961-972.

Netoff, T.I., and Schiff, S.J. (2002). Decreased neuronal synchronization during experimental seizures. *The Journal of neuroscience* 22**,** 7297-7307.

Nicholls, J.G.M., A.R.; Wallace B.G.; Fuchs P.A. (2012). "Ionic Basis of the Action Potential," in *From Neuron to Brain: A Cellular and Molecular Approach to the Function of the Nervous System*. 5th ed (Sunderland, MA: Sinauer Associates, Inc.), 99-128.

Nishimura, M., Gu, X., and Swann, J.W. (2011). Seizures in early life suppress hippocampal dendrite growth while impairing spatial learning. *Neurobiol Dis* 44**,** 205-214.

Norenberg, A., Hu, H., Vida, I., Bartos, M., and Jonas, P. (2010). Distinct nonuniform cable properties optimize rapid and efficient activation of fast-spiking GABAergic interneurons. *Proc Natl Acad Sci U S A* 107**,** 894-899.

Oberlaender, M., De Kock, C.P.J., Bruno, R.M., Ramirez, A., Meyer, H.S., Dercksen, V.J., Helmstaedter, M., and Sakmann, B. (2012). Cell Type–Specific Three-Dimensional Structure of Thalamocortical Circuits in a Column of Rat Vibrissal Cortex. *Cerebral Cortex* 22**,** 2375-2391.

Olanow, C.W. (1993). A radical hypothesis for neurodegeneration. *Trends Neurosci* 16**,** 439-444.

Parent, J.M., and Kron, M.M. (2012). "Neurogenesis and Epilepsy," in *Jasper's Basic Mechanisms of the Epilepsies,* eds. J.L. Noebels, M. Avoli, M.A. Rogawski, R.W. Olsen & A.V. Delgado-Escueta. (Bethesda (MD): National Center for Biotechnology Information (US)

Michael A Rogawski, Antonio V Delgado-Escueta, Jeffrey L Noebels, Massimo Avoli and Richard W Olsen.).

Parihar, V.K., and Limoli, C.L. (2013). Cranial irradiation compromises neuronal architecture in the hippocampus. *Proc Natl Acad Sci U S A* 110**,** 12822-12827.

Paz, J.T., Davidson, T.J., Frechette, E.S., Delord, B., Parada, I., Peng, K., Deisseroth, K., and Huguenard, J.R. (2013). Closed-loop optogenetic control of thalamus as a tool for interrupting seizures after cortical injury. *Nature neuroscience* 16**,** 64-70.

Pearce, A., Wulsin, D., Blanco, J.A., Krieger, A., Litt, B., and Stacey, W.C. (2013). Temporal changes of neocortical high-frequency oscillations in epilepsy. *Journal of neurophysiology* 110**,** 1167-1179.

Peng, Z., Zhang, N., Wei, W., Huang, C.S., Cetina, Y., Otis, T.S., and Houser, C.R. (2013). A reorganized GABAergic circuit in a model of epilepsy: evidence from optogenetic labeling and stimulation of somatostatin interneurons. *J Neurosci* 33**,** 14392-14405.

Perez-Cruz, C., Nolte, M.W., Van Gaalen, M.M., Rustay, N.R., Termont, A., Tanghe, A., Kirchhoff, F., and Ebert, U. (2011). Reduced spine density in specific regions of CA1 pyramidal neurons in two transgenic mouse models of Alzheimer's disease. *J Neurosci* 31**,** 3926-3934.

Piatti, V.C., Ewell, L.A., and Leutgeb, J.K. (2013). Neurogenesis in the dentate gyrus: carrying the message or dictating the tone. *Front Neurosci* 7**,** 50.

Picardo, M.A., Guigue, P., Bonifazi, P., Batista-Brito, R., Allene, C., Ribas, A., Fishell, G., Baude, A., and Cossart, R. (2011). Pioneer GABA cells comprise a subpopulation of hub neurons in the developing hippocampus. *Neuron* 71**,** 695-709.

Pieri, M., Carunchio, I., Curcio, L., Mercuri, N.B., and Zona, C. (2009). Increased persistent sodium current determines cortical hyperexcitability in a genetic model of amyotrophic lateral sclerosis. *Exp Neurol* 215**,** 368-379.

Procter, A.W. (1996). Neurochemical correlates of dementia. *Neurodegeneration* 5**,** 403-407.

Raber, J., Rola, R., Lefevour, A., Morhardt, D., Curley, J., Mizumatsu, S., Vandenberg, S.R., and Fike, J.R. (2004). Radiation-induced cognitive impairments are associated with changes in indicators of hippocampal neurogenesis. *Radiat Res* 162**,** 39-47.

Rapp, P.R., and Gallagher, M. (1996). Preserved neuron number in the hippocampus of aged rats with spatial learning deficits. *Proc Natl Acad Sci U S A* 93**,** 9926-9930.

Rein, K., Zöckler, M., Mader, M.T., Grübel, C., and Heisenberg, M. (2002). The Drosophila Standard Brain. *Current Biology* 12**,** 227-231.

Rola, R., Raber, J., Rizk, A., Otsuka, S., Vandenberg, S.R., Morhardt, D.R., and Fike, J.R. (2004). Radiation-induced impairment of hippocampal neurogenesis is associated with cognitive deficits in young mice. *Exp Neurol* 188**,** 316-330.

Rola, R., Zou, Y., Huang, T.T., Fishman, K., Baure, J., Rosi, S., Milliken, H., Limoli, C.L., and Fike, J.R. (2007). Lack of extracellular superoxide dismutase (EC-SOD) in the microenvironment impacts radiation-induced changes in neurogenesis. *Free Radic Biol Med* 42**,** 1133-1145; discussion 1131-1132.

Ropireddy, D., Bachus, S.E., and Ascoli, G.A. (2012). Non-homogeneous stereological properties of the rat hippocampus from high-resolution 3D serial reconstruction of thin histological sections. *Neuroscience* 205**,** 91-111.

Ross, S.T., and Soltesz, I. (2000). Selective depolarization of interneurons in the early posttraumatic dentate gyrus: involvement of the Na(+)/K(+)-ATPase. *J Neurophysiol* 83**,** 2916-2930.

Santhakumar, V., Aradi, I., and Soltesz, I. (2005). Role of mossy fiber sprouting and mossy cell loss in hyperexcitability: a network model of the dentate gyrus incorporating cell types and axonal topography. *J Neurophysiol* 93**,** 437-453.

Savanthrapadian, S., Meyer, T., Elgueta, C., Booker, S.A., Vida, I., and Bartos, M. (2014). Synaptic Properties of SOM- and CCK-Expressing Cells in Dentate Gyrus Interneuron Networks. *J Neurosci* 34**,** 8197-8209.

Schaefer, A.T., Larkum, M.E., Sakmann, B., and Roth, A. (2003). Coincidence detection in pyramidal neurons is tuned by their dendritic branching pattern. *J Neurophysiol* 89**,** 3143-3154.

Schevon, C.A., Weiss, S.A., Mckhann Jr, G., Goodman, R.R., Yuste, R., Emerson, R.G., and Trevelyan, A.J. (2012). Evidence of an inhibitory restraint of seizure activity in humans. *Nature communications* 3**,** 1060.

Schmidt-Hieber, C., and Bischofberger, J. (2010). Fast sodium channel gating supports localized and efficient axonal action potential initiation. *J Neurosci* 30**,** 10233-10242.

Schmidt-Hieber, C., Jonas, P., and Bischofberger, J. (2004). Enhanced synaptic plasticity in newly generated granule cells of the adult hippocampus. *Nature* 429**,** 184-187.

Schmidt-Hieber, C., Jonas, P., and Bischofberger, J. (2007). Subthreshold dendritic signal processing and coincidence detection in dentate gyrus granule cells. *J Neurosci* 27**,** 8430-8441.

Schneider, C.J., Bezaire, M., and Soltesz, I. (2012). Toward a full-scale computational model of the rat dentate gyrus. *Front Neural Circuits* 6**,** 83.

Scorcioni, R., Bouteiller, J.-M., and Ascoli, G.A. (2002). A real-scale anatomical model of the dentate gyrus based on single cell reconstructions and 3D rendering of a brain atlas. *Neurocomputing* 44–46**,** 629-634.

Scorcioni, R., Polavaram, S., and Ascoli, G.A. (2008). L-Measure: a web-accessible tool for the analysis, comparison and search of digital reconstructions of neuronal morphologies. *Nat Protoc* 3**,** 866-876.

Seress, L., and Pokorny, J. (1981). Structure of the granular layer of the rat dentate gyrus. A light microscopic and Golgi study. *J Anat* 133**,** 181-195.

Setlow, R.B. (2003). The hazards of space travel. *EMBO Rep* 4**,** 1013-1016.

Seung, H.S. (2009). Reading the book of memory: sparse sampling versus dense mapping of connectomes. *Neuron* 62**,** 17-29.

Sholl, D.A. (1953). Dendritic organization in the neurons of the visual and motor cortices of the cat. *Journal of anatomy* 87**,** 387-406.

Shukitt-Hale, B., Casadesus, G., Cantuti-Castelvetri, I., Rabin, B.M., and Joseph, J.A. (2003). Cognitive deficits induced by 56Fe radiation exposure. *Adv Space Res* 31**,** 119-126.

Shukitt-Hale, B., Szprengiel, A., Pluhar, J., Rabin, B.M., and Joseph, J.A. (2004). The effects of proton exposure on neurochemistry and behavior. *Adv Space Res* 33**,** 1334-1339.

Smart, O., Maus, D., Marsh, E., Dlugos, D., Litt, B., and Meador, K. (2012). Mapping and mining interictal pathological gamma (30–100Hz) oscillations with clinical intracranial EEG in patients with epilepsy. *Expert systems with applications* 39**,** 7355-7370.

Sokolova, I.V., Lester, H.A., and Davidson, N. (2006). Postsynaptic mechanisms are essential for forskolin-induced potentiation of synaptic transmission. *J Neurophysiol* 95**,** 2570-2579.

Sokolova, I.V., and Mody, I. (2008). Silencing-induced metaplasticity in hippocampal cultured neurons. *J Neurophysiol* 100**,** 690-697.

Soltesz, I. (2005). *Diversity in the Neuronal Machine: Order and Variability in Interneuronal Microcircuits.* Oxford University Press, USA.

Somogyi, P., and Klausberger, T. (2005). Defined types of cortical interneurone structure space and spike timing in the hippocampus. *J Physiol* 562**,** 9-26.

Spruston, N., and Johnston, D. (1992). Perforated patch-clamp analysis of the passive membrane properties of three classes of hippocampal neurons. *J Neurophysiol* 67**,** 508-529.

Squire, L.R., Stark, C.E., and Clark, R.E. (2004). The medial temporal lobe. *Annu Rev Neurosci* 27**,** 279-306.

Staba, R.J., Wilson, C.L., Bragin, A., Fried, I., and Engel, J., Jr. (2002). Quantitative analysis of high-frequency oscillations (80-500 Hz) recorded in human epileptic hippocampus and entorhinal cortex. *J Neurophysiol* 88**,** 1743-1752.

Staba, R.J., Wilson, C.L., Bragin, A., Jhung, D., Fried, I., and Engel, J., Jr. (2004). High-frequency oscillations recorded in human medial temporal lobe during sleep. *Ann Neurol* 56**,** 108-115.

Staley, K.J., and Dudek, F.E. (2006). Interictal spikes and epileptogenesis. *Epilepsy Currents* 6**,** 199-202.

Stark, G. (2005). Functional consequences of oxidative membrane damage. *J Membr Biol* 205**,** 1-16.

Sucher, N.J., and Lipton, S.A. (1991). Redox modulatory site of the NMDA receptor-channel complex: regulation by oxidized glutathione. *J Neurosci Res* 30**,** 582-591.

Sullivan, J.M., Traynelis, S.F., Chen, H.S., Escobar, W., Heinemann, S.F., and Lipton, S.A. (1994). Identification of two cysteine residues that are required for redox modulation of the NMDA subtype of glutamate receptor. *Neuron* 13**,** 929-936.

Suman, S., Rodriguez, O.C., Winters, T.A., Fornace, A.J., Jr., Albanese, C., and Datta, K. (2013). Therapeutic and space radiation exposure of mouse brain causes impaired DNA repair response and premature senescence by chronic oxidant production. *Aging (Albany NY)* 5**,** 607-622.

Surma-Aho, O., Niemela, M., Vilkki, J., Kouri, M., Brander, A., Salonen, O., Paetau, A., Kallio, M., Pyykkonen, J., and Jaaskelainen, J. (2001). Adverse long-term effects of brain radiotherapy in adult low-grade glioma patients. *Neurology* 56**,** 1285-1290.

Sweatt, J.D. (2004). Hippocampal function in cognition. *Psychopharmacology (Berl)* 174**,** 99-110.

Taneja, P., Ogier, M., Brooks-Harris, G., Schmid, D.A., Katz, D.M., and Nelson, S.B. (2009). Pathophysiology of locus ceruleus neurons in a mouse model of Rett syndrome. *J Neurosci* 29**,** 12187-12195.

Tang, L.H., and Aizenman, E. (1993a). Allosteric modulation of the NMDA receptor by dihydrolipoic and lipoic acid in rat cortical neurons in vitro. *Neuron* 11**,** 857-863.

Tang, L.H., and Aizenman, E. (1993b). The modulation of N-methyl-D-aspartate receptors by redox and alkylating reagents in rat cortical neurones in vitro. *J Physiol* 465**,** 303-323.

Tashiro, A., Makino, H., and Gage, F.H. (2007). Experience-specific functional modification of the dentate gyrus through adult neurogenesis: a critical period during an immature stage. *J Neurosci* 27**,** 3252-3259.

Terry, R.D., Peck, A., Deteresa, R., Schechter, R., and Horoupian, D.S. (1981). Some morphometric aspects of the brain in senile dementia of the Alzheimer type. *Ann Neurol* 10**,** 184-192.

Thomas, E.A., Reid, C.A., Berkovic, S.F., and Petrou, S. (2009). Prediction by modeling that epilepsy may be caused by very small functional changes in ion channels. *Arch Neurol* 66**,** 1225-1232.

Thomas, E.A., Reid, C.A., and Petrou, S. (2010). Mossy fiber sprouting interacts with sodium channel mutations to increase dentate gyrus excitability. *Epilepsia* 51**,** 136-145.

Torben-Nielsen, B., Tuyls, K., and Postma, E. (2008). EvOL-NEURON: Neuronal morphology generation. *Neurocomputing* 71**,** 963-972.

Truccolo, W., Ahmed, O.J., Harrison, M.T., Eskandar, E.N., Cosgrove, G.R., Madsen, J.R., Blum, A.S., Potter, N.S., Hochberg, L.R., and Cash, S.S. (2014). Neuronal Ensemble Synchrony during Human Focal Seizures. *The Journal of Neuroscience* 34**,** 9927-9944.

Truccolo, W., Donoghue, J.A., Hochberg, L.R., Eskandar, E.N., Madsen, J.R., Anderson, W.S., Brown, E.N., Halgren, E., and Cash, S.S. (2011). Single-neuron dynamics in human focal epilepsy. *Nature neuroscience* 14**,** 635-641.

Tseng, B.P., Giedzinski, E., Izadi, A., Suarez, T., Lan, M.L., Tran, K.K., Acharya, M.M., Nelson, G.A., Raber, J., Parihar, V.K., and Limoli, C.L. (2013). Functional Consequences of Radiation-Induced Oxidative Stress in Cultured Neural Stem Cells and the Brain Exposed to Charged Particle Irradiation. *Antioxid Redox Signal*.

Turrigiano, G. (2007). Homeostatic signaling: the positive side of negative feedback. *Curr Opin Neurobiol* 17**,** 318-324.

Turrigiano, G.G. (2008). The self-tuning neuron: synaptic scaling of excitatory synapses. *Cell* 135**,** 422-435.

Turrigiano, G.G., and Nelson, S.B. (2004). Homeostatic plasticity in the developing nervous system. *Nat Rev Neurosci* 5**,** 97-107.

Van De Vijver, I., Cohen, M.X., and Ridderinkhof, K.R. (2014). Aging affects medial but not anterior frontal learning-related theta oscillations. *Neurobiol Aging* 35**,** 692-704.

Van Elburg, R.A., and Van Ooyen, A. (2010). Impact of dendritic size and dendritic topology on burst firing in pyramidal cells. *PLoS Comput Biol* 6**,** e1000781.

Varga, C., Oijala, M., Lish, J., Szabo, G.G., Bezaire, M., Marchionni, I., Golshani, P., and Soltesz, I. (2014). Functional fission of parvalbumin interneuron classes during fast network events. *eLife* 3.

Vetter, P., Roth, A., and Hausser, M. (2001). Propagation of action potentials in dendrites depends on dendritic morphology. *J Neurophysiol* 85**,** 926-937.

Viventi, J., Kim, D.-H., Vigeland, L., Frechette, E.S., Blanco, J.A., Kim, Y.-S., Avrin, A.E., Tiruvadi, V.R., Hwang, S.-W., and Vanleer, A.C. (2011). Flexible, foldable, actively multiplexed, high-density electrode array for mapping brain activity in vivo. *Nature neuroscience* 14**,** 1599-1605.

Wagner, S., Rokita, A.G., Anderson, M.E., and Maier, L.S. (2013). Redox regulation of sodium and calcium handling. *Antioxid Redox Signal* 18**,** 1063-1077.

Wann, K.T., and Southan, A.P. (1992). The action of anaesthetics and high pressure on neuronal discharge patterns. *Gen Pharmacol* 23**,** 993-1004.

Weiss, S.A., Banks, G.P., Mckhann, G.M., Goodman, R.R., Emerson, R.G., Trevelyan, A.J., and Schevon, C.A. (2013). Ictal high frequency oscillations distinguish two types of seizure territories in humans. *Brain* 136**,** 3796-3808.

West, M.J., Slomianka, L., and Gundersen, H.J. (1991). Unbiased stereological estimation of the total number of neurons in thesubdivisions of the rat hippocampus using the optical fractionator. *Anat Rec* 231**,** 482-497.

White, A., Williams, P.A., Hellier, J.L., Clark, S., Edward Dudek, F., and Staley, K.J. (2010). EEG spike activity precedes epilepsy after kainate-induced status epilepticus. *Epilepsia* 51**,** 371-383.

Williams, R.S., and Matthysse, S. (1983). Morphometric analysis of granule cell dendrites in the mouse dentate gyrus. *J Comp Neurol* 215**,** 154-164.

Winfree, A.T. (2001). *The geometry of biological time.* Springer.

Winkels, R., Jedlicka, P., Weise, F.K., Schultz, C., Deller, T., and Schwarzacher, S.W. (2009). Reduced excitability in the dentate gyrus network of betaIV-spectrin mutant mice in vivo. *Hippocampus* 19**,** 677-686.

Winslow, J.L., Jou, S.F., Wang, S., and Wojtowicz, J.M. (1999). Signals in stochastically generated neurons. *J Comput Neurosci* 6**,** 5-26.

Wolf, S., Grein, S., and Queisser, G. (2013). Employing NeuGen 2.0 to automatically generate realistic morphologies of hippocampal neurons and neural networks in 3D. *Neuroinformatics* 11**,** 137-148.

Yang, M., Kim, H., Kim, J., Kim, S.H., Kim, J.C., Bae, C.S., Kim, J.S., Shin, T., and Moon, C. (2012). Fast neutron irradiation deteriorates hippocampus-related memory ability in adult mice. *J Vet Sci* 13**,** 1-6.

Zeitlin, C., Hassler, D.M., Cucinotta, F.A., Ehresmann, B., Wimmer-Schweingruber, R.F., Brinza, D.E., Kang, S., Weigle, G., Bottcher, S., Bohm, E., Burmeister, S., Guo, J., Kohler, J., Martin, C., Posner, A., Rafkin, S., and Reitz, G. (2013). Measurements of energetic particle radiation in transit to Mars on the Mars Science Laboratory. *Science* 340**,** 1080-1084.

Zhang, W., Thamattoor, A.K., Leroy, C., and Buckmaster, P.S. (2014). Surviving mossy cells enlarge and receive more excitatory synaptic input in a mouse model of temporal lobe epilepsy. *Hippocampus*.

Zhang, W., Yamawaki, R., Wen, X., Uhl, J., Diaz, J., Prince, D.A., and Buckmaster, P.S. (2009). Surviving hilar somatostatin interneurons enlarge, sprout axons, and form new synapses with granule cells in a mouse model of temporal lobe epilepsy. *J Neurosci* 29**,** 14247-14256.

Zhao, C., Deng, W., and Gage, F.H. (2008). Mechanisms and Functional Implications of Adult Neurogenesis. *Cell* 132**,** 645-660.

Zima, A.V., and Blatter, L.A. (2006). Redox regulation of cardiac calcium channels and transporters. *Cardiovasc Res* 71**,** 310-321.